

Nanoparticle Assembly and Oriented Attachment: Correlating Controlling Factors to the Resulting Structures

Dongsheng Li,* Qian Chen, Jaehun Chun, Kristen Fichthorn, James De Yoreo, and Haimei Zheng



Cite This: *Chem. Rev.* 2023, 123, 3127–3159



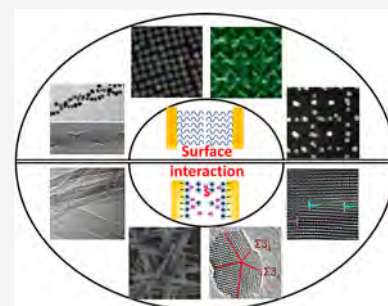
Read Online

ACCESS |

Metrics & More

Article Recommendations

ABSTRACT: Nanoparticle assembly and attachment are common pathways of crystal growth by which particles organize into larger scale materials with hierarchical structure and long-range order. In particular, oriented attachment (OA), which is a special type of particle assembly, has attracted great attention in recent years because of the wide range of material structures that result from this process, such as one-dimensional (1D) nanowires, two-dimensional (2D) sheets, three-dimensional (3D) branched structures, twinned crystals, defects, etc. Utilizing in situ transmission electron microscopy techniques, researchers observed orientation-specific forces that act over short distances (~ 1 nm) from the particle surfaces and drive the OA process. Integrating recently developed 3D fast force mapping via atomic force microscopy with theories and simulations, researchers have resolved the near-surface solution structure, the molecular details of charge states at particle/fluid interfaces, inhomogeneity of surface charges, and dielectric/magnetic properties of particles that influence short- and long-range forces, such as electrostatic, van der Waals, hydration, and dipole–dipole forces. In this review, we discuss the fundamental principles for understanding particle assembly and attachment processes, and the controlling factors and resulting structures. We review recent progress in the field via examples of both experiments and modeling, and discuss current developments and the future outlook.

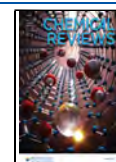


CONTENTS

1. Introduction	3128	4. OA-Induced Crystal Structures	3144
2. Particle Assembly and Controlling Factors	3129	4.1. 1D Nanowires, 2D Nanosheets, and 3D Branched Nanostructures	3144
2.1. Long- and Short-Range Forces Involved in Particle Interactions	3129	4.1.1. 1D Nanowires	3144
2.2. Ionic Strength, Ionic Species, and Temperature	3131	4.1.2. 2D Structures	3144
2.3. Solvent Effects	3132	4.1.3. 3D Structures	3145
2.3.1. Near Surface Solvent Structures	3132	4.2. Multiply Twinned Structures	3145
2.3.2. Bulk Solvent	3132	4.3. Necking	3146
2.4. Ligand Effects	3132	4.4. Defects Induced by OA	3147
2.4.1. Materials Structures Directed by Ligands of DNA and Biomimic Organics	3134	5. NP Interactions and Energetics of Particle Assembly and OA Processes	3148
2.4.2. Ligand Effect on Particle–Substrate Interactions	3135	5.1. Interparticle Potential and Evolution of Energetics	3148
2.4.3. Mapping Interparticle Interaction through Trajectory Sampling	3136	5.2. Individual NP Structural Modifications from NP Interactions	3149
2.5. Nanoparticle Shape Effects	3137	5.3. Coalescence and Facet-Dependent Surface Energy of Superlattices	3149
3. Oriented Attachment and Controlling Factors	3139	6. Summary and Outlook	3150
3.1. Crystallographic Orientation	3139		
3.1.1. Crystallographically Matched Attachments	3139		
3.1.2. Mismatched but Oriented Interfaces	3140		
3.2. Effect of Interfacial Liquid–Solid Structure	3141		
3.3. Interface-Driven Nucleation and OA of Crystals	3143		

Received: October 12, 2022

Published: February 20, 2023



6.1. Recent Achievements and Ongoing Advances	3150
6.1.1. Recent Achievements	3150
6.1.2. Ongoing Advances	3151
6.2. Remaining Challenges and Future Directions	3151
Author Information	3152
Corresponding Author	3152
Authors	3152
Author Contributions	3152
Notes	3152
Biographies	3152
Acknowledgments	3153
Abbreviations	3153
References	3154

1. INTRODUCTION

The size, geometry, and structure of materials determine emergent physical and chemical properties that have drawn considerable recent interest for optics, catalysis, and other fields.¹ For example, branched nanowires can have large absorption cross sections, short electron mean free paths, or complex patterns of optical interference.² Particle assembly is a common pathway for organizing material structures and crystal growth in both natural and synthetic systems, such as mineral formation in mollusk shells (where an organic matrix directs crystal growth of aragonitic tablets),³ (branched) colloidal superlattice structures,^{4,5} and hierarchical structures of nanowires⁶ (Figure 1).

Particle assembly in abiotic systems reflects the interplay of solution structure, interparticle forces, and motion in which crystal surfaces impose structure on the near-surface solution, leading to a set of interparticle forces, including hydration (solvation), steric hindrance, van der Waals (vdW), and electrostatic forces. These forces are influenced by the structure of the near-surface solution, which is affected by solvent, solution pH, ionic strength, ionic species, particle shapes, temperature, and ligands on the crystal surface. These factors determine the interparticle forces, motion, and the resulting assembled structures (e.g., superlattices) or crystal structures. For example, structures of colloidal crystal superlattices are controlled by functionalizing them with DNA strands that direct assembly through hybridization, leading to various types of symmetry of the structures of two-body centered tetragonal phases, a simple hexagonal phase, a cubic high-pressure gallium phase, and a gyroid phase.⁷

Oriented attachment (OA) is a special type of particle aggregation in which assembling particles become crystallographically coaligned before coalescence or attach while misaligned and relax into coalignment via atomistic processes. OA was first observed for TiO₂ (anatase) by Penn and Banfield in 1998 via ex situ transmission electron microscopy (TEM).^{8,9} Since then, crystal growth via OA has been widely reported in semiconductors,^{10–13} metals,^{14,15} silicates,^{16,17} oxides,^{6,8,18–26} fluorides,²⁷ organic compounds,²⁸ peptides,²⁹ and proteins.³⁰ OA leads to remarkable morphologies from the atomic to the micrometer scales, including tetrapods, chains,^{24,31} and sheets,³ highly branched nanowires,⁶ three-dimensional (3D) mesocrystals,²⁶ epitaxially connected nanocrystal superlattices,^{32,33} multiply twinned crystals,³⁴ and dislocations in crystal lattices³⁵ (Figure 1). For example, Zheng et al. showed that hexagonal self-assembled monolayers of oleate-capped PbSe nanocrystals (6.2 nm diameter) transformed into an epitaxially connected square

superlattice after OA of the PbSe nanocrystals.^{32,33} Li et al. showed that OA coupled with strain relaxation drove the formation of commonly observed 5-fold twinned structures of metal nanoparticles (NPs),³⁴ and a kinetically controlled OA process led to edge dislocations in rutile and anatase crystal lattices, enhancing their photoactivity.³⁵

In 2012, a major breakthrough was achieved through studies of OA by NPs of iron oxyhydroxide,³⁹ Pt₃Fe,⁴⁰ and platinum,⁴¹ which were observed in real time with atomic resolution using in situ liquid phase TEM (LP-TEM) imaging. The results on the iron oxyhydroxide system³⁹ demonstrated the ability to directly observe the process at lattice resolution, showing that ferrihydrite NPs coalign prior to attachment (Figure 2a–g)

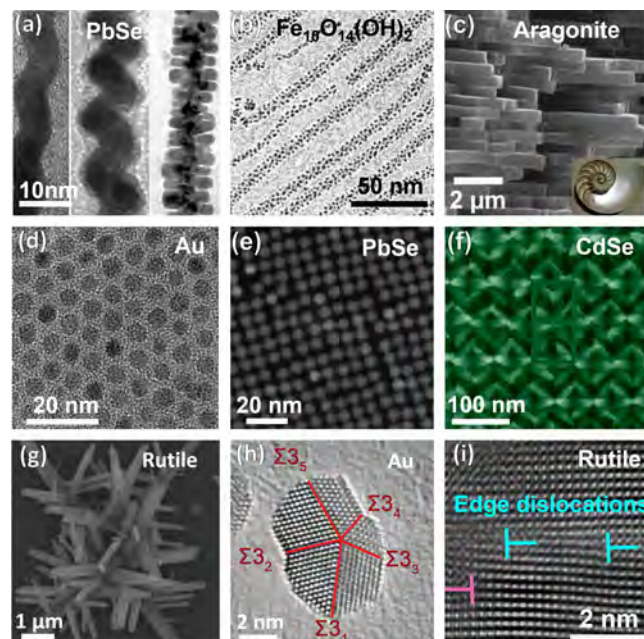


Figure 1. OA pathways leading to novel materials architectures revealed at both micrometer and atomic scales. (a) PbSe nanowires.³¹ Adapted with permission from ref 31. Copyright 2005 American Chemical Society. (b) Iron oxyhydroxide chain.²⁴ Adapted with permission from ref 24. Copyright 2010 American Chemical Society. (c) Nacre shell composed of organic matrix and aragonitic tablets.³ Adapted with permission from ref 3. Copyright 2005 Elsevier. (d) Au NP superlattice with 6-fold symmetry.³⁶ Adapted with permission from ref 36. Copyright 2018 American Chemical Society. (e) PbSe NP superlattice with 4-fold symmetry.³⁷ Reproduced with permission from ref 37. Copyright 2019 exclusive licensee American Association for the Advancement of Science. (f) CdSe branched colloidal superlattice.³⁸ Reproduced with permission from ref 38. Open Access. Copyright 2016 American Chemical Society. (g) Rutile branched nanowire.⁶ Reproduced with permission from ref 6. Copyright 2013 American Chemical Society. (h) Au 5-fold twin.³⁴ Adapted with permission from ref 34. Copyright 2019 The American Association for the Advancement of Science. (i) Rutile nanowire with edge dislocations.³⁵ Adapted with permission from ref 35. Copyright 2019 Wiley-VCH.

and are driven to attach through orientation-dependent forces. OA resulted in either a lattice-free interface or a twinned interface (Figure 2h,j). Analysis of the attachment dynamics led to the first estimate of the force that drives OA and demonstrated the existence of a force that acts over less than or equal to one-nm to drive OA events through “jump-to-contact” behavior of the small particles.

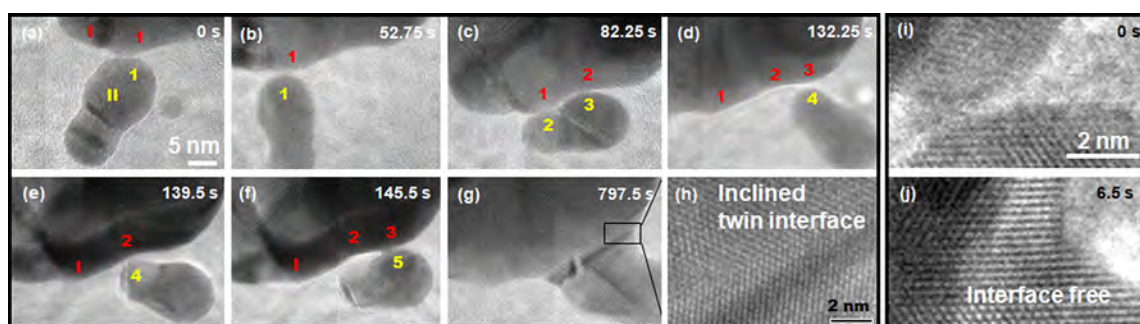


Figure 2. Dynamic attachment process and the resulting interface-free and twin related structures.³⁹ (a–g) Sequence of images showing the dynamics of one attachment process and the resulting twin related structure. (h) High-resolution image of interface in (g) showing twin structure (inclined twin plane). We define the two particles as I (partially shown in the upper part panels (a–g)) and II (the dumbbell shape particle in the lower part). The contact positions on the surfaces of the two particles are defined as 1, 2, and 3 for particle I, and 1–5 for particle II. (i–j) Sequence of images showing OA leads to interface-free structures. Adapted with permission from ref 39. Copyright 2012 The American Association for the Advancement of Science.

This force, that acts over $\lesssim 1$ nm distances is closely related to ordering of the solution near the particle surfaces and is affected by similar physicochemical parameters to those mentioned above (e.g., solvent, solution pH, ionic strength, ionic species, temperature, and ligands on the crystal surface). The effects of surface adsorption and surface charge were proposed to be the most dominant factors affecting OA.^{22,42–44} Many driving forces have been considered in theoretical models of OA processes in systems of various materials. These include reduction in surface energy,⁴⁵ dipole–dipole interactions,^{46,47} vdW forces,⁴⁸ and Coulombic interactions.⁴⁹ These forces are presumed to drive particles to overcome repulsive barriers, which come from electrical double layer (EDL), hydration, and steric interactions. A series of experimental and theoretical studies on OA-based growth kinetics have been used in an attempt to explain the process. The first phenomenological kinetic model of OA, which modeled the direct coalescence of particles as a reaction between the molecules and fit well with the experimental results of particle size vs time, was developed in 2003.⁴² After that, Penn²² and Ribeiro et al.⁵⁰ advanced OA models from the viewpoint of electrostatic interactions and colloid coagulation, respectively.

In addition to the near-surface solution structure, OA is also strongly correlated to the crystallographic structure of the surface atoms of the nanocrystals, leading to perfect or twin-related alignment of two crystals forming interface-free or twin structures, respectively.³⁹ A special form of OA (mismatched but oriented) has also been proposed. For example, the OA of anatase {103} facets onto rutile {101} facets, followed by anatase to rutile phase transformation, during which the {103} plane transforms into rutile {101}, lead to either rutile wire growth (interface-free structure) or branch growth via {101} twin boundaries.⁶

2. PARTICLE ASSEMBLY AND CONTROLLING FACTORS

2.1. Long- and Short-Range Forces Involved in Particle Interactions

The assembly of mineral nanocrystals, whether via OA or non-OA, results from a competing and cooperative interplay between short- and long-range forces (Figure 3). This interplay in energetic contributions is coupled to dynamic contributions (i.e., hydrodynamic and Brownian forces) via translational and rotational diffusivity/mobility, leading to local responses of particles and resultant microstructures during assembly. In

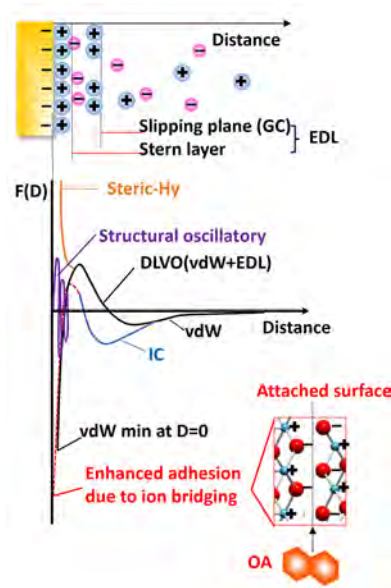


Figure 3. Profile of water structure and force distribution on particle surfaces. OA is a mesoscale response to forces defined by molecular details of the interfacial region. These details create forces that drive particle motion. As particles move, structure and forces evolve, transitioning from a regime of long-range to short-range interactions, leading to alignment and attachment.⁶² Modified with permission from ref 62. Copyright 2003 Elsevier Science Ltd.

particle assembly processes, colloidal particles are typically coated with organic ligands, polymers, or biomaterials (e.g., peptoids or DNA), which induce steric hindrance and prevent particle aggregation and growth into larger crystals. When colloidal particles approach one another, the types of interactions include vdW attraction, ion correlation (IC), EDL repulsion, hydration (Hy) repulsion, and steric interactions. Hy and steric hindrance repulsive forces are relatively short-range forces; the hydration layer and ligands directly adsorbed on the crystal surfaces dictate the short-range nature of the forces.

The Derjaguin–Landau–Verwey–Overbeek (DLVO) theory is a continuum-based theory of colloidal dispersion stability that uses a surface potential and dielectric property as key fundamental materials properties to explain interaction forces between two particles. It assumes a linear superposition of vdW forces (F_{vdW}), originating from interactions between

fluctuating dipoles in molecules by absorption of photons from the background radiation field, and EDL forces (F_{EDL}), understood as an osmotic pressure difference associated with an inhomogeneous distribution of ions due to a surface potential.

The DLVO theory becomes questionable where inherent continuum approximations in the theory become invalid. For example, the Poisson–Boltzmann (PB) model associated with EDL forces assumes⁵¹ that the electrolyte solution can be implicitly described as a continuous dielectric medium characterized by an average density of electrolytes (i.e., averaging out the degrees of freedom of solvent molecules and mobile ions), ignoring the granularity of the ions (i.e., the finite size of the ions and ion–ion interactions);⁵¹ but both “non-ideal” characteristics become important at high salt concentrations, leading to IC. Ion–ion correlations become significant when the electrostatic interaction energy between neighboring ions is larger than the thermal energy, for example, considering strong electrostatic coupling between ions in multivalent salt solutions. The strong correlations between ions can cause surface charge inversion and attraction forces.⁵² Similarly, the Lifshitz theory for vdW forces assumes that each entity can be completely represented by a full spectrum of dielectric functions,⁵³ which also becomes questionable at high salt concentrations.

Considering the molecular nature of the near-surface solution, the EDL force can be further divided into outer layer (diffuse Gouy–Chapman (GC) double layer) and inner (Stern) layer interactions (Figure 3 and Table 1). This leads to IC within the

Table 1. List of Attractive and Repulsive Forces at Long and Short Ranges

forces	long-range	short-range	attractive force	repulsive force
van der Waals (vdW)	x	x	x	(possible) ^b
electrical double layer (EDL)	x	x	(possible) ^a	x
Ion correlation (IC)		x	x	
surface hydration		x		x
steric hindrance		x		x

^a(1) IC occurs within the EDL; i.e., high salt concentrations or multivalent salt solutions lead to ion–ion correlations due to strong electrostatic coupling between ions and cause surface charge inversion and attraction forces.⁵² (2) Electrostatic forces can be attractive when interacting surfaces are dissimilar. ^bThe vdW force can be negative when a frequency-dependent dielectric property of one of the interacting surfaces is smaller than that of the intervening medium for dissimilar surfaces.

GC layer and Hy repulsion, which includes both ion and surface hydration, within the Stern layer. Hy repulsive forces beyond ~1 nm are due to ion layering; below ~1 nm, water structuring can also lead to short-range structural forces on the length scale of water molecules.⁵⁴ This repulsive force strongly depends on the ion strength and ionic species.^{54–56} Note that ion hydration and surface hydration are indeed competing with each other, depending on the relative preference for water–ion interactions over water–surface interactions.⁵⁷ If ligand absorption is not considered, the total interaction force between two surfaces, based on a superposition assumption of individual forces, is expressed as

$$\frac{F(D)}{R} = \frac{F_{\text{vdW}}}{R} + \frac{F_{\text{IC}}}{R} + \frac{F_{\text{GC}}}{R} + \frac{F_{\text{Hy}}}{R} \quad (1)$$

where R is the radius of curvature characterizing the solid–liquid interface, such as the particle radius) and D is the distance from the surface. The outer layer contribution F_{GC} is equivalent to the diffuse GC double layer repulsive interaction. The EDL contribution from the Stern layer is expressed as F_{Hy} . The total force^{58,59} between two particles in aqueous solution is given by

$$\begin{aligned} \frac{F(D)}{R} = & -\frac{A_{\text{H}}}{2D^2} - \int k_{\text{B}} T F(\Gamma) d\rho_{\text{sol}}(D) + \frac{\Omega}{\lambda_{\text{D}}} \exp\left(-\frac{D}{\lambda_{\text{D}}}\right) \\ & + 2\pi W_0 \exp\left(-\frac{D}{\lambda_{\text{Hy}}}\right) + \sum_{i=1} A_i(\rho_i) \exp\left(-\frac{D}{\sigma}\right)^2 \end{aligned} \quad (2)$$

The first two terms in eq 2 describe the vdW and IC attractive forces. The Hamaker constant A_{H} is a mild function of λ_{D} , the Debye length of the solution. λ_{D} can be calculated from the ionic strength I using

$$\lambda_{\text{D}} = \left(\frac{\epsilon_r \epsilon_0 k T}{2 I e^2} \right)^{1/2} \quad (3)$$

where ϵ_r is the relative dielectric constant of continuous medium, ϵ_0 is the vacuum dielectric permittivity, k is the Boltzmann constant, T is the absolute temperature, and e is the electron charge (1.6×10^{-19} C). I can be calculated using

$$I = 1/2 \sum (z^k)^2 n_b^k \quad (4)$$

Here, and z^k and n_b^k are the valence and bulk concentration of k th ion, respectively. An increase in ionic strength (via both ion concentration and valence) leads to a decrease in repulsive forces between particles and *vice versa*, because λ_{D} is inversely proportional to the square root of ionic strength that is proportional to $\sum (z^k)^2 n_b^k$. Γ in eq 2 is a measure of the coupling energy and is proportional to $\sqrt{|f(I, \lambda_{\text{D}}) \rho_{\text{crys}} Q^3|}$, where ρ_{crys} is crystal surface ion density related to the facet-specific charge density, discrete charge distribution of the crystal, and ionic strength. The function f reflects an incomplete screening of surface charge that can be fitted from the ionic strength dependence of counterion distribution near charged surfaces. ρ_{sol} is the ion density near the surface. The last three terms in eq 2 describe the GC, ion Hy, and surface Hy repulsive forces based on the assumption that these forces can be characterized by a “screening” length representing respective molecular structural information as a key descriptor. Ω is the interaction constant. W_0 and A_i are prefactors, λ_{Hy} is the decay length of F_{Hy} , ρ_i is oscillatory parameter, and σ is the structural hydration layer spacing. W_0 , A_i , and λ_{Hy} are related to I and can be obtained by fitting to experimental data.⁵⁸

It is noteworthy that the importance of molecular granularity (i.e., ions and solvent molecules as interacting entities with finite sizes) becomes more critical when the characteristic size of the particles, λ_{p} , becomes comparable to λ_{m} , a characteristic length scale associated with the discrete nature near the interfaces.⁶⁰ For example, it was pointed out that an error associated with neglecting the discrete nature of the intervening solvent for vdW forces scales as $O(\lambda_{\text{d}}/L)$, where L is the separation between the macroscopic bodies.⁶¹ In this case, the molecular nature cannot be neglected for vdW forces between particles when $\lambda_{\text{d}} \sim O(L)$.

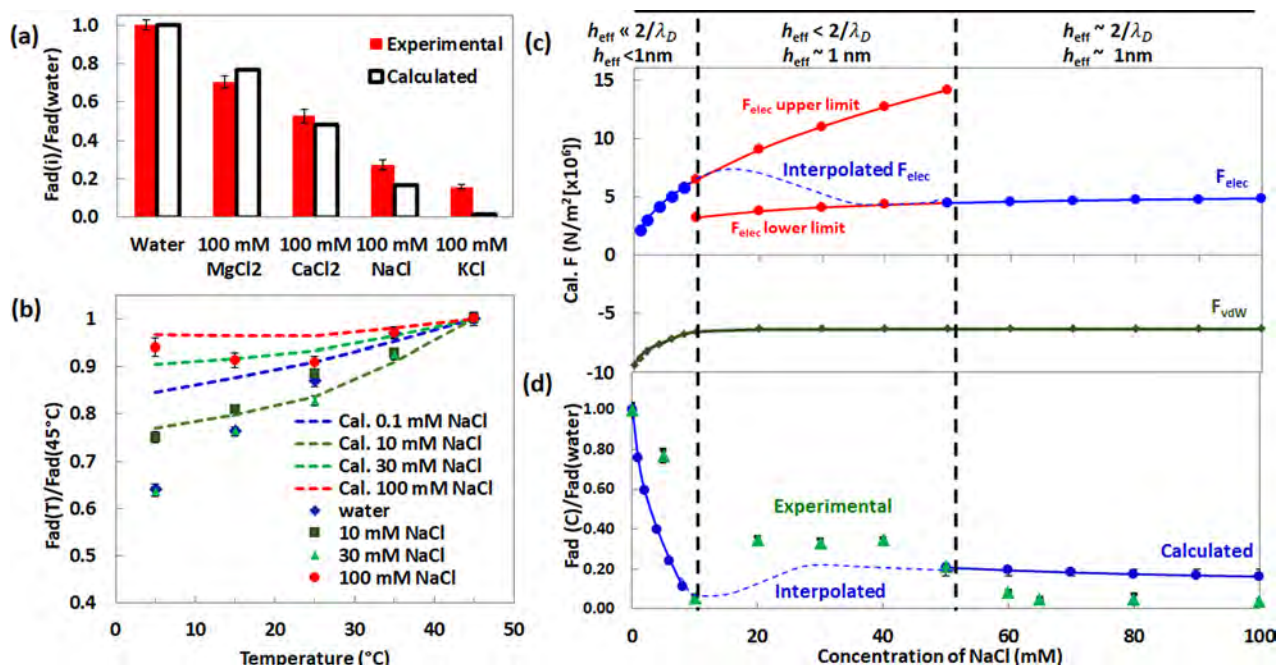


Figure 4. Dependence of F_{ad} on NaCl concentration (C_{NaCl}), electrolyte type, and temperature (T).⁷¹ (a) Experimental and calculated values of F_{ad} for a range of electrolytes, where F_{ad} is normalized to that for pure water, (b) Experimental and calculated values F_{ad} vs T for a range of C_{NaCl} , where F_{ad} is normalized to the value at 45 °C. The calculated curve for 0.1 mM NaCl was used for comparison with the observed values in pure water. (c) Calculated (solid curve) and extrapolated (solid red curves) or interpolated (dashed blue curve) values of F_{elec} and F_{vdW} vs C_{NaCl} based on DLVO theory modified to include the charge-regulating nature of the mica surface. (d) Experimental and calculated values of F_{ad} vs C_{NaCl} and three regions of C_{NaCl} defined by the ratio of the estimated separation (h) to the calculated value of $2/\lambda_D$. h_{eff} is an effective separation between crystal surfaces. Cal.: Calculated. Modified with permission from ref 71. Copyright 2017 PNAS open access.

2.2. Ionic Strength, Ionic Species, and Temperature

The role of electrostatic interactions in directing particle aggregation has been highlighted previously. Several studies have emphasized the role of dipole–dipole interactions in inducing directional nanocrystal aggregation.^{63–65} However, Alimohammadi and Fichthorn used molecular dynamics (MD) simulations to show that when two anatase NPs are in close proximity, more localized electrostatic interactions become important in directing aggregation, even though each particle possessed a relatively high dipole moment.⁶⁶ Schapotschnikow and co-workers reached a similar conclusion in simulations of the aggregation of PbSe nanocrystals.⁶⁷ Zhang and Banfield also concluded that Coulombic interactions are the primary driving force for OA when two particles are in close proximity.⁶⁸

In the simple context of DLVO theory (i.e., electrostatic and vdW forces), ionic strength directly influences λ_D , a characteristic length scale over which the electrostatic interaction potential decays⁶⁹ as shown in eq 3. This relation also implies that temperature can change the repulsive force based on (1) a direct effect from the square root dependence and (2) an indirect effect via the temperature dependence of the relative dielectric constant (i.e., decreasing as the temperature increases⁷⁰). Note that the vdW force, resulting from interactions between objects through an intervening medium via fluctuating electromagnetic fields ranging from microwave to X-rays, is relatively insensitive to a change in ionic strength. The change mainly influences the low frequency regime (i.e., up to THz) that does not significantly contribute to the vdW force unless the ion concentration becomes high.⁶¹

In practical nanoscale systems, the long- and short-range forces involved in particle interactions are determined by the near-surface solvent structures, which reflect molecular nature

and the effects of ionic strength/species and temperature becomes more complicated. Understanding this complex dependence requires implementation of key molecular nature into macroscopic descriptions of adhesion forces based on electrostatic and van der Waals forces.

Using atomic force microscopy (AFM)-based dynamic force spectroscopy (DFS) method, Li et al. used tips fabricated from oriented mica and measured the magnitude of the adhesion forces between mica (001) surfaces (Figure 4).⁷¹ Taking advantage of the near-equilibrium nature of the force measurements, this study shows that the adhesive force between mica surfaces in the solvent-separated regime has a $\sim 60^\circ$ periodicity related to crystal structure and depends strongly on electrolyte type, concentration, and temperature. The separation between two surfaces via the size of hydrated ions varies over different ion species (i.e., ion specificity), as well as the dependence of ionic strength and temperature on Debye length. The structure of the interfacial solution layer fundamentally changes F_{vdW} and the electrostatic force (F_{elec}), leading to significant changes of attractive forces as a function of the parameters mentioned above.

The nonmonotonic variation of adhesive force (F_{ad}) with electrolyte concentration indicates the magnitude of F_{ad} is determined by competing forces. Analysis shows these features are all consistent with an attractive interaction induced by vdW forces that is indeed competing with electrostatic and hydration forces. This balance is predicted to be very sensitive to the short-range surface hydration structure, which can be controlled via electrolyte type, concentration, and temperature, leading to changes in the dependence of force on separation and consequent variations in effective separation (h_{eff}). This demonstrates a need for the coupling between microscopic

details (e.g., water structure, ion hydration, and charge regulation at the interface) and the continuum model for electrostatic repulsion and vdW attraction, in order to understand forces in the solvent-separated state.

2.3. Solvent Effects

Solvent can be a controlling factor in two ways: (1) an energetic contribution associated with solvent structuring at solid/liquid interfaces, giving rise to structural forces and (2) a dynamic contribution associated with motions of particles in bulk (i.e., hydrodynamics).

2.3.1. Near Surface Solvent Structures. Using LP-TEM imaging of the NP assembly process and AFM-DFS of measuring surface interaction forces,⁷² Lee et al. showed that superlattice formation and the transient behavior of particles and clusters are due to a delicate balance of forces, including Brownian, vdW, steric hindrance, electrostatic, and hydration, acting over many length scales. At large separation (~ 20 nm), NP dynamics are correlated with F_{vdW} (Figure 5a,b) despite

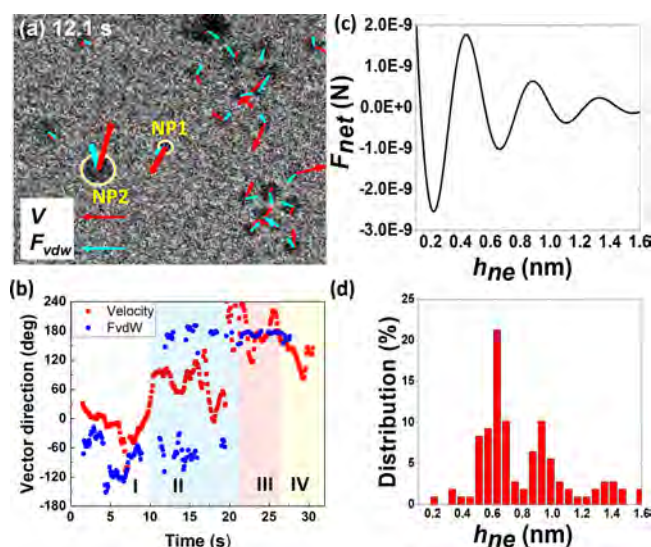


Figure 5. Ag NP superlattice formation reflects balance of multiple long-range and short-range forces.⁷² (a) A snapshot from an in situ LP-TEM movie of Ag NP assembly process. (b) Directions of v and F_{vdW} of NP1 in (a), showing correlation between them. (c) Calculated net force between two NPs. (d) Distribution of NP separations based on LP-TEM images after assembly. Adapted with permission from ref 72. Copyright 2019 Wiley-VCH.

Brownian motion. Combined with DFS measurements of interparticle forces, the results show that a balance between hydration and F_{vdW} forces at short ranges causes characteristic particle separations ($\sim 0.6, 0.9$, and 1.4 nm; Figure 5c,d) for both the transient and final structures, an outcome ascribed to layers of hydrated ions adsorbed on NP surfaces, not due to organic ligands. The superlattice structure is dictated by NP hydration structure.

2.3.2. Bulk Solvent. The dynamics of particles in solution are influenced by thermal fluctuations (Brownian motion) and hydrodynamic interactions, which are affected by solvent characteristics (e.g., viscosity). This is directly correlated to the dynamic nature of colloidal suspensions.⁷³

Neglecting rotational motions of particles that are relevant to anisotropic particles, the drag or hydrodynamic force (F_{D}) can be described by the following equation,⁷⁴

$$F_{i,D} = - \sum_{k=1}^{n_j} \mathcal{K}_{ij} V_{ij\text{rel}} \quad (5)$$

where, $V_{ij\text{rel}}$ is a relative velocity of particle i in comparison to the velocity of particle j . Here \mathcal{K}_{ij} is the hydrodynamic resistivity between particles i and j , i.e., a proportionality tensor correlating an imposed velocity $V_{ij\text{rel}}$ and the resultant hydrodynamic drag force.

The \mathcal{K}_{ij} between two unequal spherical particles is dependent on the ratio of particle sizes ($\lambda = a_j/a_i$), in addition to the separation between particles, the value of the radius for one particle, a_i , and the solvent viscosity, μ . The hydrodynamic resistivity has been calculated by multipole expansions combined with asymptotic analyses at a lubrication regime as shown by Jeffrey and Onishi.⁷⁴ The normalized hydrodynamic resistivity for spherical particles involves two different modes of motions between two unequal spherical particles, motions along and perpendicular to the line of centers. The leading order of the hydrodynamic resistivity for the motion along the line of centers in the lubrication regime (where a significant hydrodynamic drag force is expected), $O(1/\epsilon)$, is much larger than that for the motion perpendicular to the line of centers, $O(\log(1/\epsilon))$. Here, ϵ is a normalized separation by a harmonic average of the particle radii. Therefore, we can mainly consider the hydrodynamic resistivity for the motion along the line of centers; all coefficients of the even or odd functions and singular terms associated with this mode of the relative motion are shown in the work by Jeffrey and Onishi.⁷⁴

Thus, the magnitude of F_{D} can be obtained by

$$\begin{aligned} |F_{i,Dx}| &= \left| - \sum_{k=1}^{n_j} \mathcal{K}_{ij} V_{ij\text{rel}} \cos \theta \right|, \\ |F_{i,Dy}| &= \left| - \sum_{k=1}^{n_j} \mathcal{K}_{ij} V_{ij\text{rel}} \sin \theta \right| \end{aligned} \quad (6)$$

where θ is the angle between the relative velocity vector and position vector. The direction of F_{D} is opposite from the direction of particle motion. It is important to note that \mathcal{K}_{ij} is heavily dependent on the particle shape. A nonspherical shape will bring a qualitatively different form of \mathcal{K}_{ij} due to characteristic directors to describe the particle orientation, as well as a different separation dependence in \mathcal{K}_{ij} and the importance of rotational motions.^{75,76}

2.4. Ligand Effects

For organic ligands, when two NPs coated by ligands approach each other and the ligands begin to overlap, they experience a steric hindrance force (F_{sh}). This force is repulsive in nature, caused by the unfavorable entropy related to confining the chains between the surfaces. F_{sh} can be estimated by the modified Alexander–de Gennes equation.^{77–79} F_{sh} here is due to the osmotic pressure, which actually drives solvent molecules out of the soft overlapping areas between neighboring NPs, as well as the elastic energy of ligands as the ligands are compressed. Assuming the solvent is as a good solvent for the ligand (i.e., the solvent–ligand interaction is greater than the solvent–solvent interaction, leading to the ligands to expand, following the context of polymer chemistry⁸⁰), the steric hindrance force can be described by the interaction energy per unit area between two plates,

$$W_{\text{sh}} \approx \frac{100}{\pi s^3} kT e^{-\pi h/L} \quad (7)$$

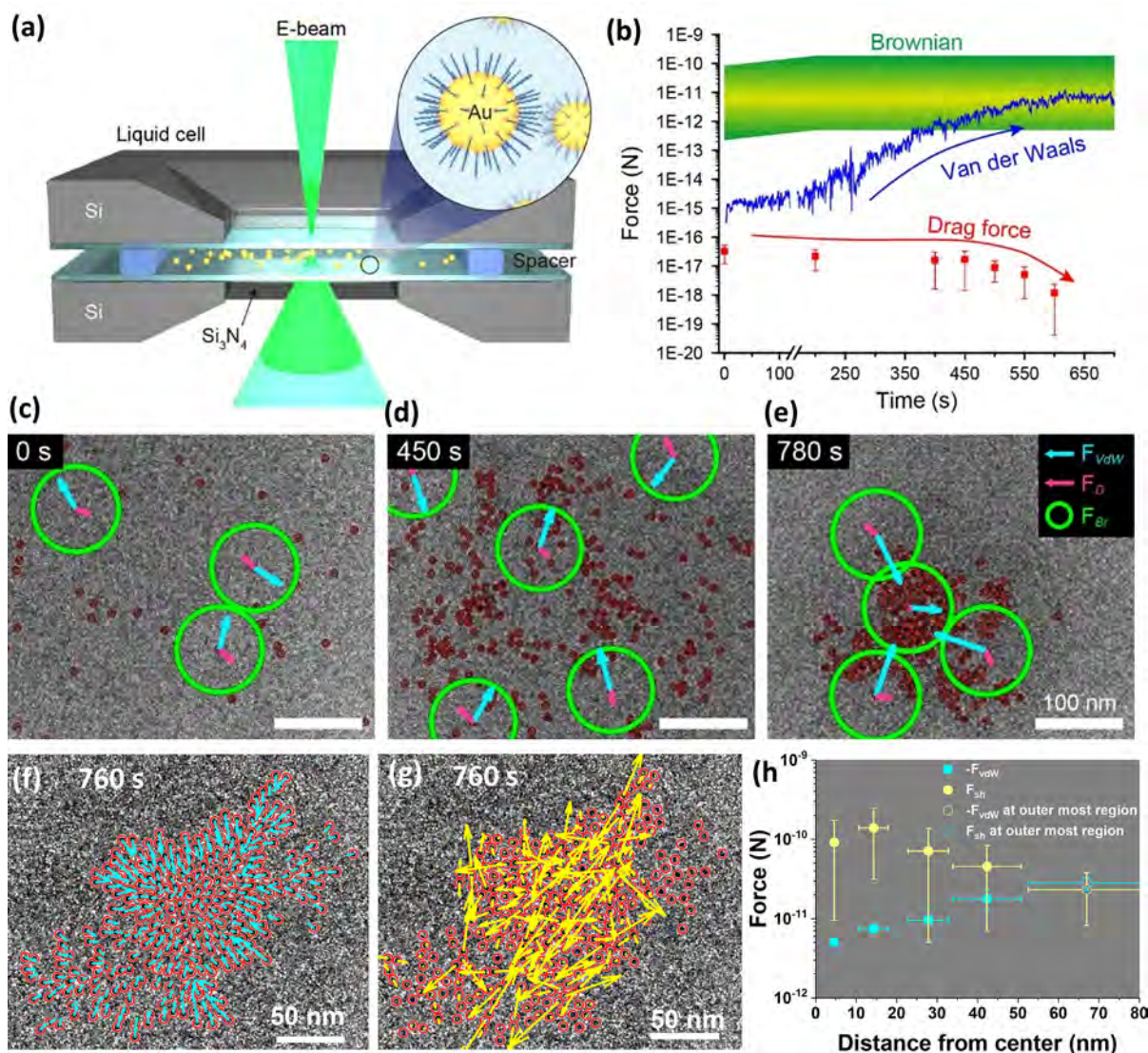


Figure 6. Tracking the dynamics of gold NP self-assembly in toluene.³⁶ (a) Scheme of a liquid cell used for the in situ LP-TEM experiments. (b) Interparticle forces as a function of assembly time. (c–e) Time sequenced LP-TEM images of Au NP assembly and calculated forces acting on individual NPs. (f–h) Force analysis of F_{vdW} and steric hindrance of particles in a dynamic superlattice. Cyan and yellow arrow arrows in (f) and (g) represent F_{vdW} and F_{sh} respectively. Force values in (c–e) are in log scale. Adapted with permission from ref 36. Copyright 2018 American Chemical Society.

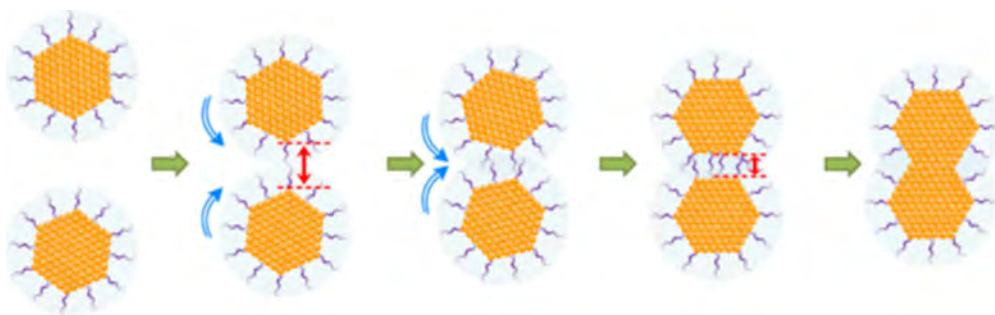


Figure 7. Mechanism proposed by Zhu et al. for the aggregation of citrate-capped Au NPs on the {111} facets.⁸¹ Reproduced from ref 81. Access to this figure is permitted under a Creative Commons License at <http://creativecommons.org/licenses/by/4.0/>.

where s is the footprint diameter of a single polymer chain and L is the end-to-end distance of ligand in a good solvent. The length of ligands mainly influences the range of the steric hindrance interactions, i.e., F_{sh} drops to zero when there is no overlap

between ligands and determines the interparticle spacing, which plays a critical role in resulting superlattice properties. Following the Derjaguin approximation,⁶⁹ the steric hindrance force between two spherical particles can be further approximated as

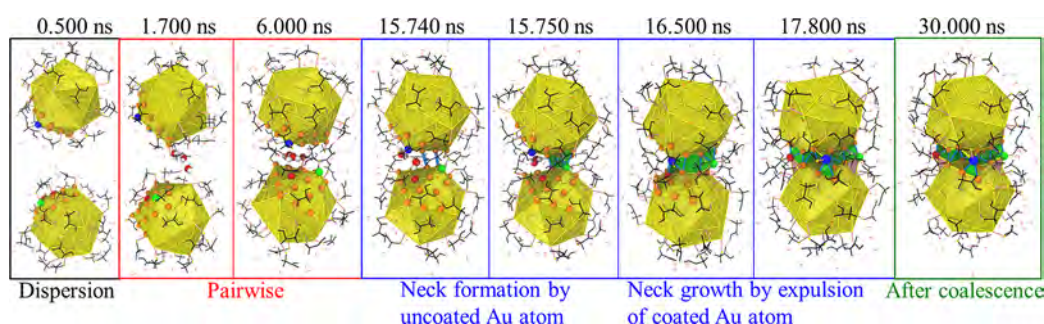


Figure 8. Schematic of the aggregation process of two Au nanocrystals coated with $\text{S}(\text{CH}_2)_{11}\text{COOH}$ in water.⁸² Initially, the nanocrystals are dispersed in water (dispersion). As they approach one another, they form a dimer (pairwise), and they subsequently begin to form a neck via exchange of uncoated Au atoms. The neck grows by expulsion of ligands from the particle gap until the particles have coalesced. Reproduced with permission from ref 82. Copyright 2020 American Physical Society..

$$F_{\text{Sh}} = \frac{200}{s^3} LRkT e^{-\pi h/L} \quad (8)$$

where h is the separation between particles and R is the radius of particle.

Lee et al. quantitatively evaluated Brownian force (F_{Br}), F_{vdW} , F_{D} , and F_{Sh} among Au NPs in toluene and their competition at various separations (Figure 6a–e) during the assembly process by integrating LP-TEM experiments with theory.³⁶ It was found that, at relatively short-range particle separation, the vdW force overrode the Brownian force and was dominant in driving assembly. When the particles were in close proximity, a delicate balance between vdW and steric hindrance forces, coupled with hydrodynamic forces, determines the NP separation (2–3 nm) and leads to a unique dynamic nature of the assembled superlattice (Figure 6f–h).

Typically, organic ligands can prevent NPs from aggregation, tune the interparticle distances, and program superlattice structures, which determine the resulting superlattice properties. Weakly bonded small organic molecules can direct particle aggregation and control the OA process.

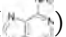
Zhu et al. used in situ LP-TEM to demonstrate the ligand-controlled OA of citrate-stabilized gold NPs.⁸¹ A schematic of their proposed mechanism is shown in Figure 7. They observed that when the particles reached a distance at which their ligands could begin to overlap, they jumped to contact upon reaching a common {111} orientation, with simultaneous expulsion of ligands from the interparticle gap. This observation correlated with results from first-principles calculations, which indicated the ligand binding energy was the lowest on the {111} facets.

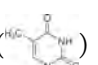
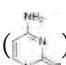
Guo and Gao studied the aggregation of two Au nanocrystals coated with $\text{S}(\text{CH}_2)_{11}\text{COOH}$ in water.⁸² As Figure 8 shows, the aggregation involved association, neck formation via uncoated Au atoms, and finally expulsion of ligand from the interparticle gap as neck formation completes and the particles are coalesced. Balankura et al. observed a similar mechanism for the aggregation of two polyvinylpyrrolidone (PVP)-covered Ag nanoplates in ethylene glycol solvent.⁸³ Their MD simulations revealed that the aggregation mechanism of the PVP-covered Ag nanoplates is one in which PVP capping molecules continuously diffuse around the aggregate and/or desorb to vacate the interparticle gap so that aggregation can occur. They noted that because the side facets of the plates contain less adsorbed PVP than the faces, less transport was needed to vacate the interparticle gap so that the free energy barrier was lower for side-to-side aggregation than for face-to-face aggregation. Their

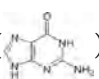
observations were consistent with the experimentally observed formation of Ag nanoplates in the presence of PVP.^{84,85}

2.4.1. Materials Structures Directed by Ligands of DNA and Biomimic Organics.

DNA and biomimic organics (e.g., peptoids) can serve as unique programmable ligands. For example, due to DNA's unique Watson–Crick base-pairing interactions, introducing a number of distinct and well controlled superlattice structures.^{86–88} The forces between DNA-capped NPs include Watson–Crick base pairing forces

through hydrogen bonds, in which adenine () binds to

thymine () and cytosine () binds to guanine

()⁸⁹ π – π stacking interactions,⁹⁰ vdW attractions, and electrostatic repulsive forces.⁸⁶ In aqueous solutions, base-pairing controls the superlattice growth by tuning the ionic strength and/or annealing temperature.⁹¹

Mirkin used a complementary contact model (CCM) to predict the crystallographic structures for DNA-based NP superlattice growth in aqueous buffered conditions.⁸⁷ Key aspects of this model are (1) DNA-NPs with equal DNA-NP radii in the superlattice (R_n) will maximize the number of closest neighbors to which it can form DNA connections; (2) when two lattices are of similar stability, a kinetic product can be produced by slowing the rate at which individual DNA linkers dehybridize and subsequently rehybridize; (3) the hydrodynamic size, as opposed to the core size or DNA length, mainly determines the superlattice structure; and (4) in a binary system, the size ratio and DNA linker ratio between two particles dictate the thermodynamically favored crystal structure. The “size ratio” is defined as the ratio of the DNA-NP hydrodynamic radii (the sum of the inorganic particle radius and DNA linker length), and the DNA linker ratio is the ratio of the number of DNA linkers on the two different types of DNA-NPs.^{87,91}

Based on the above rules, Mirkin also developed an approach to fabricating complex and low symmetry structures using programmable NP functionalized with DNA strands by tuning the NP size (R_n) and the number of DNA strands attached on the NP (S_n), providing two types of interactions between NPs (Figure 9): ionic-like (“ionic”) bonding between two NP with comparable R_n (programmable atom equivalents, PAE) and metallic-like (“metallic”) bonding between two NPs with one large and one small R_n (mobile electron equivalents, EE).⁹² Depending on the number of input linker strands and EE/PAE

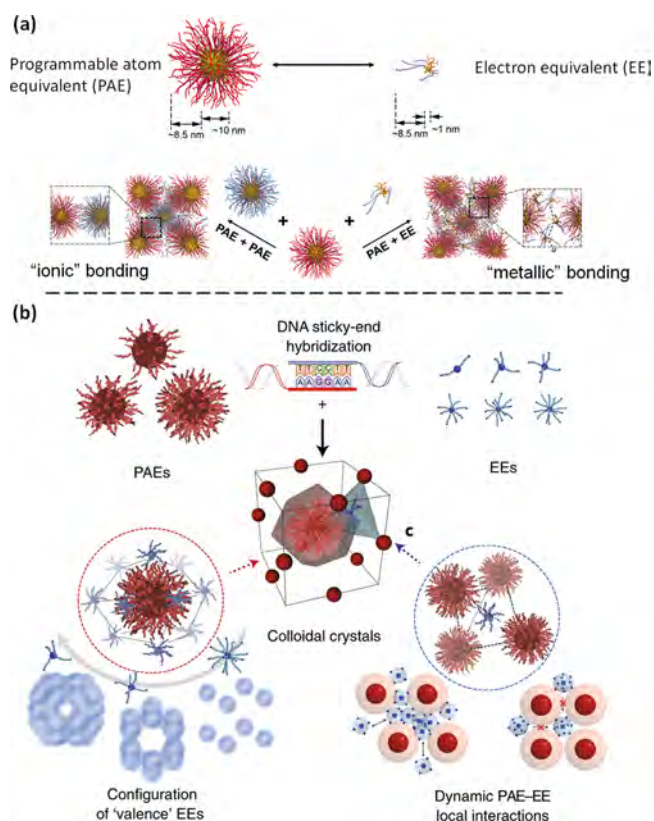


Figure 9. Schematic drawing of PAE, EE, and an example of resulting crystal. (a) PAE, EE, and the resulting "ionic" and "metallic" bonding.⁹² (b) An example of colloidal crystals synthesized from coassembling PAEs and EEs.⁷ (a) Adapted with permission from ref 92. Copyright 2019 American Association for the Advancement of Science. (b) Reproduced with permission from ref 7. Copyright 2022 Nature/Springer/Palgrave.

stoichiometry, nine crystalline phases were formed when the PAEs and EEs were mixed (Figure 10).⁷

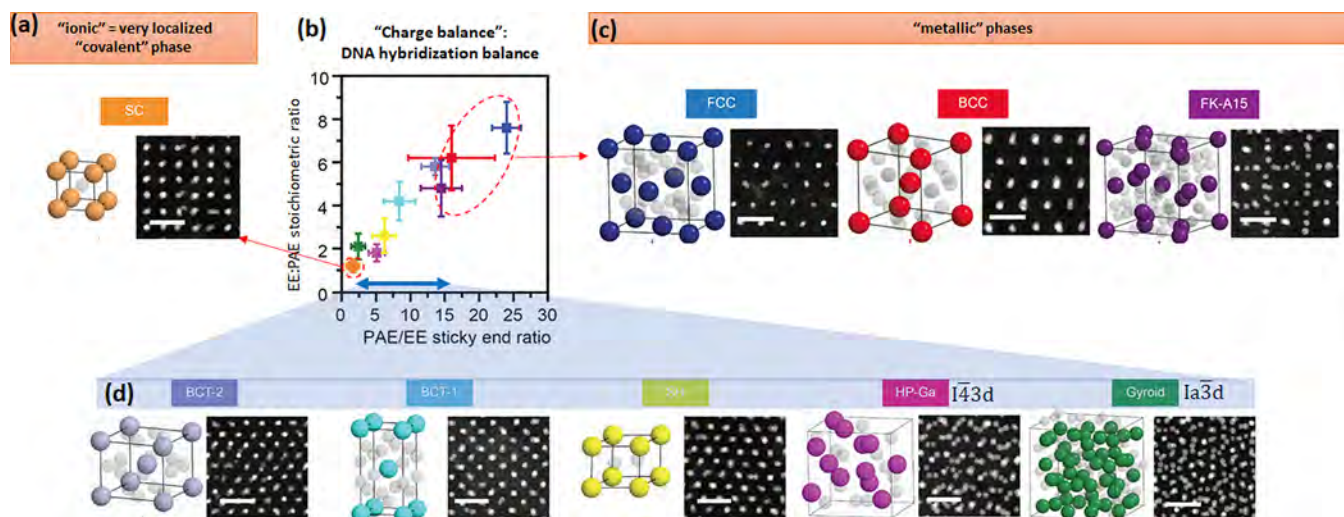


Figure 10. Formation of PAE-PAE ("ionic") and PAE-EE ("metallic") assemblies through DNA-based interactions. (a, c, d) Unit cell models (PAEs in color, EEs in light gray (left), representative cross-sectional low-angle annular dark-field (LAADF) images (right), Scale bar is 50 nm. (b) A positive correlation is observed between PAE/EE stoichiometry and the surface sticky-end density ratio (based on input linkers).⁷ Adapted by permission from ref 7. Copyright 2022 Nature/Springer/Palgrave.

Similarly, biomolecules or biomimetic materials have been used to direct crystal growth and the resulting structures. For example, Rosi et al. reported a peptide-based method to design and synthesis of NP superstructures containing double helices of Au NPs (Figure 11a).⁹³ Zhu et al. reported that 4-

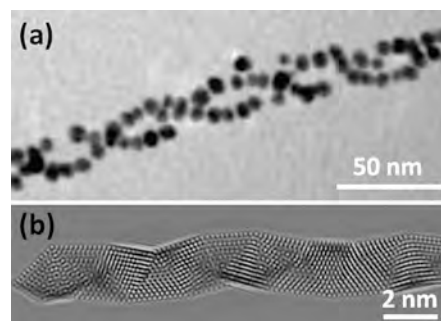


Figure 11. Biomolecules and biomimetic organics direct the structures of double helices and a chiral helix structure. (a) TEM image of gold NP double helices.⁹³ Reproduced with permission from ref 93. Copyright 2008 American Chemical Society. (b) Simulated high resolution TEM (HRTEM) image of a single BCB-structured Au NW, based on experimental HRTEM image.⁹⁴ Reproduced with permission from ref 94. Open access. Copyright 2014 American Chemical Society.

mercaptobenzoic acid, a strong ligand, assisted the formation of a chiral Boerdijk-Coxeter-Bernal (BCB) helix, which is composed of linearly stacked regular Au tetrahedra (Figure 11b).⁹⁴

2.4.2. Ligand Effect on Particle-Substrate Interactions. Ligand molecules adsorbed on NPs can determine NP-substrate interactions and interparticle interactions (see also section 2.2), both of which have been quantified and measured using the direct imaging capability of LP-TEM.

The surface ligands on NPs can impact the interaction between NPs and substrate and thereby affecting the motions of NPs when they are observed in liquid cells under TEM imaging. It has been reported that the Si_3N_4 substrate of a liquid TEM cell becomes positively charged during electron beam illumination

due to ionization of the Si_3N_4 surface. This positive surface potential increases with increasing electron beam intensity.⁹⁵ Indeed, negatively charged NPs (e.g., citrate-coated or carboxylate acid end functionalized gold NPs) dispersed in deionized water were observed to adsorb and immobilize on Si_3N_4 surface during in situ LP-TEM imaging due to the strong electrostatic attraction between the NPs and positively charged Si_3N_4 surface. The process of a NP adsorbing onto a Si_3N_4 surface was observed in a previous LP-TEM study, which shows that adsorption can be described by a Langmuir adsorption isotherm.⁹⁶ In comparison, positively charged NPs (e.g., amine end functionalized gold NPs) were repelled from the Si_3N_4 surface and moved around to interact with other NPs and formed into assemblies under LP-TEM observations.⁹⁵ Due to the electrostatic nature of this NP–substrate interaction, changing the ionic strength of the solution can change the strength of the NP–substrate interaction. For example, ~ 15 mM phosphate buffered solution (PBS) screens the substrate–NP attraction such that even negatively charged NPs can exhibit diffusional motions in LP-TEM observations.⁹⁷ This fast diffusion of NPs is essential for the formation of crystals from dynamic assembly of the NPs. It also facilitates the annealing of defects via particle rearrangement to allow for the growth of large crystals.

When the substrate–NP attraction is not fully screened, various types of anomalous NP diffusion have been observed. Alivisatos and co-workers constructed a deep neural network for analyzing anomalous NP trajectories and conducted extensive statistical tests on NP trajectories captured at different conditions (Figure 12).⁹⁸ They showed that the anomalous

to facilitate the understanding of substrate-mediated NP motions.

Note that the ligand effect on the NP–substrate interaction is prominent when electrostatic interactions are dominant. The NP–substrate interaction can also ubiquitously include vdW interactions. For example, oxide or mineral NPs possess similar composition to the SiN substrate and thus have fairly high Hamaker constants, leading to a non-negligible vdW attraction. For those systems, LP-TEM studies have focused mostly on nucleation and growth of NPs, which does not require fast NP motions.

2.4.3. Mapping Interparticle Interaction through Trajectory Sampling. Ligand molecules impact different types of interparticle interactions, such as electrostatic interactions, hydrophobic attraction, and steric hindrance. Two routes have been taken to understand these effects. One is to model each contribution of the pairwise interaction (see below), and the other is to measure the total pairwise interaction directly from experimental data of NP trajectories. In the conditions where NPs move and interact, their trajectories can be analyzed in two different ways to derive the pairwise interaction.

To model interparticle interactions, either Boltzmann inversion has been used, for dilute systems, or iterative Boltzmann inversion has been employed for more highly concentrated suspensions. Boltzmann inversion embodies the principle that at equilibrium, more frequently sampled states of the system are those with lower free energies. In this technique, the interaction potential $u(r, \theta)$, corresponding to the total free energy of an interacting pair of NPs at equilibrium can be obtained using $u(r, \theta) = -k_B T \ln g(r, \theta)$ where $g(r, \theta)$ is the radial distribution function. Previous studies on gold nanorods,⁹⁹ gold nanospheres,¹⁰⁰ and gold triangular prisms¹⁰¹ have shown that $g(r, \theta)$ can be tracked from LP-TEM movies. This function describes the normalized particle density at a distance r and relative orientation θ from a reference particle which can be obtained from the pairwise positions sampled by the NP during motions. Besides traditional NP tracking based on thresholding the NP features from the background, Chen and co-workers also developed a U-Net neural network-based analysis which can single out NPs from the background without setting a background. This method is particularly useful for movies of a low signal-to-noise ratio where not a suitable threshold can be found (Figure 13a).¹⁰¹ This method works well when the system reaches equilibrium and has significant statistics. The resolution of the interaction profile is only limited by the spatial resolution of NP tracking.

The other method is to map the pairwise Brownian force, which is the major driving force of particle motion, based on experimental NP trajectories and the fluctuation–dissipation theorem, which describes the forces involved in Brownian motion.¹⁰² A force–distance profile between a pair of interacting NPs can be measured from the relative velocity and diffusion coefficient of the pair. This method has been demonstrated in previous work on PtFe^{103,104} and Au NPs³⁶ (Figure 13b,c). This workflow can apply to a single pair of NPs in heterogeneous suspensions (e.g., due to high NP polydispersity) provided a sufficient range of interparticle distances is sampled. The Brownian force obtained from this analysis can be then combined with other forces (often calculated from theoretical models) to derive the total pairwise interaction between NPs. At higher NP concentrations, NPs can self-assemble into complex structures exhibiting collective dynamics. In this scenario, the

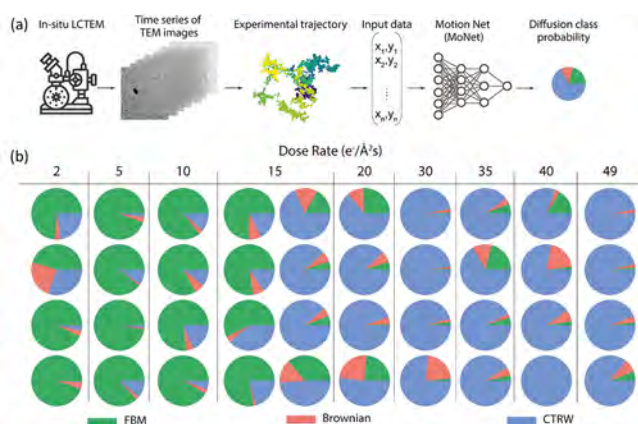


Figure 12. Deep neural-network workflow for anomalous diffusion classification on NP motions captured by LP-TEM.⁹⁸ (a) Deep neural-network pipeline for anomalous diffusion classification on in situ LP-TEM data using MoNet. (b) Neural-network analysis results for all trajectories studied as a function of dose rate (increasing from left to right across the table). Pie charts show the diffusion class probability where at low dose rates, there is a higher probability associated with an FBM (green), and at high dose rates, there is a higher probability associated with a CTRW (blue). Reproduced with permission from ref 98. Copyright 2021 National Academy of Science.

motions exhibit a continuous-time random walk (CTRW) which involves stop-and-go motion due to heterogeneous surface pinning (i.e., transient surface adsorption), fractional Brownian motion (FBM) usually attributed to viscoelastic liquid environment, and Brownian motion. Using their convolutional neural network (MoNet), they were able to determine the fractions of the different diffusion modes within a NP trajectory,

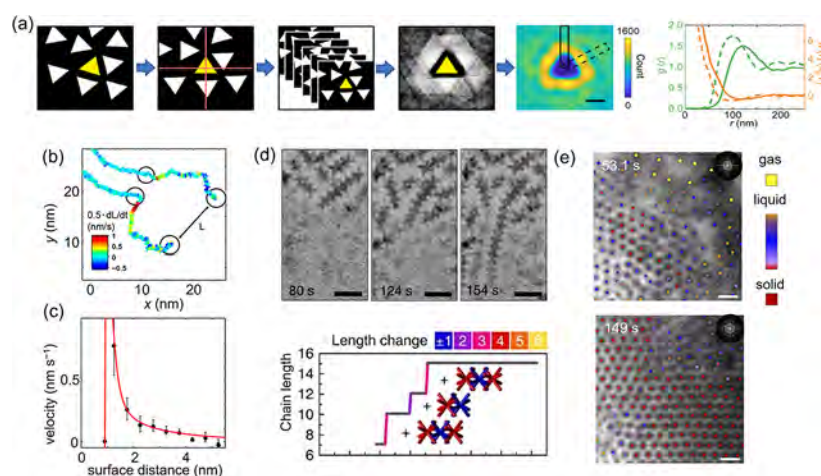


Figure 13. Mapping interaction potentials of NPs through trajectory sampling. (a) Elucidation of effective pairwise interaction mapping of gold triangular prisms based on Boltzmann inversion: 2D distribution map with accumulated statistics from a pair of particles where one of them is centered (yellow) and the others undergo motions.¹⁰¹ Reproduced with permission from ref 101. Copyright 2020 American Chemical Society through open access of ACS Author Choice License. (b) Tracked paths of two nearby NPs, color coded based on the estimated relative particle velocity.¹⁰⁴ Reproduced with permission from ref 104. Copyright 2017 American Chemical Society. (c) Averaged data for relative velocity versus surface-to-surface distance between particles (black).¹⁰⁴ The fitted line (red) shows the fitted interparticle forces. Reproduced with permission from ref 104. Copyright 2017 American Chemical Society. (d) LP-TEM images and growth kinetics of CdSe octapods into interlocked chains.¹⁰⁵ Reproduced with permission from ref 105. Open access. Copyright 2016 Springer Nature. (e) Phase coordinates tracking both the local density and local structure of NPs demonstrating the nonclassical nucleation pathway with amorphous intermediates.⁹⁷ Reproduced with permission from ref 97. Copyright 2019 under exclusive license to Springer Nature Limited. Scale bar: 200 nm.

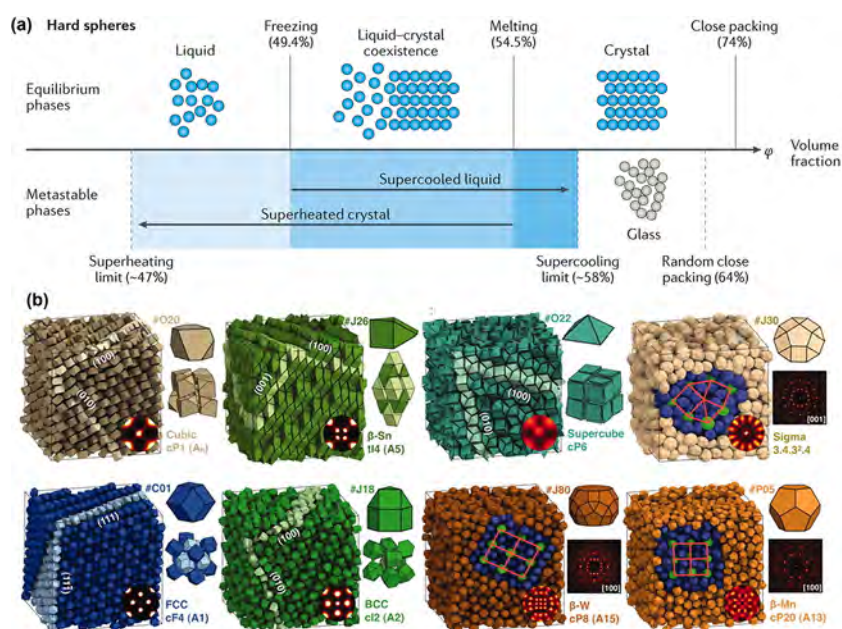


Figure 14. The formation of close-packed lattices from various shaped particles that can be described as hard colloids. (a) Schematic of how hard spheres can pack into crystals as the particle concentration increases, driven by increased translational entropy.¹⁰⁷ Reproduced with permission from ref 107. Copyright 2016 Macmillan Publishers Limited. (b) Simulation results of differently shaped NPs forming into various types of close-packed structures.¹⁰⁶ Reproduced with permission from ref 106. Copyright 2012 American Association for the Advancement of Science.

tracking of individual NPs allows for analysis of structural motifs and growth laws, such as the step-growth polymerization kinetics observed in the tip-to-tip assembly of gold triangular prisms⁹⁷ and the statistical mechanical model for the interlocked assembly of CdSe/CdS octapods (Figure 13d).¹⁰⁵ In the case of NP assembly into highly ordered supracrystals, phase-coordinate tracking of both the local density and local structural order of NPs elucidated a remarkable nonclassical nucleation pathway with amorphous intermediates (Figure 13e).⁹⁷

2.5. Nanoparticle Shape Effects

In NP assembly studies, NP shapes are regarded as the foremost parameter to encode interparticle interactions and the resulting equilibrium assembly. Frankel, Glotzer, and other pioneers have established from both statistical thermodynamics principles and large-scale computer simulations that in the limit of “hard colloids,” the shapes of NPs govern the packing symmetry and volume fraction of the final assembled superlattices to maximize the translational entropy of the whole NP ensemble.¹⁰⁶ Here

“hard colloids” refers to the ideal case when particles only interact via excluded volume repulsion defined by the particle shape, and crystallization can be driven by an order-from-disorder process (Figure 14a). Historically, hard colloids were experimentally realized as model systems when they did not have surface charges (thus no electrostatic effect) and were dispersed in a solvent which has an identical refractive index to the colloids to cancel vdW attraction. Classical examples of hard colloids include poly(methyl methacrylate) dispersed in hydrocarbon solvent and poly(*N*-isopropylacrylamide) in water.¹⁰⁷ Yet, in practice, the principle of hard colloids applies well to uncharged metallic and oxide NPs coated with hydrocarbon ligands, where the steric hindrance of the ligands merely increases the “effective” size of the NPs. For example, a diversity of single-component or binary lattices have been assembled from these NPs by solvent evaporation or interfacial self-assembly, so as to increase NP concentration.³⁸ The underpinning goal of entropy maximization in hard colloids is achieved in closely packed lattices given the geometric dimensions of the NPs, because the NPs at the lattice sites collectively attain the largest open space for translational degrees of freedom, in comparison with NPs in disordered and open lattices at the same NP concentration. In the case of binary lattices, the size ratio of large to small NPs can be varied such that the smaller NPs can occupy the interstitial spaces of the lattices formed by the large NPs.

For nonspherical NPs that can be modeled as hard colloids, the excluded volume can be quantified as a “directional entropic bond” in simulations,¹⁰⁸ which has been shown to drive the thermodynamic assembly of NPs into a full “periodic table” of closely packed structures, including space-filling lattices (from cubes, triangular plates, etc.), quasicrystals (from pentagons, tetrahedra, binary mixture, etc.), and plastic crystal (Figure 14b).¹⁰⁶ Such simulations are possible for large-scale (including hundreds to thousands of NPs) systems by efficiently modeling the excluded volume repulsion as a simple geometry rule that no shape boundaries of the NPs can intercept one another, thus reducing the computational cost. Using this method, while ignoring the hydrodynamics of the particles involved in self-assembly (as pointed out in section 2.3), the effects of nanoscale shape details, such as truncation of polygonal shaped NPs, have been studied to show how the extent of truncation can drastically change the lattice types.¹⁰⁹ Real-time nucleation pathways of NPs have also been simulated in 2019, where the entropic colloidal crystallization of hard colloids was shown to involve a 2-step crystallization through a high-density prenucleation precursor fluid phase with prenucleation motifs in the form of clusters, fibers and layers, and networks, all fundamentally depending on the NP shape.¹¹⁰ Highly complicated lattices can be simulated, including chiral, quasi-crystal, and crystals with a huge unit cell (see the example of 432 NPs in a cubic unit cell). Moreover, in this framework of nonspherical “hard” colloids, inverse design to predict the needed NP shape toward a targeted lattice structure can be achieved through an iterative optimization of building block shapes as demonstrated by Glotzer and her co-workers.¹¹¹

For NPs that cannot be modeled as hard colloids, NP shape can regulate interparticle interactions through the volume (all atoms inside NP matter) or surface contour, where ligand effects dominate. Those systems are considered on a case-by-case basis. For charged metallic NPs dispersed in aqueous solution, the major interactions are vdW attraction and electrostatic repulsion. Both interactions can be computed on the pairwise

level by a coarse-grained (CG) model, where a metal NP coated with charged ligands can be discretized as a shape matrix consisting of beads (type 1 for the metal core and type 2 for surface ligands).⁹⁷ It is important that the beads are small enough to represent the full 3D volume of the NP shape, sometimes down to atom size (e.g., 3.3 Å for gold atoms) to include nanoscale details such as truncation or to construct a smooth facet. This CG model is based on DLVO theory, which assumes a linear superposition of vdW and electrostatic interactions (see section 2.1). For vdW attraction, the Hamaker constant of metals are 1 order of magnitude larger than hydrocarbon ligands, so the vdW contribution from the metals E_{vdw} is considered, following:

$$E_{\text{vdw}} = \sum_{\vec{R}_i} \sum_{\vec{R}_j} -\frac{A_{\text{H}}\sigma^6}{\pi^2|\vec{R}_i - \vec{R}_j|^6} \quad (9)$$

\vec{R}_i and \vec{R}_j represent position vectors of the i th and j th beads.

The sum over \vec{R}_i and \vec{R}_j goes over all the beads (σ is the size of bead type 1) in the two NPs, for calculation efficiency. A_{H} is the Hamaker constant (e.g., 10^{-19} J for gold–gold in water). Equation 9 implements the assumption that vdW attractions are additive, which applies to most metal NPs. In this calculation of vdW attraction, the whole 3D shape of NPs matters. Similarly, NP systems that interact through (magnetic) dipole–dipole interactions also have the dipole moment (determined by the atom positions within the NPs) and directions sculpted by the 3D NP shape. As shown in Zheng’s LP-TEM study of the growth and self-assembly of FePt NPs,¹⁰³ the dipole–dipole interaction of FePt NPs adapts its mathematical profile as the NPs change their shape during growth and drives the coalescence of NPs into elongated wires.

The electrostatic interactions, when charge–charge correlation can be neglected at low ionic strength (e.g., < 0.1 M),⁶⁹ can be effectively computed by treating each charged ligand molecule as one point charge, and by doing similar summation as eq 9 for the vdW interaction. The ligands are coated on the NP surface, so the surface profile of the NP shape is important. Specifically, the electrostatic repulsion energy (E_{el}) between the two NPs can be calculated by summing over a pairwise Yukawa potential based on the Debye–Hückel theory for all the ligand beads (type 2) of two NPs. Type 2 beads are positioned as a monolayer approximately a ligand length distance away from the core NP surface, with the packing density matching the charge density predicted by surface potential. Thus, E_{el} is given by

$$E_{\text{el}} = \sum_{\vec{R}_i} \sum_{\vec{R}_j} \frac{Z_i Z_j}{4\pi\epsilon\epsilon_0|\vec{R}_i - \vec{R}_j|} e^{-|\vec{R}_i - \vec{R}_j|/\lambda_D} \quad (10)$$

Here i and j are the i th unit charge on one NP and the j th unit charge on the other NP. The sum over \vec{R}_i and \vec{R}_j goes through all the charged ligand beads on the NP. Z is the effective charge of the ligand ($|Z| = 1$ e). ϵ ($= 78$) is the relative dielectric constant of water, and ϵ_0 is the vacuum permittivity. λ_D is the Debye length of the solution determined by the ionic strength I as described by eq 3. In this calculation, the surface contours of the NPs determine the positions of the ligands and the extent of the summation. Similar interactions determined by the surface ligands include steric hindrance due to extended hydrocarbon ligands (such as polymers), and solvation effects where solvent

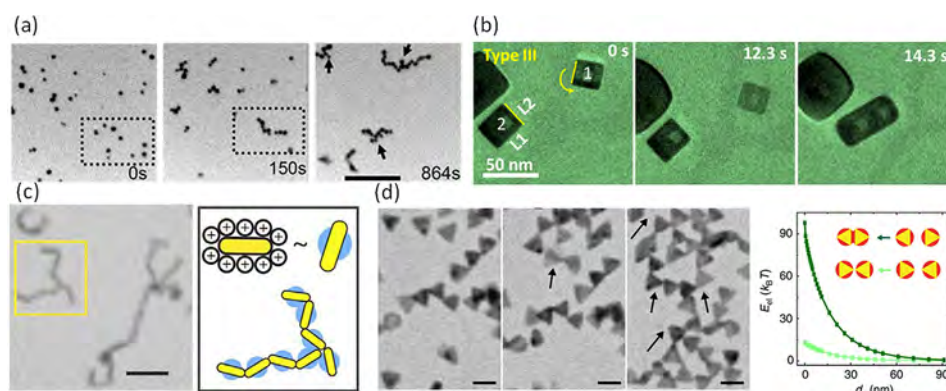


Figure 15. Assembly of differently shaped and charged metal NPs into end-to-end structures: (a) Au nanospheres.⁹⁵ Reproduced with permission from ref 95. Copyright 2013 American Chemical Society. (b) Ag nanocubes.¹¹⁵ Reproduced with permission from ref 115. Copyright 2018 American Chemical Society. (c) Au nanorods.⁹⁹ Reproduced with permission from ref 99. Open access. Copyright 2015 American Chemical Society under ACS Author Choice License. (d) Au triangular prisms.¹¹³ Reproduced with permission from ref 113. Copyright 2017 Spring Nature. Scale bars: 500 nm (a); 100 nm (c,d).

molecules reorient and arrange following the surface facets and curvature of NPs. The electrostatic interaction can have a range from Ångströms to hundreds of nanometers and are controlled by the ionic strength. Steric hindrance and solvation effects tend to be short-ranged and come into effect when the NPs are nearly in physical contact. Note that eq 9 and eq 10 do not consider many-body effects.

The above method of modeling the pairwise vdW and electrostatic interactions of charged metallic NPs has shown quantitative consistency with experimental results of NP assemblies studied by LP-TEM, such as gold nanorods,¹¹² nanoarrows,⁹⁶ and triangular nanoprisms.^{97,113} In all these examples, NP shapes sensitively fine-tune the interaction profiles, which often exhibits a secondary energy minimum that predicts the experimental equilibrium configuration of nearest neighbors. Because of electrostatic repulsions, non-closely packed structures inaccessible by “hard colloids” can be assembled, such as the nanorods formed from metal nanospheres and nanocubes (Figure 15a,b),^{95,114,115} end-to-end assembled gold nanorods⁹⁹ (Figure 15c), and triangular prisms (Figure 15d),¹¹³ as well as a hexagonal columnar phase of triangular prisms at high NP concentration.⁹⁷ In the latter case, at an ionic strength of 30 mM, while the vdW attraction favors planar stacking of the prisms in maximal registry, the electrostatic repulsion favors misalignment of the stacking prisms to minimize face–face electrostatic repulsion. This balance of interactions leads to a flattened enthalpic interaction potential around the perfectly aligned configuration, leading to an effective cylinder with a circular cross-section and a 3D hierarchical superlattice.

One limitation of CG-based interaction modeling is that one needs to enumerate and sample all the possible orientations and positions of two NPs in 3D to obtain the full pairwise interaction potential, which is computationally expensive. CG models work well for just two NPs and for assembly systems where the nearest neighboring pairwise interactions determine the final structure. For large-scale simulations that involve hundreds or even more NPs, one good strategy is to first use a CG model to calculate the pairwise NP interaction considering all the shape details of NPs and then fit the calculated interaction as a mathematical form (either by approximation or by iterative fitting based on a neural network). Thus, the mathematical form can be used as the input for large-scale simulations. Even in this case, to further reduce

the computational cost, simulations can adopt strategies such as “seed”, add some structural motifs of the final assemblies to expedite the system’s approaching to final assembly¹¹⁶ or start from a state that is close to the final structure and let it run to equilibrium.⁹⁷ Due to complicated effects of shape on enthalpic interactions, a universal workflow for simulation or prediction of assembly remains to be achieved. Reverse engineering also remains challenging.

3. ORIENTED ATTACHMENT AND CONTROLLING FACTORS

3.1. Crystallographic Orientation

3.1.1. Crystallographically Matched Attachments. The crystallographic coalignment of aggregating particles that leads to their oriented attachment can result from direction-dependent interactions associated with unique “crystallographically varying” material properties (e.g., dielectric properties and/or dipole moments), leading to torques that rotate nanocrystals into alignment. In addition to dipole characteristics known to be present in some mineral crystals, dielectric properties of mineral crystals are expected to exhibit spatial inhomogeneities, anisotropy, and nonlocality.^{117,118} Capturing these characteristics via classical MD simulations is challenging due to their intrinsically many-body nature.

The concept of a vdW torque, formulated by Parsegian and Weiss¹¹⁹ and initially introduced to explain the orientational adsorption of macromolecules on graphite surfaces,^{120,121} was more recently used to explain the orientational dependence of adhesion forces between rutile TiO₂ crystals.¹²² The mutual coalignment of ZnO nanocrystals observed in LP-TEM was understood by assessing the torque from a strong dipole–dipole interaction owing to the intrinsic dipole moment of ZnO.¹²³ Both sources of torque can only lead to an appreciable orientational alignment when they outcompete Brownian torque.^{120,121}

As expected, the continuum theory that considers many-body interactions at molecular dimensions to describe a macroscopic body requires correct values of subtle materials properties (e.g., the dielectric tensor as a function of frequency) that are often evaluated via a computational approach. This is especially true for vdW torque because a corresponding interaction is dominated by subtle dielectric spectra in the ultraviolet (UV)

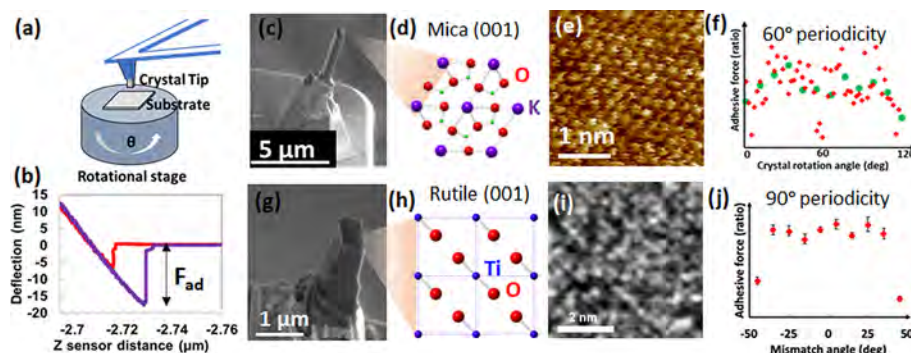


Figure 16. AFM-DFS force measurements show a 60° or a 90° periodicity of adhesive forces between mica–mica (001)⁷¹ or rutile–rutile (001)¹²⁶ surfaces, respectively, consistent with the symmetry of adsorbed water. (a) Schematic drawing of the AFM-DFS experimental setup, showing the crystal tip and substrate, which were aligned visually in the AFM. (b) A representative force curve. (c,g) SEM images of custom-made oriented single crystal AFM tips of mica (001) and rutile (001), respectively. (d,h) crystal structure of mica (001) and rutile (001) facets, respectively. (e,i) AFM images of mica (001) and rutile (001) facets in water, showing 6- and 4-fold symmetry, respectively. (f,j) Dependence of adhesive force (F_{ad}) on relative in-plane orientation for mica–mica and rutile–rutile surface interactions. (a,b,g,i,j) Reproduced with permission from ref 126. Copyright 2017 Royal Society of Chemistry. (c,f) Adapted with permission from ref 71. Copyright 2017 through the open access of the National Academy of Sciences.

range, rather than at the infrared range.⁶¹ For example, a tight-binding model, combined with a first-principles method, was used to obtain the anisotropy of the in-plane dielectric function of a graphite surface.¹²⁰ In addition to the properties of the particle, characteristics of the intervening medium are critical for determining the strength of the torque and the resulting orientation. “Screening” by the intervening medium, whose dielectric constant is inversely proportional to the strength of dipole–dipole torque,¹²³ is expected to reduce the vdW torque.⁶¹

Studies have shown that solvent-mediated free-energy barriers for nanocrystal aggregation can be facet dependent, thus promoting OA. For example, Raju, van Duin, and Fichthorn used MD simulations based on the ReaxFF reactive force field to show that approaching anatase nanocrystals with adsorbed water create a dynamic network of hydrogen bonds between surface hydroxyls and surface oxygens of the aggregating nanocrystals.¹²⁴ They showed that OA is dominant on surfaces that have the greatest propensity to dissociate water, consistent with experiment.¹²⁵

Using AFM-DFS (Figure 16a–g) to directly measure interparticle forces, Li et al. demonstrated that the adhesion forces (F_{ad}) between two mica (001)⁷¹ and two rutile (001)¹²⁶ surfaces have ~60° and 90° periodicity (Figure 16f,j), consistent with the 6-fold and 4-fold symmetry of the mica (001) and rutile (001) surfaces, respectively, as well as the adsorbed water (Figure 16e,i).⁷¹ A separate study on ZnO (0001) surface also revealed 60° periodicity, consistent with the 6-fold symmetry of ZnO (0001).¹²⁷ In the TiO₂ system, which is a classic OA system, within the measured 90° periodicity, the maximum and minimum forces appeared at mismatch angles of about 0° and ~±45°, respectively (Figure 16j). MD simulations predicted, in the case of two water layers between the surfaces, a 4-fold symmetric F_{ad} between (001) rutile surfaces with water dissociation results from the 4-fold symmetry of O_T–H_B pairwise interactions (Figure 17, O_T: terminated O, H_B: bridge H; simulation performed in vacuum with two layers of dissociated water). Additional longer-range forces, particularly vdW interactions that we expect to exhibit the 4-fold symmetry of the crystal lattice, may be needed to obtain a complete picture of TiO₂–TiO₂ interactions in water. Additional physics associated with the role of water, such as the hydrodynamics

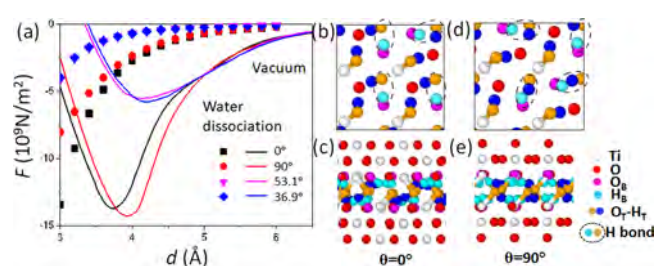


Figure 17. MD Simulations demonstrate a dependence of interparticle forces on crystallographic orientation driven by the structure of dissociated water on crystal surfaces.¹²⁶ (a) The interaction force per unit area, $F(\theta, d)$, in vacuum and with water surface dissociation as a function of d , for misorientation, $\theta = 0$ –90°. (b,d) Top views of two rutile (001) slabs with water dissociation at $\theta = 0^\circ$ and 90° , respectively. (c,e) Side views of two rutile (001) slabs with water dissociation at $\theta = 0^\circ$ and 90° , respectively. B, bridging; T, terminal. Reproduced with permission from ref 126. Copyright 2017 Royal Society of Chemistry..

of freely moving water molecules, will also need to be investigated to complete this picture.

3.1.2. Mismatched but Oriented Interfaces. Most OA occurs through perfect or twin-related crystallographic alignment of the particles, leading to interface-free single crystals or those with twin boundaries, respectively. Li’s group discovered mismatched but oriented interfaces (MOI) that produce diverse 3D structures of Ag₃PO₄ (i.e., symmetric and asymmetric polypods) composed of two or more tetrapods (Figure 18a).¹²⁸ TEM and SEM results (Figure 18b–e) suggest that interfaces of {100} and {110}({100}/{110}), {100}/{111}, {110}/{111}, and {100}/{100} have certain structural relationships corresponding to energy minima (Figure 18f) and coincident site lattices of interfacial atoms (the outlined orange and blues rectangles in Figure 18g), as demonstrated by MD simulations. Density functional theory (DFT) calculations (Figure 18g,h) indicate that the formation of pyrophosphate and/or phosphate rotation across the interface, as well as deformation of Ag–O bonds, compensates for the lattice mismatch at the interfaces.

Mismatched interfaces generally are highly strained, leading to large energy barriers to formation. However, pyrophosphates are known to be flexible and can relieve deformation, as manifest by a wide range of P–O_B–P bond angles (123°–180°).¹²⁹ The rotation of PO₄^{3−} tetrahedra in pyrophosphate allows for

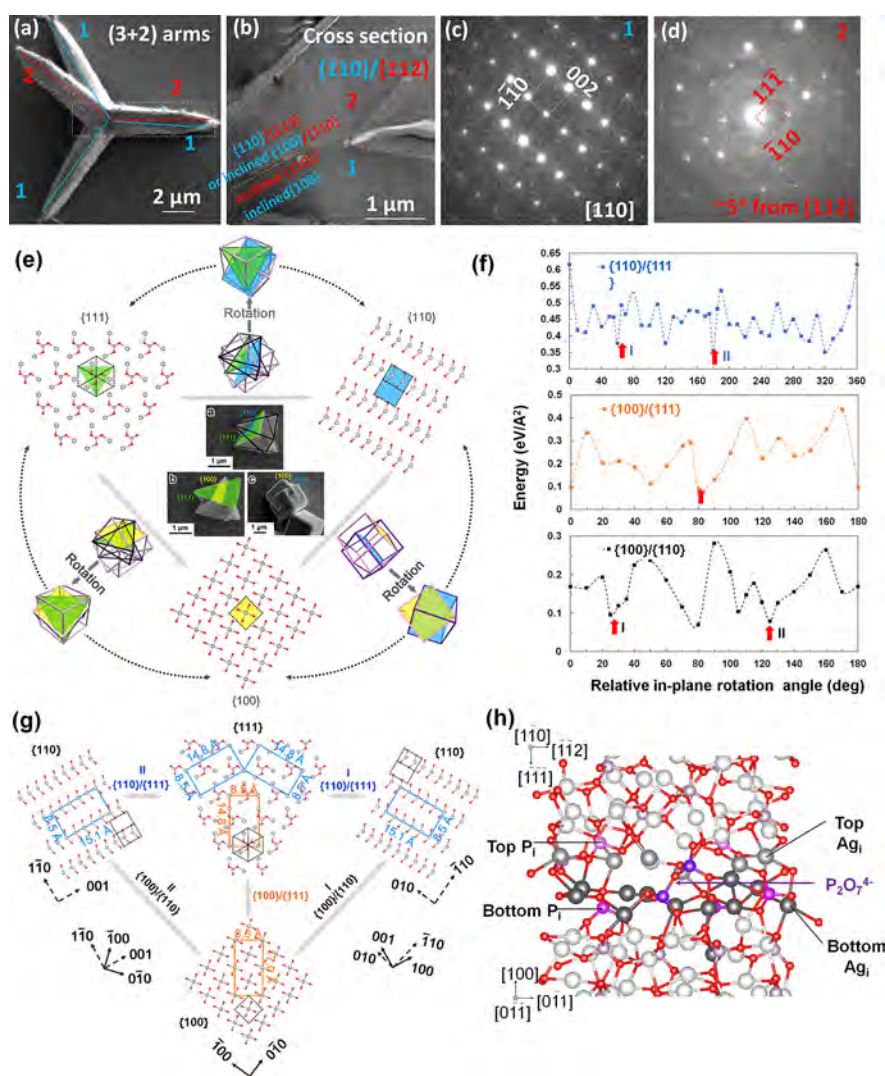


Figure 18. Mismatched but oriented interfaces.¹²⁸ (a) SEM images of Ag_3PO_4 tetrapods. (b) Cross-sectional TEM image of the polypods in (a). (c,d) Selected area electron diffraction patterns of arms 1 and 2, respectively. (e) Orientational relationships between Ag_3PO_4 surfaces based on SEM images of intergrown tetrahedral and cuboidal aggregates. (f) Plots of interfacial energy obtained via MD as a function of in-plane rotation angle θ . Red arrows correspond to the MOIs that are observed from experiments (SEM/TEM) consistent with the MOIs that can form supercells. (g) Ag and O atom arrangements at the $\{100\}$, $\{110\}$, and $\{111\}$ planes; similarity of the lateral supercells, indicated with colored rectangles, suggests the possibility that MOIs enable the formation of $\{100\}/\{111\}$ (orange rectangles) and $\{111\}/\{110\}$ (blue rectangles) interfaces. Black dotted lines show unit cells. (h) Side view of the interfacial atomic structures of MOI $\{100\}/\{111\}$, showing the formation of a pyrophosphate across the interface. Adapted with permission from ref 128. Copyright 2021 Elsevier BV.

distortion of the crystal. The formation of pyrophosphate takes place with a large rotation of phosphate ($\sim 40^\circ$). The energy cost associated with this rotation of the phosphate groups can be readily offset by the formation of pyrophosphate, stabilizing the mismatched interface. Two mechanisms were proposed for the growth of asymmetric polypods: (1) nucleation of a pyrophosphate, followed by growth through ion-by-ion addition, which disrupts the crystal symmetry, and (2) attachment of small Ag_3PO_4 NPs in an oriented fashion via the formation of pyrophosphate across the interfaces, which disrupts the crystal symmetry. Notably, the two interfacial planes are not perfectly parallel to each other. The lattices can accommodate large distortions via rotation of the phosphate groups and the flexibility of the Ag–O bond lengths and O–Ag–O angles. The ions of PO_4^{3-} or Ag^+ from the reaction solution can bridge the gap by forming $\text{O}_3\text{P–O–Ag–O–PO}_3$ or $\text{O}_3\text{P–O}_\text{B–PO}_3$ linkages across the interface.

3.2. Effect of Interfacial Liquid–Solid Structure

Unlike the isotropic bulk solution that is far from a particle surface, within a nm or so of a surface, the solution exhibits a heterogeneous structure.¹³⁰ Due to confinement effects, variations in solution density in the direction perpendicular to the surface occur on the length scale of a solvent molecule (~ 3 Å in the case of water), while in the lateral direction, the variations occur on the length scale of the substrate lattice. For inorganic crystalline particles, the latter is also on the order of a few angstroms, as shown, for example, by 3D fast force mapping (FFM) in aqueous solution above the (110) face of boehmite (AlOOH)¹³⁰ (Figure 19a,b), which is a face on which platelets of boehmite undergo OA.⁷⁶

Such solution structures near particle surfaces have significant consequences on long- and short-range forces between NPs. When two colloidal particles come within nanometer distances in a liquid solvent, the solvent can mediate a force between them.

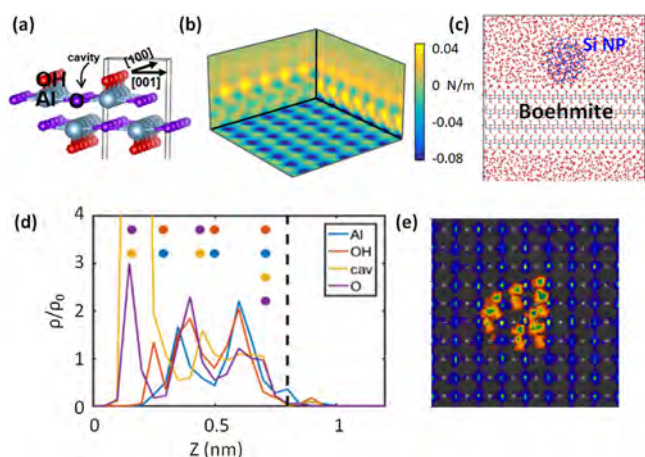


Figure 19. FFM provides atomic-level maps of solvent structure interpretable in terms of tip-solvent interactions via MD.¹³⁰ (a) Boehmite (AlOOH) structure. (b) FFM map of force gradient in three orthogonal planes above boehmite. (c) Simulation cell of silica particle representing AFM tip above boehmite in water. (d) Predicted water density (relative to bulk) vs height above distinct atomic sites. Dots indicate locations of peaks in (b). (e) Pattern of H₂O (blue) and oxygens of OH (gray) in first hydration layer, as well as silanols on the tip (orange/green) that H-bond to H₂O molecules in the first layer, thus defining the observed hydration structure. (a–d) Adapted with permission from ref 130. Open Access License. Copyright 2021 American Chemical Society.

This solvation force (or hydration force) is due to differences between solvent ordering and/or density in the gap between the particles and in the bulk liquid region around them.⁷⁹ When defining the interparticle potentials that drive particle assembly, in contrast to the well-known vdW, ion correlation, and electrostatic interactions discussed above, the role of interfacial solution structure has only recently been explored. Along with simple physical arguments on ion hydration, Li et al.'s study⁷¹ based on AFM-DFS measurements revealed that a consideration of the solution structure at interface is necessary to understand the adhesion forces between mica surfaces (Figure 4), leading to reasonable explanations for nontrivial dependence of the adhesion forces on ion concentration and specificity (e.g., Na⁺ vs K⁺). Similarly, Zhang et al.¹³¹ used AFM-DFS measurements to quantify the orientation dependence of the adhesion force

between complementary (0001) faces of the polar crystal ZnO, finding that the symmetry mirrored that of the crystal lattice. Furthermore, Lee et al.¹³² demonstrated that the solution structure near NP surfaces, probed by amplitude modulated AFM (AM-AFM) and correlated to layers of hydrated ions adsorbed on the NP surface, are directly responsible for a distinct distribution of separations between Ag NPs at transient and final superlattice structures (Figure 5). This clearly indicates that solution structures can even influence collective responses of NPs.

Recent simulation and theoretical studies demonstrated two important effects of solution structures on particle interaction forces.^{23,133–137} The first is a significant orientation dependence of the potential (Figure 20a). Simulations on a number of systems^{126,130,135,137,138} (TiO₂, ZnO, MgO, boehmite, muscovite, and pyrophyllite) predict that the free energy vs separation between atomically flat crystal surfaces in water varies between minima and maxima that correspond to the number of water layers between the surfaces for separations of ~1 nm (~3 water layers) or less and that the minima are deepest for perfect crystallographic alignment and shallowest, or eliminated, for maximum misalignment. However, the results also consistently predict a second effect: these density variations produce barriers between adjacent minima that are many tens of kT even for contact areas of less than 10 nm² (Figure 20a). The simulations also predict that the oscillations in water density and corresponding forces scale with surface hydrophobicity (Figure 20b,c).¹³⁵ Finally, we note that none of the simulations of particle-particle interactions done to date include surface reactions, such as hydroxylation, yet simulations of water structure near AlOOH surfaces show that hydroxylation is an important factor in the predicted distribution of water, especially as surfaces approach contact where hydroxyl groups on one surface can interact with those on the other (Figure 19c–e).¹³⁰ Consequently, much research is still needed to connect the atomic-scale structure and chemistry of particle surfaces to the complex set of barriers and potential minima created by solution structuring that both pull particles toward one another and keep them apart.

Solution structures near particle surfaces can bring additional consequences. A recent study based on AFM-based 3D-FFM¹³⁰ suggested that the solution structure can cause unusual transport properties under confinement, leading to “conservative” hydro-

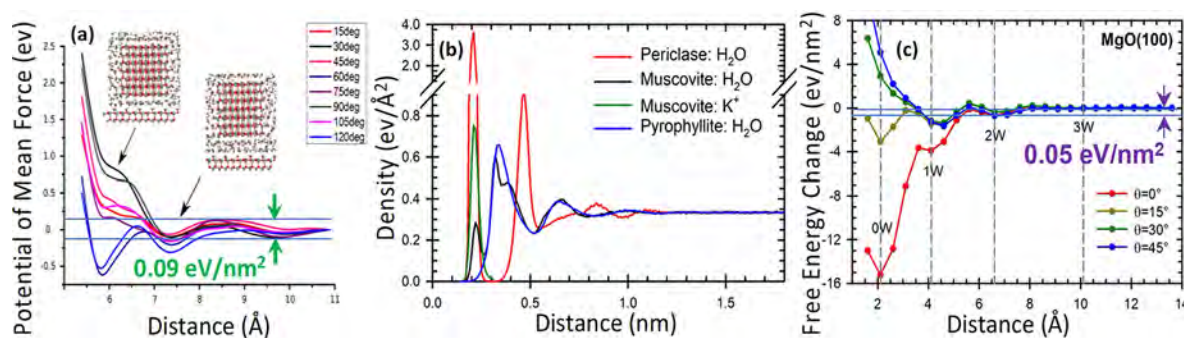


Figure 20. Simulations predict a dependence of interparticle potentials on relative orientation driven by hydration structure, which is strongly impacted by surface hydrophobicity. (a) Potential of mean force vs distance between ZnO surfaces showing minima that correspond to integer numbers of water layers and barriers between minima equivalent to ~40 kT for a 10 nm² contact area.¹³¹ (b) Effect of hydrophobicity on water density, with periclase (MgO) being most hydrophilic and pyrophyllite most hydrophobic. (c) Free energy vs distance between MgO surfaces for water structure in (b) showing strong orientation dependence and sizable barriers.¹³⁵ (a) Adapted with permission from ref 131. Open Access License. Copyright 2017 Springer Nature. (b,c) Adapted with permission from ref 135. Copyright 2020 American Chemical Society.

dynamic forces at ~ 1 nm of solution layer. This is, in fact, well-aligned with many previous studies observing chemistry-dependent transport properties in confined liquids (e.g., viscoelasticity^{139,140}). Similarly, an unusual dielectric property of confined water associated with solution structures (~ 2 instead of a well-known bulk value, ~ 80) was also reported.¹⁴¹ These facts illustrate convincingly that the solution structure influences dynamic contributions, as well as energetic contributions, to particle assembly. Note that this nature is especially important for understanding the last stage of particle assembly and OA where physical contact of NPs occurs.

Solvent-mediated forces can have interesting consequences for particle-mediated growth, as recently reviewed by Sushko.¹⁴²

Figure 21 depicts the concept of solvent-mediated forces for two

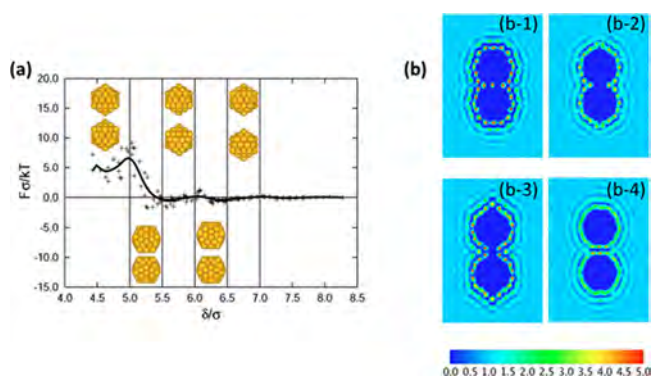


Figure 21. Solvation force and its dependence on solvent ordering in the interparticle gap.¹⁴³ (a) Mean dimensionless force F , where F has units of kT/σ and σ is the Lennard-Jones distance parameter, along with particle configurations as two Au icosahedra approach one another. It is seen that the particles alternate between face-to-face and vertex-to-vertex configurations as they approach one another in solution. (b) Heat map showing the solvent density relative to the bulk solvent density (the normalized bulk density is 1.0) at selected NP separations. (b-1) A fixed face–face configuration at a separation of $\delta = 4.63\sigma$. (b-2) Corresponding average rotational density profile of (b-1), where the particles assume a vertex–vertex orientation to minimize the solvent density in the interparticle gap. (b-3) A fixed vertex–vertex configuration with a separation of $\delta = 6.08\sigma$. (b-4) The average rotational density profile of (b-3), where the particles assume a face–face configuration. Reproduced with permission from ref 143. Copyright 2006 American Physical Society..

metal icosahedra in Lennard-Jones solvent.¹⁴³ In Figure 21a, the mean interparticle force between the two particles is shown as a function of their separation. Preferred orientations of the particles are shown for various separations, and it is seen that the particles alternate between face-to-face and vertex-to-vertex orientations as they approach one another in solution. The heat map in Figure 21b shows the solvent density relative to the bulk density for the two particles. Generally, there are oscillatory solvent density profiles around the two particles, which stem from solvent ordering at the particle surfaces and layering away from the surfaces. In Figure 21 (b-1) and (b-2), the distance δ between the two particles is fixed at $\delta = 4.63\sigma$, where σ is the Lennard-Jones distance parameter. In (b-1) the particles are held in the face-to-face configuration, and in (b-2) the particles are in their preferred configuration in Figure 21. There are regions of high solvent density in the interparticle gap in (b-1), while there is vacuum in (b-2). Similarly, in (b-3) and (b-4), the two particles are held at a distance of $\delta = 6.08\sigma$, where the face-

to-face configuration in (b-4) is preferred, and we see high-density regions in (b-3).

Kerisit and De Yoreo recently used classical MD simulations to compute the free energy landscape of aqueous NPs approaching mineral substrates with variable hydrophilicity.¹⁴⁴ They showed that the interfacial water structure created free energy minima for NP approach that corresponded to integer numbers of intervening water layers. The depth of the free-energy minima and the free-energy barriers between minima depended on the hydrophilicity of the mineral surface. The results help explain the formation of mesocrystals and the observed ability of NPs to rotate before attachment while in a long-lived solvent-separated state. In a more direct probe of solvent-mediated forces, Zhang and co-workers used both experiments and MD simulations to probe solvent-mediated forces between ZnO NPs in aqueous solution. Their simulations also exhibited water layering in the interparticle gap and their calculated potentials of mean force agreed well with experiment.¹⁴⁵

3.3. Interface-Driven Nucleation and OA of Crystals

One of the most consequential discoveries to arise from studies of crystal growth through assembly and fusion of particles in recent years is that the effect of the mineral surface on local solution structure extends to the equilibrium thermodynamic solution properties in the interfacial region. Both studies in which this effect was manifest involved organic ligands that bind to the faces of the particles. In the first, hematite (Fe_2O_3 , Hm) crystals were formed from ferrihydrite (FeOOH , Fh) suspensions (Figure 22a) at 80°C .²⁶ When pure Fh suspensions

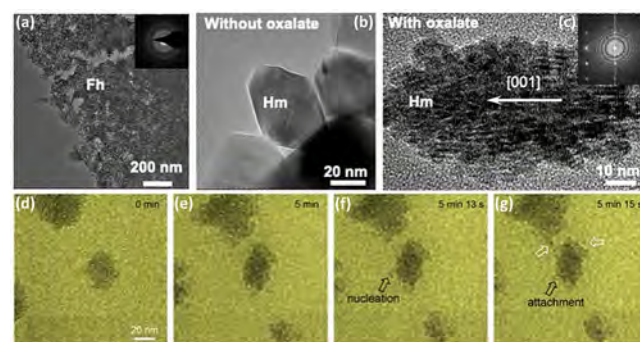


Figure 22. When incubated at slightly elevated temperature, Fh converts to Hm, producing well-faceted single crystals in pure solution, but spindle-shaped mesocrystals through a process of interfacially driven nucleation followed by OA when oxalate is present.²⁶ (a) Fh precursor NPs. (b) Hematite single crystals formed at 80°C . (c) Hematite mesocrystal formed in the presence of sodium oxalate. (d–g) Series of in situ TEM images collected at 80°C documenting the mechanism of mesocrystal development. (a,b) and (d–g) Adapted with permission from ref 26. Copyright 2021 Springer Nature. Under exclusive license to Springer Nature Limited.

were used, well faceted Hm single crystals formed (Figure 22b), but when sodium oxalate (Ox) was added to the suspension, spindle-shaped Hm mesocrystals were generated instead (Figure 22c). All particles were found to be crystallographically coaligned (Figure 22c) and all spindles were self-similar in geometry, with the long axis of the spindle running parallel to the Hm (001) direction. In situ TEM experiments performed at 80°C (Figure 22d–g) showed that isolated Hm particles rarely appeared, but once formed, new Hm particles began to nucleate repeatedly ~ 2 nm from their surfaces, to which they then

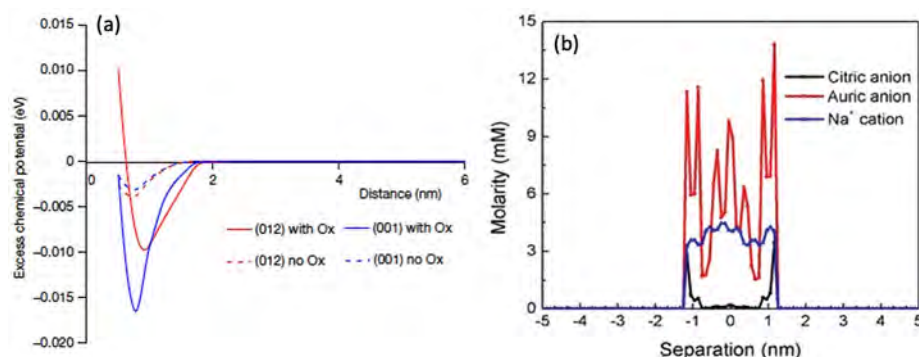


Figure 23. Surface-adsorbed organic ligands induce near-surface concentration gradients that can enhance the chemical driving force for nucleation of new particles. (a) Average potential of mean force of Fe ions versus distance away from the surface of oxalate-coated Hm.²⁶ (b) Ion distribution in the gap between two Au surfaces with an interparticle distance of 3 nm.⁷⁶ (a) Adapted with permission from ref 26. Copyright 2021 Springer Nature and The Author(s), under exclusive license to Springer Nature Limited. (b) Adapted with permission from ref 76. Copyright 2018 Royal Society of Chemistry.

attached, thereby generating mesocrystals, though whether the particles are aligned at the time of nucleation or rotate into alignment during the attachment phase could not be discerned. Thus, the rate of crystal growth by particle attachment and the morphology of the resulting mesocrystals were set by the facet-specific rate of interfacially driven nucleation. Both measurements and simulations showed that Ox binds to Hm with a coverage that is facet specific. The simulations predicted interfacial gradients in speciation near the Ox-covered surfaces, leading to a peak in excess Fe^{3+} concentration about 1 nm from the surface due to attraction by the negatively charged surface-bound ligands (Figure 23a). These simulations also predicted a barrier-free attractive interparticle potential for particles separated by less than ~ 2 nm.

A separate study on Au NP formation in the presence of citrate revealed a similar pathway with all Au nuclei appearing within 1 nm of existing particles.⁷⁶ The gap was closed either by a jump-to-contact or formation of a neck between the new and existing particles. Classical DFT (cDFT) again predicted that the presence of the negatively charged organic ligands led to a peak in excess Au ion concentration within a nm of the interface, corresponding to the same region where new particles formed and where the necks between particles grew (Figure 23b). However, the effect was predicted to be strongly pH dependent due to the role of ligand and solute ion valency in determining whether ligands or ions preferentially access the particle surface, as with the case of Hm mesocrystal formation. Once new Au NPs formed, an attractive interparticle potential drove the particles to attach to the growing aggregate.

In both of these examples, crystal growth by assembly of particles is a consequence of interface-driven nucleation in a system where the organic ligands attract solute ions, inhibit growth of newly formed NPs, and create an attractive interparticle interaction potential. Given that the chemical potential must be uniform throughout the solution, the dramatic enhancement of nucleation in the near-surface solution over that in the bulk must be attributable to one of two other factors that define the free energy barrier to nucleation: a decrease in mineral solubility, leading to an increase in local supersaturation, or a decrease in interfacial free energy.^{76,146} The former appears as inverse squared term in the barrier, while the latter is a cubic term. Because the nucleation rate is exponential in the barrier, even small changes in these quantities can increase rates by many

orders of magnitude, thus a multiparticle environment driven to assembly.

4. OA-INDUCED CRYSTAL STRUCTURES

OA processes can direct 1D–3D nano/microstructures of materials (e.g., nanowires,⁶ nanosheets,¹⁴⁷ and branched or hierarchical structures⁶) and atomic lattice structures (e.g., twin related structures³⁴ and defects³⁵).

4.1. 1D Nanowires, 2D Nanosheets, and 3D Branched Nanostructures

4.1.1. 1D Nanowires. Recent studies have emphasized that for two particles to be able to aggregate, solvent and/or adsorbed ligands must leave the interparticle gap, and the way in which this occurs can have interesting consequences for the morphology of the aggregate. For example, Sathiyarayanan et al. showed that because Lennard-Jones solvent cannot easily form protective layers near Ag nanocrystal corners and edges, two nanocrystals tend to aggregate near their corners and edges.¹⁴⁸ Furthermore, the more developed ordering on large nanocrystal facets than on small ones tends to promote 1D nanocrystal growth.¹⁴⁸ In recent studies with LP-TEM, Dong et al. found evidence for these predicted aggregation tendencies.¹⁴⁹ They observed the aggregative growth mechanisms of sub-10 nm Ag NPs in water. As shown in Figure 24, they found that small Ag NPs tended to aggregate into chains to form nanorods, a phenomenon they attributed to weaker hydration forces at the nanorod ends.¹⁴⁹

Halder and Ravishankar reported the synthesis of Au nanowires capped with oleylamine from the OA of Au cuboctahedra.¹⁵⁰ As shown in Figure 25a, they observed that Au cuboctahedra formed in the initial stages of their synthesis. Over time, the nanocrystals disappeared, and nanowires emerged, as shown in Figure 25b. They proposed that the formation of nanowires occurred via OA of the NPs on their {111} facets because the diameters of the wires were virtually identical to the diameters of the nanocrystals in the solution. Additionally, the defects they observed in the nanowires were characteristic of {111} aggregation, as shown in Figure 25c.

4.1.2. 2D Structures. 2D structures have also been proposed to grow via OA.^{84,85,151,152} For example, Yang et al. showed that cobalt oxide and cobalt nickel oxide can form 2D nanosheets from the shape transformation of 3D nanocrystal intermediates in a solution-phase synthesis.¹⁵¹ Using LP-TEM, they observed 3D NPs form from cobalt and nickel precursors.

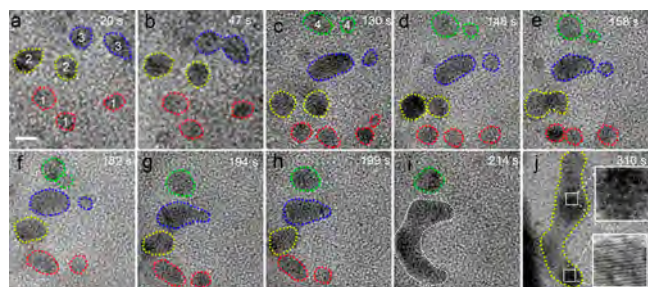


Figure 24. Snapshots of the growth trajectory of a Ag nanorod originating from four groups (termed 1, 2, 3, and 4) of Ag NPs randomly dispersed in a liquid cell.¹⁴⁹ Different groups of NPs are highlighted by dotted lines of different colors. Scale bar is 5 nm. Adapted with permission from ref 149. Copyright 2019 American Chemical Society.

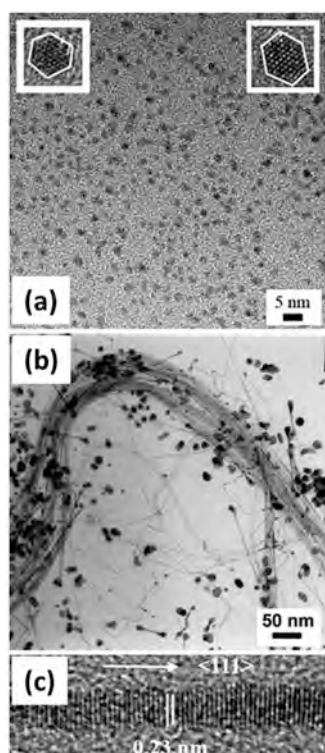


Figure 25. Au nanowires capped with oleylamine from the OA of Au cuboctahedra. (a) Bright-field TEM image of gold NPs. The insets show that the particles contain {111} and {100} facets. (b) Bundles of nanowires formed on aging. (c) A high-resolution image revealing that the growth direction of the wires was $\langle 111 \rangle$.¹⁵⁰ Adapted with permission from ref 150. Copyright 2007 Wiley.

Upon reaching a size of a few nanometers, 3D particles began to spread, developing a 2D region at their periphery, with the 3D region gradually disappearing. As they spread, neighboring nanosheets came into contact with each other and merged to form larger sheets by attaching at their edges. Although their analysis was focused on the 3D–2D transformation in this system,¹⁵² the final 2D plates were formed by OA. Further resolution of this aspect of their synthesis would be helpful.

4.1.3. 3D Structures. Rutile nanowires typically grow via OAs. As previously reported, anatase NPs initially form and then transform into rutile,¹⁵³ because anatase is more stable than rutile at small crystal sizes while rutile is a more stable phase at larger sizes.¹⁵⁴ Branched rutile nanowires (Figure 26a) also form

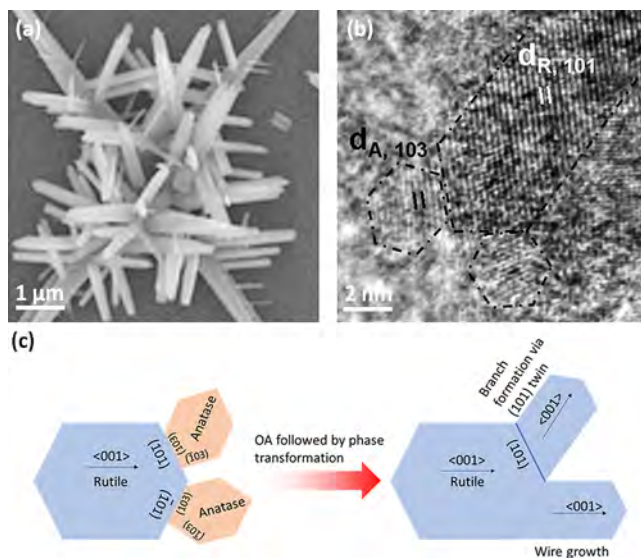


Figure 26. Wire and branch growth via OA of anatase {103} facets onto rutile {101} facets, followed by phase transformation from anatase into rutile.⁶ (a) SEM image of branched rutile wires. (b) High-resolution TEM image shows OAs of anatase {103} facets onto rutile {101} facets for short reaction times (~ 45 min.). (c) Schematic drawing showing wire and branch growth mechanisms. Adapted with permission from ref 6. Copyright 2013 American Chemical Society.

via OA on two distinct facets. During the growth, the {103} crystal facet of the anatase particle attaches in an oriented manner with the {101} crystal facet of rutile at the tip of a rutile nanowire. The following phase transformation from anatase into rutile results in either interface-free wire growth or the formation of branch via {101} twin interfaces with growth along $[001]$ directions (Figure 26b–c).⁶

4.2. Multiply Twinned Structures

Recently, Li's group revealed that repeated OA events by ~ 3 nm Au NPs create high-energy grain boundaries, that accumulate strain during atomic rearrangements and consequently decompose, inducing formation of 5-fold twins (5-FTs).³⁴ When a twinned crystal (with the first twin, $\Sigma 3_1$) undergoes OA with another single crystal, a second twin ($\Sigma 3_2$) forms, resulting in two types of concave surfaces with angles of $\sim 94^\circ$ and $\sim 150^\circ$ (Figure 27a,b and l,m). These events lead to two different mechanisms of 5-FT formation. In mechanism 1, on the resulting $\sim 94^\circ$ concave surface with two $\Sigma 3$ twin interfaces, the small radius of curvature provides a path that is far from equilibrium: a large strain quickly accumulates while the surface energy is minimized via atomic surface diffusion to the curved surface, resulting in lattice deformation and a high energy grain boundary (GB) $\Sigma 9$ (Figure 27c), which decomposes into another high energy GB $\Sigma 27$ and $\Sigma 3$ (Figure 27d–f). Analysis that includes MD simulations concludes that, to release this high strain energy, a small twin forms via slip on three consecutive {111} planes, which is a process that does not create extra strain in the nearby lattice or require high energy, i.e., there is zero net strain (Figure 27g,j).¹⁵⁵ Continuous nucleation and growth of this twin structure releases the strain, resulting in decomposition of $\Sigma 27$ into two $\Sigma 3$ interfaces and eventual formation of a 5-FT (Figure 27g,h and i–k).

In mechanism 2, on the resulting $\sim 150^\circ$ concave surfaces, OA only creates a small $\Sigma 9$ (Figure 27n) due to the large radius of curvature and the crystal lattice is less deformed than in

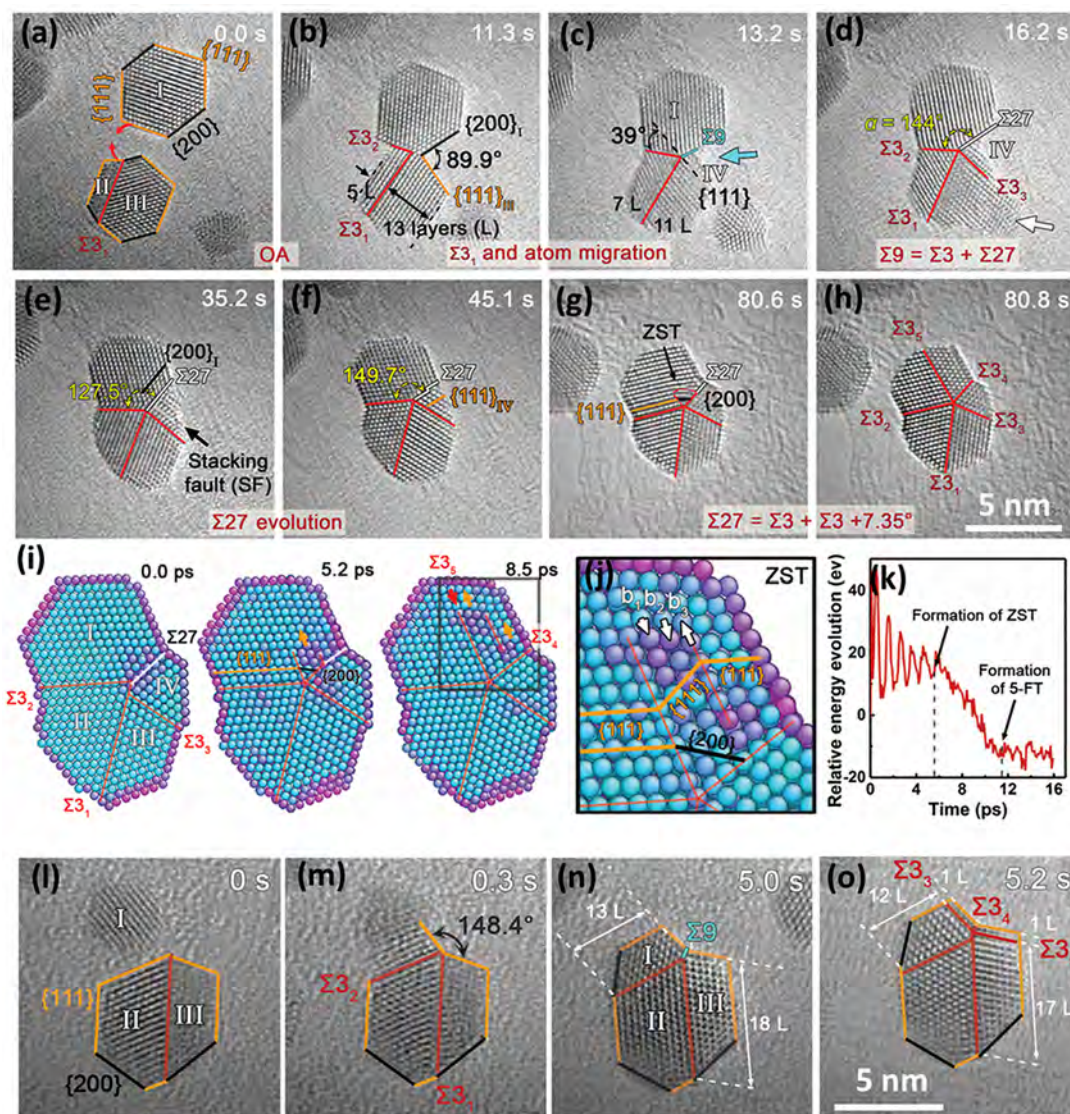


Figure 27. Two pathways of 5-FT formation with a $\sim 90^\circ$ or $\sim 150^\circ$ concave surface.³⁴ (a,b) Formation of Σ_3 and $\sim 90^\circ$ concave surface after the OA process. (c) Migration of atoms to the concave surface region (cyan arrow) with the formation of the Σ_9 GB and Σ_3 migration of two atomic layers toward region III from II. (d–f) Oscillation between $\Sigma 27$ -(200)_I and $\Sigma 27$ -(111)_{IV} and corresponding α of $\sim 125^\circ$ and $\sim 150^\circ$, respectively. (g) Nucleation of ZST on $\Sigma 27$ near twin pole. (h) Formation of 5-FT. (i) MD simulation. (j) Enlarged simulation image showing the ZST formation and growth. (k) Energy profile of the NP during decomposition of $\Sigma 27$. ZST: zero strain twin. (l,m) Formation of Σ_3 and $\sim 150^\circ$ concave surface after the OA process. (n) Migration of atoms to the concave surface region with the formation of the Σ_9 GB. (o) Formation of asymmetric 5-FT. Adapted with permission from ref 34. Copyright 2019 American Association for the Advancement of Science.

mechanism 1. Consequently, asymmetrical 5-FTs form via partial dislocation slipping of only a few layers of {111} planes (Figure 27o) because further slipping creates extra strain energy in the lattice due to large interfaces. In contrast, in mechanism 1, a highly strained lattice is already formed via surface diffusion after the OA event. The formation of 5-FTs within the bulk of the particle (i.e., with large interfaces) results in a reduction of strain. These two mechanisms are also applicable for high twin-fault energy systems, such as Pd and Pt, but result in smaller twinned units.³⁴

The growth path via repeated OA events may be general for a wide range of materials and enable the formation of structures with multiple grain boundaries, besides 5-FTs, depending on the specific crystal structure and the nature of twin boundaries in each system.

4.3. Necking

During OA of colloidal nanocrystals, a neck can be formed between nanocrystals,^{156–159} and it may strongly influence the properties of the resulting epitaxially connected nanocrystal superlattices. For example, superlattices with atomically uniform internanocrystal necks increase the electron delocalization length,^{160,161} which impacts the coherent coupling effects in superlattices^{162,163} and may induce various novel properties,^{162,164,165} e.g., topological states or Dirac cones.^{10,166,167} Thus, there has been significant interest in understanding the mechanism of neck formation, which is important not only for interpreting semiconductor crystallization through particle attachment¹⁶⁸ but also for improving the internanocrystal connectivity in nanocrystal superlattices to achieve the desired electronic properties.^{160,169}

It was assumed that necking may be achieved through a “click and cascade” model when two nanocrystals are at a short range and separated by solvent molecules.¹⁷⁰ However, measurements using X-ray scattering^{171–173} and ex situ TEM^{174–176} indicate that the center-to-center distance of epitaxially connected nanocrystals is often larger than the diameter of the initial nanocrystals,^{10,170} which suggests that necking is likely achieved through different mechanisms.

A study on OA of PbSe nanocrystals revealed the unique necking process by real-time atomic-resolution imaging using LP-TEM.¹⁷⁷ It was found that the necking occurred in three stages (Figure 28): (1) nanocrystals first approached each other

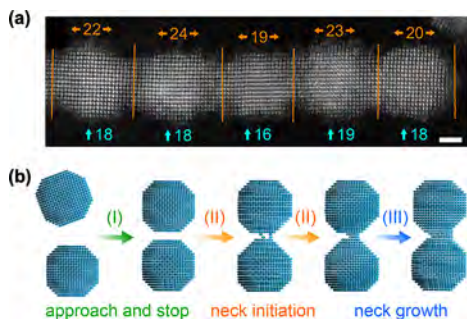


Figure 28. Necking of PbSe nanocrystals during assembly. (a) Representative HAADF-STEM image of a PbSe nanocrystal chain formed by oriented attachment.³⁷ Vertical lines denote the nanocrystal boundaries and labels indicate the number of Pb layers along the nanocrystal length (orange) and width (blue). Scale bar: 5 nm. Adapted with permission from ref 37. Copyright 2019 exclusive licensee American Association for the Advancement of Science. (b) Atomic model showing the atomistic pathway of neck formation between two PbSe nanocrystals.¹⁷⁷ Only Pb atoms are shown in the model for clarity. Adapted with permission from ref 178. Copyright 2019 Tsinghua University Press and Springer-Verlag.

and the lattice angle changed from $\sim 60^\circ$ to $\sim 90^\circ$, indicating the lattice geometry change from hexagonal to square, (2) the neck initiation occurred slowly (~ 10 s) when two nanocrystals approached to each other within an edge-to-edge distance of 0.6 nm. During neck initiation, Pb and Se atoms diffuse from other facets into the gap, forming “dynamic reversible” filaments. (3) Once the filament (neck) width is larger than a critical size of 0.9 nm, it gradually (in 15 s) widens into a 3 nm wide neck. The neck initiation and growth mechanisms were rationalized with DFT calculations.¹⁷⁷

4.4. Defects Induced by OA

During OA processes, in some cases, a slight misalignment upon attachment leads to defect formation at the interface, where the lattice planes are slightly bent due to the formation of dislocations. In the case of ferrihydrite, an iron oxyhydroxide (Figure 29a,b), LP-TEM showed that, within a few seconds of contact, edge dislocations formed upon attachment translated laterally across the interface (Figure 29b,d) via atomic diffusion in the crystal lattice and aqueous solution, leaving behind a perfect defect free interface (Figure 29d).³⁹

Through this understanding of OA mechanisms, a synthesis method was designed to guide the growth of crystals with desired defects to improve catalytic properties.³⁵ This synthesis method is based on the hypothesis that solvents of high viscosity slow atomic motion and thus potentially prevent self-elimination of edge dislocations that are formed during OA events. The growth of rutile has been reported to occur via OA,⁶

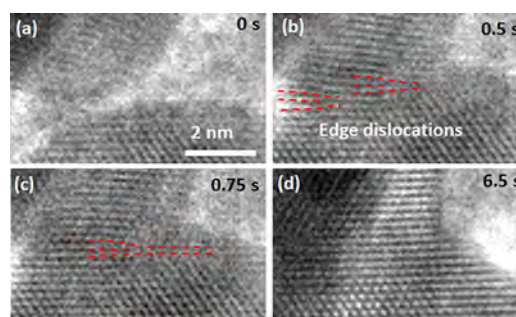


Figure 29. Sequence of TEM images of an OA event in ferrihydrite with a slight misalignment upon attachment, showing the formation of edge dislocations at the interface and their self-elimination.³⁹ Adapted with permission from ref 39. Copyright 2012 American Association for the Advancement of Science.

and edge dislocations in TiO_2 introduce Ti^{3+} sites, which are predicted to be weak recombination centers. Thus, these sites could potentially improve photoactivity in visible light, but this improvement had been neither proven nor realized due to the experimental difficulties of obtaining sufficient dislocations in the crystal lattice. Ethylene glycol with a nearly 100 times higher viscosity than water was chosen as the solvent during the synthesis.¹⁷⁸ Using a simple, one-step hydrosolvothermal method, colored ultrafine nanowires of rutile (B-R) and NPs of anatase (B-A) with edge dislocations (Figure 30a–f) were

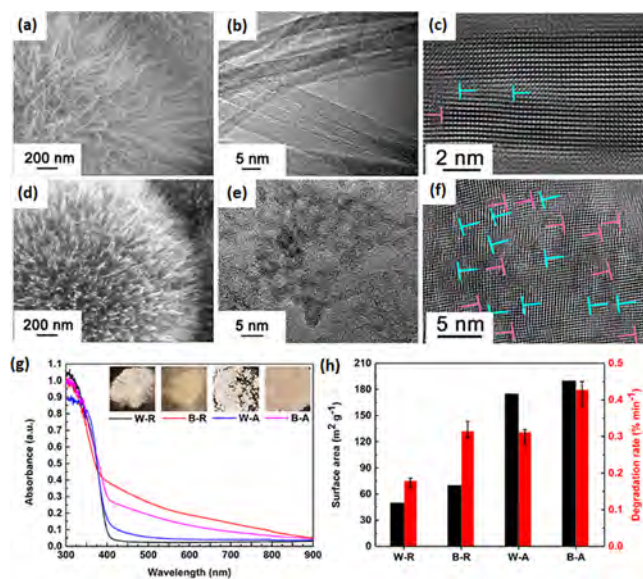


Figure 30. Edge dislocations formed via imperfect particle coalignment during growth.³⁵ (a,d) SEM and (b,c,e,f) HRTEM images of B-R (a–c) and B-A (e–f), respectively. (g) UV–vis spectra of W-R, B-R, W-A, and B-A, respectively. The insets show the optical images of W-R, B-R, W-A, and B-A powders. (h) Photo-degradation rate and surface area of W-R, B-R, W-A, and B-A. “T” represents edge dislocation. W-R, white rutile; B-R, brown rutile; W-A, white anatase; B-A, brown anatase. Adapted with permission from ref 35. Copyright 2019 Wiley-VCH.

obtained with visible solar absorption (400–900 nm) broadened significantly in comparison to rutile wires and anatase NPs without defects (Figure 30g).³⁵ The broadened UV–vis absorption improved the photocatalytic efficiency by up to 1.8 times (Figure 30h).

5. NP INTERACTIONS AND ENERGETICS OF PARTICLE ASSEMBLY AND OA PROCESSES

5.1. Interparticle Potential and Evolution of Energetics

Self-assembly of NPs into ordered superstructures requires precise control over NP interactions in solution. In the past two decades, a broad range of assembly routes, either spontaneous or guided, have been developed by modifying surface ligands^{91,179–181} or applying an external potential, such as a magnetic¹⁸² or electric^{183,184} field. The spontaneous assembly, for example, by slow solvent evaporation¹⁸⁵ or destabilization of a NP dispersion without external forces,^{186,187} is a main strategy for the assembly of colloidal NPs into superlattices, during which the system reaches thermodynamic equilibrium.¹⁶⁵

As a first-order approximation (i.e., assuming negligible multibody interactions), the forces driving self-assembly can be understood as collective effects from various competing pairwise forces/torques (i.e., vdW, electrostatics, hydration, etc.) that are explained in section 2. Any physicochemical parameter changes in either the particles and of the surrounding medium (e.g., ligand adsorption, structural modification, and pH/solution chemistry) drive the alteration of fundamental properties (e.g., surface charges, ionic strength, and dielectric properties), leading to noticeable changes in these forces/torques. Depending on the sensitivity of the fundamental properties to physicochemical parameters, the balance among the forces/torques is altered, resulting in energetics that can drive self-assembly. Interestingly, this force/torque balance dictates particle dynamics (i.e., translational and rotational motions of particles) so the energetics of self-assembly become coupled to kinetics. Due to perpetual random Brownian forces/torques that are appreciable for nanometer-sized particles, the net force/torque is nonzero, giving rise to a “quasi-equilibrium” state of the assembled structures. This is especially prevalent for nanocrystals (typically nonspherical) that are significantly influenced by both forces and torques, where the forces and torques are often coupled.

Tracking individual NP movements using in situ LP-TEM to estimate NP interaction energies¹⁸⁸ (Figure 31a,b) is of great importance, but very challenging. For many systems, LP-TEM is complementary to ensemble studies by X-ray scattering.^{172,189} However, quantifying individual NP interaction forces and mapping the energetics and stability of the dynamic assembly can be uniquely achieved by tracing individual NP trajectories observed in LP-TEM. For example, with an advanced image analysis method, NP trajectories were traced with high precision from a stack of relatively noisy images from in situ TEM experiments on Pt–Fe NPs.¹⁸⁸ This study illustrated that long-range anisotropic forces drive the formation of chains, which then clump and fold to maximize close range vdW interactions.

Collective motion and NP interactions can also be captured by direct imaging with the assistance of computer simulation. For example, CTA⁺-capped gold NPs can be assembled into two modes by tuning the concentration of cysteamine molecules (linkers).¹⁹⁰ At low cysteamine concentration (150 μ M), NRs attach end-to-end, whereas at high concentration (500 μ M), the NRs attach side-to-side (Figure 31c).

By combining particle tracking with Monte Carlo simulations, a recent study uncovered the crystallization process of triangular prisms from dispersed prisms to ordered superlattices. The prisms formed columns within which the prisms were misaligned and exhibited high orientational randomness. Crystallization proceeded by side-to-side columnar attachment

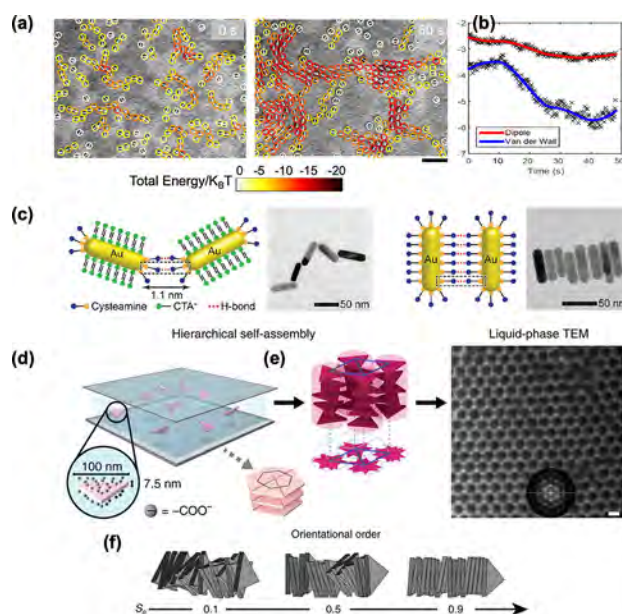


Figure 31. Tracking movement of NPs and estimating their interactions.¹⁸⁸ (a) Energy and stability of self-assembly. Colored circles indicate locations of Pt–Fe NPs overlaid on the original images. White arrows indicate dipole orientations. The color corresponds to the total energy of an individual NP computed from the dipole and vdW interaction with nearby particles. Scale bar: 20 nm. (b) The change in average particle energy contributions over time. Adapted with permission from ref 188. Copyright 2017 American Chemical Society. (c) Gold NP interactions and assembly.¹⁹⁰ Adapted with permission from ref 190. Copyright 2017 American Chemical Society. (d–f) Transition of gold nanoprisms into a superlattice by controlling NP interactions without affecting their motions. Combining particle tracking with Monte Carlo simulations showed the positional ordering of the superlattice emerges from orientational disorder.¹⁹¹ Scale bar in (e): 100 nm. Adapted with permission from ref 191. Copyright 2019 Springer Nature.

to form the final structure of hexagonally packed columns with touching edges¹⁹¹ (Figure 31d–f).

These and other studies show that, while much interest has been focused on the self-assembly of anisotropic NPs, these are often complex systems because small differences in NP shape, ligand length, and coverage, and solvent conditions can lead to markedly different self-assembled superstructures due to subtle changes in the free energy of ligand interactions.¹⁹²

As discussed above, tracking quasi-2D motions of NPs based on LP-TEM can provide an attractive pathway to understanding interparticle forces. However, correlating ensembles of particle configurations (i.e., radial distribution functions) from LP-TEM to the interaction potential is strictly valid at equilibrium. Here, the inherent nature of LP-TEM mitigates this issue. The motion of NPs is shown to become significantly slow due to interfacial solution structure in the proximity of a membrane, where the majority of particle motion takes place.^{193,194} This results in slow diffusion of particles in comparison to that expected in the bulk (e.g., using the Stokes–Einstein equation), implying that the interfacial solution structure induces a large “effective” viscosity.^{123,194} In fact, this characteristic renders assembly kinetics diffusion limited. For example, the study by Liu et al.¹²³ for ZnO OA in LP-TEM showed that the diffusivity of ZnO NPs is ~ 5 – 6 orders of magnitude smaller than that estimated from the Stokes–Einstein equation, allowing reliable extraction of the interaction potential from particle configurations based on LP-

TEM. Similar behavior^{95,104,195–197} has been observed in many LP-TEM based studies for various NPs.

5.2. Individual NP Structural Modifications from NP Interactions

During assembly, NPs interact with each other to form superlattices.¹⁶⁵ Such NP assemblies may actively respond to external stimuli, such as electric biasing,¹⁹⁸ magnetic¹⁹⁹ or mechanical²⁰⁰ forces, photon activation,^{201,202} etc., and they may also undergo self-healing processes.^{203,204} Individual NPs are often considered to act as “artificial atoms” and the properties of the NPs can be preserved during their interaction and assembly.²⁰⁵ The structural modifications of individual NPs during the assembly process are rarely discussed. However, some recent studies suggest that individual NPs may severely deform while interacting with other NPs^{206,207} or solvent molecules²⁰⁷ or during changes in environment.²⁰⁸

The behavior of individual nanocrystals during assembly may profoundly impact the structural perfection of the superlattices. However, details of individual nanocrystal transformations during assembly are largely unknown due to the lack of direct observation with high spatial resolution. Recent advances in LP-TEM²⁰⁹ have enabled tracking dynamic deformability of individual nanocrystals during superlattice phase transitions driven by ligand displacement.²⁰⁷ For instance, the as-synthesized PbSe nanocrystals with oleate ligands form a hexagonal superlattice on surfaces upon solvent evaporation. By introducing a solution of 1,2-ethylenediamine (EDA) in ethylene glycol (EG), the oleate ligands are removed and PbSe nanocrystals undergo OA. Subsequently, the superlattice also transforms from hexagonal to square. Through real-time high-resolution imaging with LP-TEM, the shape changes of individual nanocrystals were captured and the degree of individual PbSe NP deformation during superlattice transformations was found to be different when a different ligand-stripping solution was used (Figure 32).³⁷ The superlattice phase transition in pure EG shown reduced the deformability of individual nanocrystals and the transformation from an unconnected hexagonal lattice to a connected square lattice occurred with fewer defects. However, when an EDA containing solution (100 nL of a 15 mM solution of EDA in EG) was used to remove the oleate ligands on PbSe nanocrystals in a hexagonal lattice, the individual PbSe nanocrystals experienced drastic directional shape deformation when the spacing between nanocrystals reached 2–4 nm. A reversible elongation (up to 40%) was achieved. The deformation could be completely recovered when two nanocrystals moved apart, or it could be retained when they attached. This large deformation of PbSe nanocrystals during superlattice transition is responsible for structural defects formed in the epitaxially fused nanocrystal superlattice. The observed large deformability of PbSe semiconductor nanocrystals may arise from the intrinsic nanoscale property that the surface atoms of a nanocrystal are highly mobile during reconstruction.^{210,211} MD results showed that the dipole–dipole interactions may lead to the observed reversible elongation. Therefore, controlling nanocrystal deformation during ligand removal or ligand exchange may improve performance in many applications of semiconductor nanocrystals, such as photoelectric devices, plasmonics, and bioimaging.

5.3. Coalescence and Facet-Dependent Surface Energy of Superlattices

As with NP growth, where coalescence and shape are both driven by minimization of surface energy, self-assembled NP

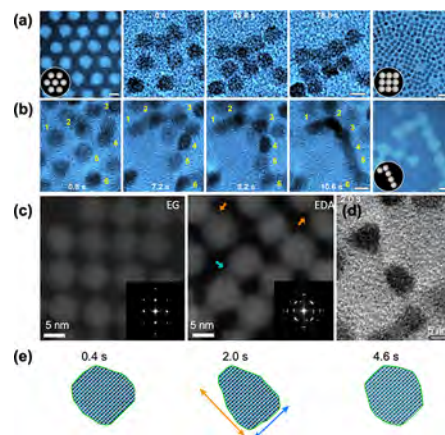


Figure 32. Deformation of individual PbSe NPs during assembly and superlattice transformation due to ligand displacement.³⁷ (a) The initial self-assembled hexagonal lattices of PbSe NPs capped with oleate ligands, sequential images (0–78.8 s) from in situ LP-TEM experiments showing the phase transition from hexagonal to epitaxially fused square superlattice after ligands were displaced, and a TEM image of the square lattice with a larger field of view. Reduced deformation of PbSe NPs during the superlattice transformation as ethylene glycol EG was used to strip the oleate ligands. Scale bars are 5 nm. (b) Sequential in situ TEM images showing the oriented attachment of six PbSe nanocrystals to form a 1D nanocrystal chain. An EDA-containing solution was used to strip oleate ligands. Scale bars are 5 nm. (c) High resolution TEM images showing the square lattice without obvious defects corresponding to EG stripping ligands (left), and the superlattice with defects in both crystalline orientation and connectivity corresponding to EDA stripping ligands (right). (d) Reversible directional shape deformation with EDA stripping ligands. (e) Schematics showing reversible deformation up to 40% along the long axis (highlighted in orange color). Adapted with permission from ref 37. Copyright 2019 The Authors, some rights reserved, exclusive licensee American Association for the Advancement of Science.

superlattices also exhibit coalescence and a shape formation process through a global minimization of surface energy. LP-TEM imaging of the dynamic formation process of NP assemblies allows for measurement of surface energies of the assemblies using capillary wave theory (CWT). CWT describes the shape evolution of a colloidal assembly and has been predominantly used for equilibrated interfaces (e.g., surface of the assembled structure and the suspension, liquid–liquid interface, liquid–solid interface) in micrometer-sized colloid²¹² and atomic²¹³ systems. When applying CWT to colloidal systems, one can regard the assembled structure as one phase, and the solution containing unassembled colloids as the other phase. In equilibrium, the surface between the above two phases is determined by a balance between the flattening effect of surface energy and statistical fluctuations of interface locations induced by thermal motion. Thermally induced capillary waves with different wavelengths superimpose onto rough interfacial profiles, where equilibrium roughness is a trade-off between the surface energy and thermal fluctuations.

By imaging the evolution of the NP assembly shapes, LP-TEM studies have made major contributions in the application of CWT analysis to NP assemblies. In the first demonstration using gold nanoarrows,⁹⁶ CWT theory revealed free energy minimization by reduction of surface area as the driving force for coalescence of small clusters of assembled gold nanoarrows into large clusters, which is a process similar to that occurring in atom systems (Figure 33a). Quantitatively, the experimentally

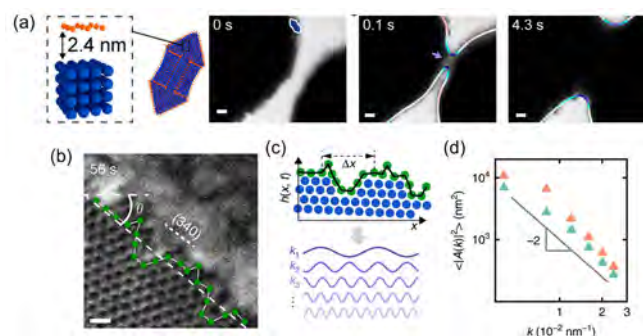


Figure 33. Coalescence and facet-dependent surface energy of superlattices. (a) Coalescence of clusters assembled from gold nanoarrows. Time-lapsed LP-TEM images showing the coalescence of two large clusters.⁹⁶ The boundaries of the clusters involved in coalescence are colored to surface curvature. Blue to white to pink indicates negative to positive surface curvature. Adapted with permission from ref 96. Copyright 2020 American Chemical Society. (b–d) The facet dependent surface energy of NP superlattices. (b) LP-TEM and the forefront surface profiles of a growing NP superlattice. (c) (top) The calculated total pairwise interactions for different gold nanoarrow pairs. (c) (bottom) Illustration of capillary waves forming into the final surface profiles. (d) Fourier components of the surface profiles fitting with CWT.²¹⁴ (b–d) Adapted with permission from ref 214. Copyright 2020 Springer Nature Open Access. Scale bars: 100 nm (a), 200 nm (b).

observed fluctuating surface profile of the small clusters can be first converted to a height function, which is then decomposed into a series of sinusoidal waves of wave vector κ (Figure 33c). The square of the time-averaged Fourier coefficient $\langle |A(\kappa)|^2 \rangle$ is well fit with $\kappa^{-2.2}$, consistent with the prediction of CWT ($\langle |A(\kappa)|^2 \rangle \sim \kappa^{-2}$, Figure 33d). Using CWT, the surface energy is calculated to be $(1.26 \pm 0.02) \times 10^{-13} \text{ J m}^{-1}$ for this system, corresponding to a surface energy gain of $3.2 k_B T$ based on the initial neck width d_{neck} (104 nm). In other words, during the collision of the two small clusters, the initial neck formation through the interaction of the NP surfaces is sufficient to cause an energy gain for the coalescence to continuously occur until the two small clusters completely merge into a large cluster. Here the surface energy term has a unit of energy/length because the analysis is performed on 2D-projected TEM images. In principle, this analysis can also be applied to 3D surfaces. This work shows that CWT applies to the NP assembly and gives a quantitative measure of the surface-energy change that drives assembly.

When CWT is applied to the surface profiles of a growing NP superlattice, it measures the facet-dependent interfacial stiffness (the sum of surface energy and its second derivative). In the example of a crystal formed from gold triangular nanoprisms (Figure 33b–d),²¹⁴ the exposed facets of a growing superlattice change from a high index {340} facet to a low index {210} facet, converging to a thermodynamically favored state of lower surface energy. The shift from high to low index facets is also consistent with the notion in atomic crystals that facets of lower Miller indices tend to have lower surface energies and to be exposed as crystal surfaces. The corresponding interfacial stiffnesses of these two facets were determined based on CWT. Specifically, fitting of $1/L \langle |A(\kappa)|^2 \rangle$ as a function of κ^2 , gives the interfacial stiffness $\gamma/k_B T$ as the slope. On one hand, the interfacial stiffness values of both the first and second stages are on the order of $10^{-14} \text{ J m}^{-1}$, consistent with interface stiffness scaling as $\sim k_B T/l_c$, where l_c is the size of the building block. On

the other hand, the interfacial stiffness increases from $(1.23 \pm 0.09) \times 10^{-14} \text{ J m}^{-1}$ to $(1.63 \pm 0.08) \times 10^{-14} \text{ J m}^{-1}$ by 32%, when the exposed facets change from {340} to {210}.

Earlier work has shown, for a given crystal interface within a suspension, the surface orientation with higher interfacial stiffness corresponds to that of lower surface energy.²¹⁵ This shift from a high- to a low-index facet at the growth front of the supracrystal thus effectively lowers the surface energy for an equilibrium crystal shape, matching the Wulff construction, a prominent principle for predicting the thermodynamically stable shape of a crystal by considering the collective effects of the surface energies of different facets.²¹⁶ Extensions of the Wulff construction to Winterbottom and Summertop constructions further predict the crystal shapes when crystal growth is confined by substrates. All the construction rules based on thermodynamic stability require precise surface energy values of different supracrystalline facets as inputs. The application of CWT is thus a promising method for providing the needed inputs to achieve shape control of NP superlattices.

These observations of atom-mimicking self-organization behaviors in NP systems inspire further study of the general applicability of this analogy and suggest that the synthesis toolkits for atomic crystals (e.g., seeded growth to break symmetry and single crystal growth by OA) can also be used to encode structure and dynamics during nanoscale self-organization in NP systems.

6. SUMMARY AND OUTLOOK

6.1. Recent Achievements and Ongoing Advances

6.1.1. Recent Achievements. Particle assembly is a common pathway for crystal growth and formation of material structures in both synthetic and natural systems. This process is controlled via a cooperative interplay between short-range (within 1 or 2 nm) and long-range forces, which include vdW attraction (short and long), hydrodynamic drag (short and long), Brownian forces (short and long), electrostatic repulsion (short and long), hydration repulsion (short), and steric hindrance (short) from ligands attached on the particle surface. In particle assembly processes, colloidal particles are typically coated with organic ligands, polymers, or biomolecules (e.g., peptoids or DNA), which prevent particle aggregation and help determine the structural outcome (e.g., superlattices) through the interactions between ligands. For example, structures of crystal superlattices and supracrystals can be controlled by biomolecular or biomimetic ligands (DNA or peptoids, Figure 34a). NP shape can also regulate interparticle interactions through volume effects (atoms inside the NP) or surface contours, where ligand effects dominate.⁹⁷ OA is a special type of particle aggregation, during which particles are crystallographically coaligned before coalescence or attach with a slight misalignment and relax via atomistic processes into coalignment. During OA, ligands, which prevent particle aggregation, are typically not present. Therefore, the interfacial solution structures (between the particle surface and solution) and the resulting collective properties (e.g., dielectric properties of the interfacial solution layer) are mainly responsible for orientation-dependent adhesion forces and are strongly correlated to the ion concentration and specificity (e.g., Na^+ vs K^+). By controlling the OA process, we can not only direct nano/microstructures of materials, such as 1D nanowires,⁶ 2D nanosheets,¹⁴⁷ and 3D branched or hierarchical structures,⁶ but also atomic lattice structures, such as 5-fold twins³⁴ and defects (Figure 34b).³⁵

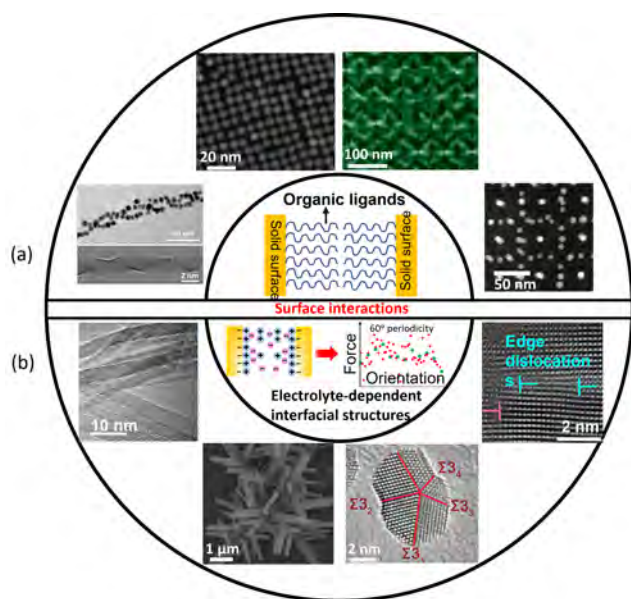


Figure 34. Material structures formed through particle–surface interactions during particle assembly (a) and OA (b). (a) Reproduced with permission from ref 93. Copyright 2008 American Chemical Society. Reproduced with permission from ref 94. Open access. Copyright 2014 American Chemical Society. Reproduced with permission from ref 37. Copyright 2019 exclusive licensee American Association for the Advancement of Science. Reproduced with permission from ref 38. Open Access. Copyright 2016 American Chemical Society. Adapted with permission from ref 7. Copyright 2022. Nature/Springer/Palgrave. (b) Adapted with permission from ref 35. Copyright 2019 Wiley-VCH. Reproduced with permission from ref 6. Copyright 2013 American Chemical Society. Adapted with permission from ref 34. Copyright 2019 American Association for the Advancement of Science. Adapted with permission from ref 35. Copyright 2019 Wiley-VCH.

Mechanistic studies of particle assembly and OA have recently come to the forefront with advances using cryo-TEM,^{18,19,24,30,217} liquid phase TEM,^{34,218–221} and AFM-based techniques. The prevalent application of in situ TEM to inorganic NP growth and assembly at equilibrium have established a conceptual and technical framework readily extendable to other nanoblocks, such as viral particles and proteins, and systems undergoing dissipative dynamics. One can also decode the behavior, all the way from single-particle trajectory analysis and pairwise interaction mapping to collective pattern formation. Note that in situ TEM has functional modules, such as heating, liquid flow, and electric biasing, to allow incorporation of external energy inputs for nonequilibrium growth conditions²²² to achieve exotic, metastable shapes or crystallinity of NPs and dissipative assembly. AFM-DFS studies that utilize custom-made single crystal tips, combined with MD simulations, have measured and predicted crystal–crystal interactions vs orientation.^{71,126,135,221,223} By developing atomic-scale, AFM-based 3D FFM,^{224–231} researchers now obtain experimental data on the structure of solutions between the tip and the crystal surface that can be compared to simulations to complete the connection between structure, forces, and motion.¹³⁰ These recent studies provide deep mechanistic insights but have brought into focus clear gaps in understanding.

6.1.2. Ongoing Advances. Thanks to the pioneering work on model development in computer science and the successful

application of image processing in biomedical and optical microscopy, machine learning (ML), especially via convolutional neural networks (NN), has become a powerful tool in the processing and statistical analysis of data.^{98,101} The direct information extraction from 2D TEM and 3D FFM images can be achieved by different designs of NN architectures, covering tasks of increasing complexity from single-image classification and regression to trajectory classification. Tremendous opportunities will emerge when all the analysis is extended to 3D. In 3D electron tomography with TEM and STEM-EDX, NN can help the reconstruction process by denoising, interpolating, and extrapolating the experimental sinogram, postfixing, or segmenting the reconstruction given by simple algorithms, and implementing the actual sinogram-to-image domain transformation. Integration of these methods with the tomography capability of LP-TEM movies will open a new avenue for understanding the growth and assembly dynamics of NPs in 3D.

6.2. Remaining Challenges and Future Directions

With the advancements of in situ TEM and AFM techniques and ML-assisted analysis of complex data, researchers have revealed molecular details (e.g., charge states at NP/fluid interfaces, inhomogeneity of surface charges, and dielectric/magnetic properties of NPs) that directly influence long- and short-range particle forces (e.g., electrostatic, vdW, hydration, and dipole–dipole forces). However, molecular details, particle forces, and local/ensemble responses and microstructure over various spatial and temporal scales are intertwined via the “structure–property–force” relationship that is not fully understood, especially in the proximity of NPs. In addition to the molecular details, mesoscopic characteristics can add an additional dimension to this complicated relationship. While previous studies have defined molecular details of interfacial solution structure, often revealing significant heterogeneity and complexity,^{130,232,233} the current state of knowledge (e.g., the strength of hydration forces, the structure of the EDL, and resultant electrostatic forces) does not provide a convincing and consistent physical rationale for particle contact (i.e., expulsion of the intervening solution layer).

Integrated with experimental results, simulations can provide insights at molecular, micro, and mesoscales. However, it is a long-standing challenge for current theoretical and simulation frameworks, which possesses inherent limitations at various spatial and temporal scales. Classical MD simulations with empirical force fields can be useful, but the calculated interaction energy and predicted molecular structures are dependent on specific force fields. The obtained interaction energy and force in DFT-based MD simulation are more accurate, but the computational cost of these methods makes them impractical for long simulations of dynamical processes such as NP assembly. Furthermore, many-body interactions are often missing in classical MD and can be poorly represented in DFT-based ab initio MD.

Data science is a recently developed interdisciplinary field that deals with large and complex data sets and integrates theory, experimentation, and simulation to extract knowledge and insights from data in various forms. ML trained NN potentials provide an efficient and accurate approach. However, a ML scheme needs to be firmly established on rigorous fundamental chemical physics and related principles. Research will need to connect various theoretical and simulation frameworks that possess inherent limitations at respective spatial and temporal scales. Combining a ML scheme for constructing “effective”

particle forces/torques to this approach can further accelerate particle-based Langevin simulations at the continuum scale. For example, one needs to connect *ab initio* MD (or DFT calculations), MD, and Langevin dynamic simulations to resolve the inherent coupling, ranging from atomistic to continuum scales. In this sense, a “coarse-graining” simulation scheme that is based on mathematical and physical rigor can be realized. A ML-based approach can be further utilized to obtain relatively unbiased force-field parameters at the atomistic or molecular scale.

A promising pathway, among others, would be to reformulate relevant continuum theories (e.g., Poisson–Boltzmann and Lifshitz theories) to obtain particle forces by accounting for the unique fundamental physicochemical properties of interfacial solution layers and key molecular descriptors (e.g., ion–surface PMF) that are identified and obtained from relevant simulations (e.g., *ab initio* MD and MD) or experiments. These forces can then serve as relevant constituents of Langevin dynamic simulations to cover collective scales with manageable computational burden. As an example, combined with experiments and molecular simulations, the interfacial solution structure (which depends on interfacial chemistry) and the dielectric properties of NPs were coupled to macroscopic Lifshitz theories^{60,234} via a simple density-dielectric mapping, leading to a qualitatively different vdW force than predicted with a simple DLVO model. Further development of such approaches would ensure self-consistency over various spatial and temporal scales. This approach will also shed light on the important coupling between electrostatics and electrodynamics, which leads to such effects as that of electrolyte concentration and types on the vdW interaction. This effect has not been rigorously studied since the 1980s.^{53,61,235}

Particle assembly and OA have been mainly studied without an external field. As pointed out, the inherent coupling between molecular-scale structural details, particle forces/torques, and local response dynamics of NPs would be a key aspect for tailoring the process. An external field such as flow or electromagnetic field will impose an additional force on the particles and, as a result, significantly perturb an interplay between the forces at different spatial and temporal scales involved in particle assembly and OA, in comparison to that under (near) equilibrium. Thus, the nonequilibrium nature due to such external field has potential to explore new “kinetically driven” metastable material structures or OA behavior. In this case, forces on NPs under equilibrium (i.e., electrostatic, vdW, and Brownian forces) will be coupled to nonequilibrium forces (i.e., shear and magnetic forces) depending on fundamental properties of the NPs and the suspending medium. The anisotropic nature of NPs provides an additional feature through which to achieve new material structures via an interplay between intrinsic and external torques. Under certain circumstances, the effect of the external field will not be additive when the external field also changes the intrinsic equilibrium forces by influencing molecular details (e.g., ion environment). Therefore, predictive modeling based on a fundamental understanding of phenomena over a wide range of such scales (via a combination of multidisciplinary theories and simulations) is of increasing importance because any empirical approach is severely limited under such complicated nonequilibrium conditions.

Looking ahead, multidisciplinary efforts, including state-of-the-art *in situ* measurements of particle dynamics and near-surface solution structures, combining ML schemes with

simulations, and integrating multiscale theories and simulations, is needed to deeply understand the complexity and heterogeneity of molecular details of interfacial solution structure and the resulting interparticle forces/particle motions, and emergent structures, leading to rigorous coupling between phenomena over different scales. This multidisciplinary approach will provide a complete, convincing, and consistent physical rationale and improved fundamental understanding of particle attachment pathways.

AUTHOR INFORMATION

Corresponding Author

Dongsheng Li – *Physical and Computational Sciences Directorate, Pacific Northwest National Laboratory, Richland, Washington 99352, United States*; orcid.org/0000-0002-1030-146X; Email: Dongsheng.li2@pnnl.gov

Authors

Qian Chen – *Department of Materials Science and Engineering, University of Illinois, Urbana, Illinois 61801, United States*; orcid.org/0000-0002-1968-441X

Jaehun Chun – *Physical and Computational Sciences Directorate, Pacific Northwest National Laboratory, Richland, Washington 99352, United States; Levich Institute and Department of Chemical Engineering, CUNY City College of New York, New York, New York 10031, United States*; orcid.org/0000-0002-2291-6496

Kristen Fichthorn – *Department of Chemical Engineering, The Pennsylvania State University, University Park, Pennsylvania 16802, United States*; orcid.org/0000-0002-4256-714X

James De Yoreo – *Physical and Computational Sciences Directorate, Pacific Northwest National Laboratory, Richland, Washington 99352, United States; Department of Materials Science and Engineering, University of Washington, Seattle, Washington 98195, United States*; orcid.org/0000-0002-9194-6699

Haimei Zheng – *Materials Sciences Division, Lawrence Berkeley National Laboratory, Berkeley, California 94720, United States; Department of Materials Science and Engineering, University of California, Berkeley, California 94720, United States*; orcid.org/0000-0003-3813-4170

Complete contact information is available at:
<https://pubs.acs.org/10.1021/acs.chemrev.2c00700>

Author Contributions

Dongsheng Li – writing-original draft of sections 1, 2.1–2.4, 3.1, 4.1, 4.2, 4.4, 6.1, 6.2; review and editing; supervision. Qian Chen – writing-original draft of chapters 2.4, 2.5, 5.3, 6.1; review & editing. Jaehun Chun – writing-original draft of chapters 2.1, 2.2, 2.4, 3.1, 3.2, 5.1, 6.2; review & editing. Kristen Fichthorn – writing-original draft of chapters 2.4, 2.5, 3.1, 3.2, 4.1; review & editing. James De Yoreo – writing-original draft of chapters 3.2, 3.3; review & editing. Haimei Zheng – writing-original draft of chapters 4.3, 5.1, 5.2. review & editing.

Notes

The authors declare no competing financial interest.

Biographies

Dongsheng Li received her Ph.D. degree in Materials from the Pennsylvania State University in 2005, where she worked on metal nanomaterials synthesis and optical property characterization. Following postdoctoral work at the Ohio State University and University of

California, Riverside, she became a scientist at Lawrence Berkeley National Laboratory in 2011, where she studied crystal growth pathways via oriented attachments using in situ transmission electron microscopy. She joined the Pacific Northwest National Laboratory as a materials scientist in 2013. Her research focuses on crystal nucleation and growth, materials synthesis and processing, and structure–function relationships. Specifically, using in situ transmission electron microscopy and atomic force microscopy, her research primarily focuses on (1) crystal structure formation via oriented attachments, (2) solid-state phase transformation among polymorphous, and (3) structure–function relationships of catalysts materials.

Qian Chen is an Associate Professor and Racheff Faculty Scholar in Materials Science and Engineering at the University of Illinois at Urbana–Champaign (UIUC). She received a B.S. in Chemistry from Peking University. She got her Ph.D. degree in 2012 from the Department of Materials Science and Engineering at UIUC under the guidance of Steve Granick, and did her postdoctoral research with A. Paul Alivisatos as a Miller Fellow at University of California, Berkeley. She started her faculty position at UIUC in 2015. Her research focuses on the broad scheme of imaging, understanding, and engineering the structure, form, and function of soft, biological, and energy matter at the nanoscale using electron microscopy, including systems such as nanoparticle and colloidal self-assembly, protein transformation and aggregation, advanced battery devices, and energy-efficient water filtration.

Jaehun Chun is a Research Scientist working at the Pacific Northwest National Laboratory and an Affiliate Professor at Lehigh Institute and Department of Chemical Engineering, CUNY City College of New York. He received his Ph.D. from the Department of Chemical and Biomolecular Engineering at Cornell in 2003 under the guidance of Donald L. Koch, followed by postdoctoral research with Dudley A. Saville in the Department of Chemical and Biological Engineering at Princeton. His research interest is mainly on energetics and dynamics of various microstructured fluids (e.g., micelles, colloids, NPs, biomacromolecules) over the wide range of length scales, especially focusing on the development of theoretical/simulation frameworks for correlating chemical physics at different length scales, combined with state-of-the-art experiments such as in situ transmission electron microscopy and atomic force microscopy. Of particular interest are self-assemblies of NPs and macromolecules, underlying electrostatic and electromagnetic forces, and physicochemical hydrodynamics/rheology of colloidal dispersions.

Kristen Fichthorn is the Merrell Fenske Professor of Chemical Engineering and a Professor of Physics at the Pennsylvania State University. She received a B.S. in Chemical Engineering from the University of Pennsylvania and a Ph.D. in Chemical Engineering from the University of Michigan and spent one year as an IBM Postdoctoral Fellow at the University of California at Santa Barbara before joining Penn State. Professor Fichthorn's research is primarily in multiscale materials simulation, in which she develops and applies theoretical techniques ranging from quantum DFT to MD, Monte Carlo methods, and continuum theories to a diverse array of fundamental problems involving fluid–solid interfaces. Applications lie in nanoscale materials, thin-film and crystal growth, colloidal assembly, and wetting.

James De Yoreo is a Battelle Fellow at Pacific Northwest National Laboratory (PNNL) and an Affiliate Professor of Materials Science and Engineering at the University of Washington. He received his Ph.D. in Physics from Cornell University in 1985. Following postdoctoral work at the University of Maine and Princeton University, he became a member of the technical staff at Lawrence Livermore National Laboratory in 1989, where he held numerous positions. He joined

Lawrence Berkeley National Laboratory in 2007, where he served as Interim Director of the Molecular Foundry before moving to PNNL in 2012. De Yoreo's research focuses on molecular interactions, self-assembly, and crystallization in inorganic, biomolecular, and biomineral systems via in situ scanned probe and electron microscopy.

Haimei Zheng is a senior staff scientist in the Materials Sciences Division at Lawrence Berkeley National Laboratory (LBNL) and an adjunct professor in the Department of Materials Science and Engineering at University of California, Berkeley. She received her Ph.D. degree from the University of Maryland, College Park. She completed her Ph.D. research in Materials Science and Engineering at the University of California, Berkeley. Thereafter, she became a postdoc at the National Center for Electron Microscopy of LBNL and in the Chemistry Department of University of California, Berkeley. She started her independent research in the Materials Sciences Division at LBNL in 2010 as a Staff Scientist and was promoted to Senior Scientist in 2018. Her research interests are centered on understanding how atomic level heterogeneity and fluctuations control the physical and chemical processes of materials, with the focus on imaging, understanding, and controlling of nucleation, growth, and structural transformations of nanoscale materials, dynamic phenomena at solid–liquid interfaces, and energy materials by developing advanced in situ transmission electron microscopy methods.

ACKNOWLEDGMENTS

The work by D.L., J.C., and J.D. was supported by the U.S. Department of Energy (DOE), Office of Basic Energy Sciences (BES), Division of Materials Science and Engineering (MSE), Synthesis and Processing Science Program FWP 67554. The work by Q.C. was supported by the Air Force Office of Scientific Research through award no. FA9550-20-1-0257. The work by K.F. was supported by the DOE BES MSE, award no. DE FG02-07ER46414. The work by H.Z. was supported by the DOE BES MSE under award no. DE-AC02-05-CH11231 within the in situ TEM program (KC22ZH).

ABBREVIATIONS

OA = oriented attachment
AFM = atomic force microscopy
AM-AFM = amplitude modulated AFM
CCM = complementary contact model
cDFT = classical DFT
CG = coarse-grained
CWT = capillary wave theory
DFS = dynamic force spectroscopy
DFT = density functional theory
DLVO = Derjaguin–Landau–Verwey–Overbeek
EDL = electrical double layer
F = force
FFM = fast force mapping
GB = grain boundary
GC = Gouy–Chapman
HRTEM = high resolution transmission electron microscopy
Hy = surface hydration repulsion
IC = ion correlation
IC = ion correlation
LP-TEM = liquid phase TEM
MD = molecular dynamics
ML = machine learning
NN = neural networks
NP = nanoparticle
PB = Poisson–Boltzmann

TEM = transmission electron microscopy
vdW = van der Waals
1D = one-dimensional
5-FT = 5-fold twin

REFERENCES

- (1) Wang, Y.; Wan, D.; Xie, S.; Xia, X.; Huang, C. Z.; Xia, Y. Synthesis of silver octahedra with controlled sizes and optical properties via seed-mediated growth. *ACS Nano* **2013**, *7*, 4586–4594.
- (2) Herman, I.; Yeo, J.; Hong, S.; Lee, D.; Nam, K. H.; Choi, J.-h.; Hong, W.-h.; Lee, D.; Grigoropoulos, C. P.; Ko, S. H. Hierarchical weeping willow nano-tree growth and effect of branching on dye-sensitized solar cell efficiency. *Nanotechnology* **2012**, *23*, 194005.
- (3) Nudelman, F.; Gotliv, B. A.; Addadi, L.; Weiner, S. Mollusk shell formation: Mapping the distribution of organic matrix components underlying a single aragonitic tablet in nacre. *J. Struct. Biol.* **2006**, *153*, 176–187.
- (4) Miszta, K.; de Graaf, J.; Bertoni, G.; Dorfs, D.; Brescia, R.; Marras, S.; Ceseracciu, L.; Cingolani, R.; van Roij, R.; Dijkstra, M.; Manna, L. Hierarchical self-assembly of suspended branched colloidal nanocrystals into superlattice structures. *Nat. Mater.* **2011**, *10*, 872–876.
- (5) Paik, T.; Diroll, B. T.; Kagan, C. R.; Murray, C. B. Binary and ternary superlattices self-assembled from colloidal nanodisks and nanorods. *J. Am. Chem. Soc.* **2015**, *137*, 6662–6669.
- (6) Sun, P.; Zhang, X.; Wang, C.; Wei, Y.; Wang, L.; Liu, Y. Rutile TiO₂ nanowire array infiltrated with anatase nanoparticles as photoanode for dye-sensitized solar cells: enhanced cell performance via the rutile-anatase heterojunction. *J. Mater. Chem. A* **2013**, *1*, 3309–3314.
- (7) Wang, S.; Lee, S.; Du, J. S.; Partridge, B. E.; Cheng, H. F.; Zhou, W.; Dravid, V. P.; Lee, B.; Glotzer, S. C.; Mirkin, C. A. The emergence of valency in colloidal crystals through electron equivalents. *Nat. Mater.* **2022**, *21*, 580–587.
- (8) Penn, R. L.; Banfield, J. F. Imperfect oriented attachment: Dislocation generation in defect-free nanocrystals. *Science* **1998**, *281*, 969–971.
- (9) Penn, R. L.; Banfield, J. F. Oriented attachment and growth, twinning, polytypism, and formation of metastable phases: Insights from nanocrystalline TiO₂. *Am. Mineral.* **1998**, *83*, 1077–1082.
- (10) Boneschanscher, M. P.; Evers, W. H.; Geuchies, J. J.; Altantzis, T.; Goris, B.; Rabouw, F. T.; van Rossum, S. A. P.; van der Zant, H. S. J.; Siebbeles, L. D. A.; Van Tendeloo, G.; et al. Long-range orientation and atomic attachment of nanocrystals in 2D honeycomb superlattices. *Science* **2014**, *344*, 1377–1380.
- (11) Cho, K. S.; Talapin, D. V.; Gaschler, W.; Murray, C. B. Designing PbSe nanowires and nanorings through oriented attachment of nanoparticles. *J. Am. Chem. Soc.* **2005**, *127*, 7140–7147.
- (12) Kuno, M. An overview of solution-based semiconductor nanowires: synthesis and optical studies. *Phys. Chem. Chem. Phys.* **2008**, *10*, 620–639.
- (13) Li, Z. G.; Sui, J. H.; Li, X. L.; Cai, W. Oriented attachment growth of quantum-sized CdS nanorods by direct thermolysis of single-source precursor. *Langmuir* **2011**, *27*, 2258–2264.
- (14) Liao, H. G.; Zheng, H. M. Liquid cell transmission electron microscopy study of platinum iron nanocrystal growth and shape evolution. *J. Am. Chem. Soc.* **2013**, *135*, 5038–5043.
- (15) Yuk, J. M.; Park, J.; Ercius, P.; Kim, K.; Hellebusch, D. J.; Crommie, M. F.; Lee, J. Y.; Zettl, A.; Alivisatos, A. P. High-resolution EM of colloidal nanocrystal growth using graphene liquid cells. *Science* **2012**, *336*, 61–64.
- (16) Lupulescu, A. I.; Rimer, J. D. In situ imaging of silicalite-1 surface growth reveals the mechanism of crystallization. *Science* **2014**, *344*, 729–732.
- (17) Davis, T. M.; Drews, T. O.; Ramanan, H.; He, C.; Dong, J. S.; Schnablegger, H.; Katsoulakis, M. A.; Kokkoli, E.; McCormick, A. V.; Penn, R. L.; Tsapatsis, M. Mechanistic principles of nanoparticle evolution to zeolite crystals. *Nat. Mater.* **2006**, *5*, 400–408.
- (18) Baumgartner, J.; Dey, A.; Bomans, P. H. H.; Le Coadou, C.; Fratzl, P.; Sommerdijk, N.; Faivre, D. Nucleation and growth of magnetite from solution. *Nat. Mater.* **2013**, *12*, 310–314.
- (19) Burrows, N. D.; Hale, C. R. H.; Penn, R. L. Effect of pH on the kinetics of crystal growth by oriented aggregation. *Cryst. Growth Des.* **2013**, *13*, 3396–3403.
- (20) Cölfen, H. Mesocrystals: Examples of non-classical crystallization. In *Handbook of Biomineralization: Biological Aspects and Structure Formation*; Bauerlein, E., Ed.; Wiley-VCH, Weinheim, 2008; pp 39–64.
- (21) Nielsen, M. H.; Li, D. S.; Zhang, H. Z.; Aloni, S.; Han, T. Y. J.; Frandsen, C.; Seto, J.; Banfield, J. F.; Cölfen, H.; De Yoreo, J. J. Investigating processes of nanocrystal formation and transformation via liquid cell TEM. *Microsc. microanal.* **2014**, *20*, 425–436.
- (22) Penn, R. L. Kinetics of oriented aggregation. *J. Phys. Chem. B* **2004**, *108* (34), 12707–12712.
- (23) Raju, M.; van Duin, A. C. T.; Fichthorn, K. A. Mechanisms of oriented attachment of TiO₂ nanocrystals in vacuum and humid environments: Reactive molecular dynamics. *Nano Lett.* **2014**, *14*, 1836–1842.
- (24) Yuwono, V. M.; Burrows, N. D.; Soltis, J. A.; Penn, R. L. Oriented aggregation: Formation and transformation of mesocrystal intermediates revealed. *J. Am. Chem. Soc.* **2010**, *132*, 2163–2165.
- (25) Zhang, H. Z.; De Yoreo, J. J.; Banfield, J. F. A unified description of attachment-based crystal growth. *ACS Nano* **2014**, *8*, 6526–6530.
- (26) Zhu, G.; Sushko, M. L.; Loring, J. S.; Legg, B. A.; Song, M.; Soltis, J. A.; Huang, X.; Rosso, K. M.; De Yoreo, J. J. Self-similar mesocrystals form via interface-driven nucleation and assembly. *Nature* **2021**, *590*, 416–422.
- (27) Bard, A. B.; Zhou, X. Z.; Xia, X. J.; Zhu, G. M.; Lim, M. B.; Kim, S. M.; Johnson, M. C.; Kollman, J. M.; Marcus, M. A.; Spurgeon, S. R.; et al. A mechanistic understanding of nonclassical crystal growth in hydrothermally synthesized sodium yttrium fluoride nanowires. *Chem. Mater.* **2020**, *32*, 2753–2763.
- (28) Bai, L.; Wang, N.; Li, Y. Controlled growth and self-assembly of multiscale organic semiconductor. *Adv. Mater.* **2022**, *34*, 2102811.
- (29) Chen, J. J.; Zhu, E. B.; Liu, J.; Zhang, S.; Lin, Z. Y.; Duan, X. F.; Heinz, H.; Huang, Y.; De Yoreo, J. J. Building two-dimensional materials one row at a time: Avoiding the nucleation barrier. *Science* **2018**, *362*, 1135.
- (30) Van Driessche, A. E. S.; Van Gerven, N.; Bomans, P. H. H.; Joosten, R. R. M.; Friedrich, H.; Gil-Carton, D.; Sommerdijk, N. A. J. M.; Sleutel, M. Molecular nucleation mechanisms and control strategies for crystal polymorph selection. *Nature* **2018**, *556*, 89.
- (31) Cho, K.-S.; Talapin, D. V.; Gaschler, W.; Murray, C. B. Designing PbSe nanowires and nanorings through oriented attachment of nanoparticles. *J. Am. Chem. Soc.* **2005**, *127*, 7140–7147.
- (32) Wang, Y.; Peng, X.; Abelson, A.; Xiao, P.; Qian, C.; Yu, L.; Ophus, C.; Ercius, P.; Wang, L.-W.; Law, M.; Zheng, H. Dynamic deformability of individual PbSe nanocrystals during superlattice phase transitions. *Sci. Adv.* **2019**, *5*, No. eaaw5623.
- (33) Wang, Y.; Peng, X.; Abelson, A.; Zhang, B.-K.; Qian, C.; Ercius, P.; Wang, L.-W.; Law, M.; Zheng, H. In situ TEM observation of neck formation during oriented attachment of PbSe nanocrystals. *Nano Res.* **2019**, *12*, 2549–2553.
- (34) Song, M.; Zhou, G.; Lu, N.; Lee, J.; Nakouzi, E.; Wang, H.; Li, D. Oriented attachment induces fivefold twins by forming and decomposing high-energy grain boundaries. *Science* **2020**, *367*, 40–45.
- (35) Ren, P.; Song, M.; Lee, J.; Zheng, J.; Lu, Z.; Engelhard, M.; Yang, X.; Li, X.; Kisailus, D.; Li, D. Edge dislocations induce improved photocatalytic efficiency of colored TiO₂. *Adv. Mater. Interfaces.* **2019**, *6*, 1901121.
- (36) Lee, J.; Nakouzi, E.; Song, M.; Wang, B.; Chun, J.; Li, D. Mechanistic Understanding of the Growth Kinetics and Dynamics of Nanoparticle Superlattices by Coupling Interparticle Forces from Real-Time Measurements. *ACS Nano* **2018**, *12*, 12778–12787.
- (37) Wang, Y.; Peng, X.; Abelson, A.; Xiao, P.; Qian, C.; Yu, L.; Ophus, C.; Ercius, P.; Wang, L.-W.; Law, M.; Zheng, H. Dynamic deformability

of individual PbSe nanocrystals during superlattice phase transitions. *Sci. Adv.* **2019**, 5, No. eaaw5623.

(38) Boles, M. A.; Engel, M.; Talapin, D. V. Self-Assembly of Colloidal Nanocrystals: From intricate structures to functional materials. *Chem. Rev.* **2016**, 116, 11220–11289.

(39) Li, D.; Nielsen, M. H.; Lee, J. R. I.; Frandsen, C.; Banfield, J. F.; De Yoreo, J. J. Direction-specific interactions control crystal growth by oriented attachment. *Science* **2012**, 336, 1014–1018.

(40) Liao, H.-G.; Cui, L.; Whitelam, S.; Zheng, H. Real-time imaging of Pt 3Fe nanorod growth in solution. *Science* **2012**, 336, 1011–14.

(41) Yuk, J. M.; Park, J.; Ercius, P.; Kim, K.; Hellebusch, D. J.; Crommie, M. F.; Lee, J. Y.; Zettl, A.; Alivisatos, A. P. High-resolution EM of colloidal nanocrystal growth using graphene liquid cells. *Science* **2012**, 336, 61.

(42) Huang, F.; Zhang, H. Z.; Banfield, J. F. Two-stage crystal-growth kinetics observed during hydrothermal coarsening of nanocrystalline ZnS. *Nano Lett.* **2003**, 3, 373–378.

(43) Gong, M.; Kirkeminde, A.; Ren, S. Symmetry-defying iron pyrite (FeS₂) nanocrystals through oriented attachment. *Sci. Rep.* **2013**, 3, 2092.

(44) Zhang, J.; Huang, F.; Lin, Z. Progress of nanocrystalline growth kinetics based on oriented attachment. *Nanoscale* **2010**, 2, 18.

(45) Yang, L.; Yang, H.; Yang, Z.; Cao, Y.; Ma, X.; Lu, Z.; Zheng, Z. Observation of rotated-oriented attachment during the growth of Ag₂S nanorods under mediation of protein. *J. Phys. Chem. B* **2008**, 112, 9795–9801.

(46) Zhu, G.; Zhang, S.; Xu, Z.; Ma, J.; Shen, X. Ultrathin ZnS single crystal nanowires: controlled synthesis and room-temperature ferromagnetism properties. *J. Am. Chem. Soc.* **2011**, 133, 15605–15612.

(47) Yasui, K.; Kato, K. Dipole-dipole interaction model for oriented attachment of BaTiO₃ nanocrystals: a route to mesocrystal formation. *J. Phys. Chem. C* **2012**, 116, 319–324.

(48) Ghezelbash, A.; Koo, B.; Korgel, B. A. Self-assembled stripe patterns of CdS nanorods. *Nano Lett.* **2006**, 6, 1832–1836.

(49) Zhang, H.; Banfield, J. F. Energy Calculations Predict Nanoparticle Attachment Orientations and Asymmetric Crystal Formation. *J. Phys. Chem. Lett.* **2012**, 3, 2882–2886.

(50) Ribeiro, C.; Lee, E. J. H.; Longo, E.; Leite, E. R. A kinetic model to describe nanocrystal growth by the oriented attachment mechanism. *ChemPhysChem* **2005**, 6, 690–696.

(51) Grochowski, P.; Trylska, J. Continuum molecular electrostatics, salt effects, and counterion binding—a review of the Poisson–Boltzmann theory and its modifications. *Biopolymers: Original Research on Biomolecules* **2008**, 89, 93–113.

(52) Tan, Q.; Zhao, G.; Qiu, Y.; Kan, Y.; Ni, Z.; Chen, Y. Experimental observation of the ion–ion correlation effects on charge inversion and strong adhesion between mica surfaces in aqueous electrolyte solutions. *Langmuir* **2014**, 30, 10845–10854.

(53) Ninham, J. M. u. B. *Dispersion Forces*; Academic Press: London, New York, San Francisco, 1976.

(54) Baimpos, T.; Shrestha, B. R.; Raman, S.; Valtiner, M. Effect of interfacial ion structuring on range and magnitude of electric double layer, hydration, and adhesive interactions between mica surfaces in 0.05–3 M Li⁺ and Cs⁺ electrolyte solutions. *Langmuir* **2014**, 30, 4322–4332.

(55) Butt, H.-J. Measuring electrostatic, van der Waals, and hydration forces in electrolyte solutions with an atomic force microscope. *Biophys. J.* **1991**, 60, 1438–1444.

(56) Kilpatrick, J. I.; Loh, S.-H.; Jarvis, S. P. Directly probing the effects of ions on hydration forces at interfaces. *J. Am. Chem. Soc.* **2013**, 135, 2628–2634.

(57) Parsegian, V.; Zemb, T. Hydration forces: Observations, explanations, expectations, questions. *Current opinion in colloid & interface science* **2011**, 16, 618–624.

(58) Baimpos, T.; Shrestha, B. R.; Raman, S.; Valtiner, M. Effect of interfacial ion structuring on range and magnitude of electric double layer, hydration, and adhesive interactions between mica surfaces in

0.05–3 M Li⁺ and Cs⁺ electrolyte solutions. *Langmuir* **2014**, 30, 4322–4332.

(59) Tan, Q.; Zhao, G.; Qiu, Y.; Kan, Y.; Ni, Z.; Chen, Y. Experimental observation of the ion-ion correlation effects on charge inversion and strong adhesion between mica surfaces in aqueous electrolyte solutions. *Langmuir* **2014**, 30, 10845–10854.

(60) Chun, J.; Mundy, C. J.; Schenter, G. K. The role of solvent heterogeneity in determining the dispersion interaction between nanoassemblies. *J. Phys. Chem. B* **2015**, 119, 5873–5881.

(61) Parsegian, V. *Van der Waals Forces, A Handbook for Biologists, Chemists, Engineers, And Physicists*. Cambridge University Press: Cambridge, UK, 2005.

(62) Alcantar, N.; Israelachvili, J.; Boles, J. Forces and ionic transport between mica surfaces: Implications for pressure solution. *Geochim. Cosmochim. Acta* **2003**, 67, 1289–1304.

(63) Zhang, Z.; Tang, Z.; Kotov, N. A.; Glotzer, S. C. Simulations and analysis of self-assembly of CdTe nanoparticles into wires and sheets. *Nano Lett.* **2007**, 7, 1670–5.

(64) Liu, L.; Nakouzi, E.; Sushko, M. L.; Schenter, G. K.; Mundy, C. J.; Chun, J.; De Yoreo, J. J. Connecting energetics to dynamics in particle growth by oriented attachment using real-time observations. *Nat. Commun.* **2020**, 11, 1045.

(65) Yasui, K.; Kato, K. Dipole–Dipole Interaction Model for Oriented Attachment of BaTiO₃ Nanocrystals: A Route to Mesocrystal Formation. *J. Phys. Chem. C* **2012**, 116, 319–324.

(66) Alimohammadi, M.; Fichthorn, K. A. Molecular Dynamics Simulation of the Aggregation of Titanium Dioxide Nanocrystals: Preferential Alignment. *Nano Lett.* **2009**, 9, 4198–4203.

(67) Schapotschnikow, P.; van Huis, M. A.; Zandbergen, H. W.; Vanmaekelbergh, D.; Vlucht, T. J. Morphological transformations and fusion of PbSe nanocrystals studied using atomistic simulations. *Nano Lett.* **2010**, 10, 3966–71.

(68) Zhang, H.; Banfield, J. F. Interatomic Coulombic interactions as the driving force for oriented attachment. *CrystEngComm* **2014**, 16, 1568–1578.

(69) Russel, W. B.; Russel, W.; Saville, D. A.; Schowalter, W. R. *Colloidal Dispersions*; Cambridge University Press: 1991; pp 100–121 and pp 149–150.

(70) Owen, B. B.; Miller, R. C.; Milner, C. E.; Cogan, H. L. The dielectric constant of water as a function of temperature and pressure I. *J. Phys. Chem.* **1961**, 65, 2065–2070.

(71) Li, D. S.; Chun, J.; Xiao, D. D.; Zhou, W. J.; Cai, H. C.; Zhang, L.; Rosso, K. M.; Mundy, C. J.; Schenter, G. K.; De Yoreo, J. J. Trends in mica-mica adhesion reflect the influence of molecular details on long-range dispersion forces underlying aggregation and coalignment. *Proc. Nat. Acad. Sci. U. S. A.* **2017**, 114, 7537–7542.

(72) Lee, J.; Nakouzi, E.; Xiao, D.; Wu, Z.; Song, M.; Ophus, C.; Chun, J.; Li, D. Interplay between short- and long-ranged forces leading to the formation of Ag nanoparticle superlattice. *Small* **2019**, 15, 1901966.

(73) Batôt, G.; Dahirel, V.; Méridet, G.; Louis, A. A.; Jardat, M. Dynamics of solutes with hydrodynamic interactions: comparison between Brownian dynamics and stochastic rotation dynamics simulations. *Phys. Rev. E. Stat. Nonlin. Soft Matter Phys.* **2013**, 88, 043304.

(74) Jeffrey, D.; Onishi, Y. Calculation of the Resistance and Mobility functions for two unequal rigid spheres in low-reynolds-number flow. *J. Fluid Mech.* **1984**, 139, 261–290.

(75) Kim, S.; Karrila, S. J. *Microhydrodynamics: Principles and Selected Applications*; Courier Corporation, 2013; pp 107–121 and pp 175–185.

(76) Nakouzi, E.; Soltis, J. A.; Legg, B. A.; Schenter, G. K.; Zhang, X.; Graham, T. R.; Rosso, K. M.; Anovitz, L. M.; De Yoreo, J. J.; Chun, J. Impact of solution chemistry and particle anisotropy on the collective dynamics of oriented aggregation. *ACS Nano* **2018**, 12, 10114–10122.

(77) Halperin, A.; Tirrell, M.; Lodge, T. Tethered chains in polymer microstructures. In *Macromolecules: Synthesis, Order and Advanced Properties*; Springer, 1992; pp 31–71.

(78) De Gennes, P. Polymers at an interface; a Simplified View. *Adv. Colloid Interface Sci.* **1987**, 27, 189–209.

- (79) Israelachvili, J. N. *Intermolecular and Surface Forces*; Academic Press, 2011; pp 341–354 and pp 381–390.
- (80) Hiemenz, P. C.; Lodge, T. P. *Polymer Chemistry*; CRC Press, 2007.
- (81) Zhu, C.; Liang, S.; Song, E.; Zhou, Y.; Wang, W.; Shan, F.; Shi, Y.; Hao, C.; Yin, K.; Zhang, T.; Liu, J.; Zheng, H.; Sun, L. In-situ liquid cell transmission electron microscopy investigation on oriented attachment of gold nanoparticles. *Nat. Commun.* **2018**, *9*, 421.
- (82) Guo, P.; Gao, Y. Coalescence of Au nanoparticles without ligand detachment. *Phys. Rev. Lett.* **2020**, *124*, 066101.
- (83) Balankura, T.; Yan, T.; Jahanmahin, O.; Narukatpichai, J.; Ng, A.; Fichthorn, K. A. Oriented attachment mechanism of triangular Ag nanoplates: a molecular dynamics study. *Nanoscale Adv.* **2020**, *2*, 2265–2270.
- (84) Liu, Z.; Zhou, H.; Lim, Y. S.; Song, J. H.; Piao, L.; Kim, S. H. Synthesis of silver nanoplates by two-dimensional oriented attachment. *Langmuir* **2012**, *28*, 9244–9.
- (85) Kim, M. H.; Yoon, D. K.; Im, S. H. Growth pathways of silver nanoplates in kinetically controlled synthesis: bimodal versus unimodal growth. *RSC Adv.* **2015**, *5*, 14266–14272.
- (86) Si, K. J.; Chen, Y.; Shi, Q.; Cheng, W. Nanoparticle Superlattices: The roles of soft ligands. *Adv. Sci.* **2018**, *5*, 1700179.
- (87) Macfarlane, R. J.; Lee, B.; Jones, M. R.; Harris, N.; Schatz, G. C.; Mirkin, C. A. Nanoparticle Superlattice Engineering with DNA. *Science* **2011**, *334*, 204–208.
- (88) Wang, S.; Lee, S.; Du, J. S.; Partridge, B. E.; Cheng, H. F.; Zhou, W.; Dravid, V. P.; Lee, B.; Glotzer, S. C.; Mirkin, C. A. The emergence of valency in colloidal crystals through electron equivalents. *Nat. Mater.* **2022**, *21*, 580.
- (89) Stofer, E.; Chipot, C.; Lavery, R. Free Energy Calculations of Watson-Crick Base Pairing in Aqueous Solution. *J. Am. Chem. Soc.* **1999**, *121*, 9503–9508.
- (90) Zhuang, W.-R.; Wang, Y.; Cui, P.-F.; Xing, L.; Lee, J.; Kim, D.; Jiang, H.-L.; Oh, Y.-K. Applications of π - π stacking interactions in the design of drug-delivery systems. *J. Controlled Release* **2019**, *294*, 311–326.
- (91) Park, S. Y.; Lytton-Jean, A. K. R.; Lee, B.; Weigand, S.; Schatz, G. C.; Mirkin, C. A. DNA-programmable nanoparticle crystallization. *Nature* **2008**, *451*, 553–556.
- (92) Girard, M.; Wang, S.; Du, J. S.; Das, A.; Huang, Z.; Dravid, V. P.; Lee, B.; Mirkin, C. A.; Olvera de la Cruz, M. Particle analogs of electrons in colloidal crystals. *Science* **2019**, *364*, 1174–1178.
- (93) Chen, C.-L.; Zhang, P.; Rosi, N. L. A new peptide-based method for the design and synthesis of nanoparticle superstructures: construction of highly ordered gold nanoparticle double helices. *J. Am. Chem. Soc.* **2008**, *130*, 13555–13557.
- (94) Zhu, Y.; He, J.; Shang, C.; Miao, X.; Huang, J.; Liu, Z.; Chen, H.; Han, Y. Chiral gold nanowires with boerdijk–coxeter–bernal structure. *J. Chem. Soc.* **2014**, *136*, 12746–12752.
- (95) Liu, Y.; Lin, X.-M.; Sun, Y.; Rajh, T. In Situ Visualization of Self-Assembly of Charged Gold Nanoparticles. *J. Am. Chem. Soc.* **2013**, *135*, 3764–3767.
- (96) Liu, C.; Ou, Z.; Guo, F.; Luo, B.; Chen, W.; Qi, L.; Chen, Q. Colloid–atom duality” in the assembly dynamics of concave gold nanorods. *J. Am. Chem. Soc.* **2020**, *142*, 11669–11673.
- (97) Ou, Z.; Wang, Z.; Luo, B.; Luijten, E.; Chen, Q. Kinetic pathways of crystallization at the nanoscale. *Nat. Mater.* **2020**, *19*, 450–455.
- (98) Jamali, V.; Hargus, C.; Ben-Moshe, A.; Aghazadeh, A.; Ha, H. D.; Mandadapu, K. K.; Alivisatos, A. P. Anomalous nanoparticle surface diffusion in LCTEM is revealed by deep learning-assisted analysis. *Proc. Natl. Acad. Sci. U. S. A.* **2021**, *118*, No. e2017616118.
- (99) Chen, Q.; Cho, H.; Manthiram, K.; Yoshida, M.; Ye, X.; Alivisatos, A. P. Interaction potentials of anisotropic nanocrystals from the trajectory sampling of particle motion using in situ liquid phase transmission electron microscopy. *ACS Cent. Sci.* **2015**, *1*, 33–39.
- (100) Anand, U.; Lu, J.; Loh, D.; Aabdin, Z.; Mirsaidov, U. Hydration layer-mediated pairwise interaction of nanoparticles. *Nano Lett.* **2016**, *16*, 786–790.
- (101) Yao, L.; Ou, Z.; Luo, B.; Xu, C.; Chen, Q. Machine learning to reveal nanoparticle dynamics from liquid-phase TEM videos. *ACS Cent. Sci.* **2020**, *6*, 1421–1430.
- (102) Einstein, A. Über die von der molekularkinetischen Theorie der Wärme geforderte Bewegung von in ruhenden Flüssigkeiten suspendierten Teilchen. *Ann. Phys.* **1905**, *322*, 549–560.
- (103) Liao, H.-G.; Cui, L.; Whitlam, S.; Zheng, H. Real-time imaging of Pt3Fe nanorod growth in solution. *Science* **2012**, *336*, 1011–1014.
- (104) Powers, A. S.; Liao, H.-G.; Raja, S. N.; Bronstein, N. D.; Alivisatos, A. P.; Zheng, H. Tracking nanoparticle diffusion and interaction during self-assembly in a liquid cell. *Nano Lett.* **2017**, *17*, 15–20.
- (105) Sutter, E.; Sutter, P.; Tkachenko, A. V.; Krahne, R.; de Graaf, J.; Arciniegas, M.; Manna, L. In situ microscopy of the self-assembly of branched nanocrystals in solution. *Nat. Commun.* **2016**, *7*, 11213.
- (106) Damasceno, P. F.; Engel, M.; Glotzer, S. C. Predictive self-assembly of polyhedra into complex structures. *Science* **2012**, *337*, 453–457.
- (107) Li, B.; Zhou, D.; Han, Y. Assembly and phase transitions of colloidal crystals. *Nat. Rev. Mater.* **2016**, *1*, 15011.
- (108) Vo, T.; Glotzer, S. C. A theory of entropic bonding. *Proc. Natl. Acad. Sci. U. S. A.* **2022**, *119*, No. e2116414119.
- (109) Damasceno, P. F.; Engel, M.; Glotzer, S. C. Crystalline assemblies and densest packings of a family of truncated tetrahedra and the role of directional entropic forces. *ACS Nano* **2012**, *6*, 609–614.
- (110) Lee, S.; Teich, E. G.; Engel, M.; Glotzer, S. C. Entropic colloidal crystallization pathways via fluid–fluid transitions and multidimensional prenucleation motifs. *PNAS* **2019**, *116*, 14843.
- (111) Geng, Y.; van Anders, G.; Dodd, P. M.; Dshemuchadse, J.; Glotzer, S. C. Engineering entropy for the inverse design of colloidal crystals from hard shapes. *Sci. Adv.* **2019**, *5*, No. eaaw0514.
- (112) Jahanmahin, O.; Kirby, D. J.; Smith, B. D.; Albright, C. A.; Gobert, Z. A.; Keating, C. D.; Fichthorn, K. A. Assembly of gold nanowires on gold nanostripe arrays: simulation and experiment. *J. Phys. Chem. C* **2020**, *124*, 9559–9571.
- (113) Kim, J.; Ou, Z.; Jones, M. R.; Song, X.; Chen, Q. Imaging the polymerization of multivalent nanoparticles in solution. *Nat. Commun.* **2017**, *8*, 761.
- (114) Tan, S. F.; Raj, S.; Bisht, G.; Annadata, H. V.; Nijhuis, C. A.; Král, P.; Mirsaidov, U. Nanoparticle interactions guided by shape-dependent hydrophobic forces. *Adv. Mater.* **2018**, *30*, 1707077.
- (115) Xiao, D.; Wu, Z.; Song, M.; Chun, J.; Schenter, G. K.; Li, D. Silver Nanocube and nanobar growth via anisotropic monomer addition and particle attachment processes. *Langmuir* **2018**, *34*, 1466–1472.
- (116) Lin, H.; Lee, S.; Sun, L.; Spellings, M.; Engel, M.; Glotzer, S. C.; Mirkin, C. A. Clathrate colloidal crystals. *Science* **2017**, *355*, 931–935.
- (117) Agranovich, V. M.; Ginzburg, V. L. Crystal optics with allowance for spatial dispersion; exciton theory. *I. Soviet Physics Uspekhi* **1962**, *5*, 323.
- (118) Landau, L. *Electrodynamics of Continuous Media, Landau and Lifshitz Course of Theoretical Physics*; Elsevier Butterworth–Heinemann, Burlington, MA, 1984; Vol. 8.
- (119) Parsegian, V.; Weiss, G. H. Dielectric anisotropy and the van der Waals interaction between bulk media. *J. Adhes.* **1972**, *3*, 259–267.
- (120) Chun, J.; Li, J.-L.; Car, R.; Aksay, I. A.; Saville, D. A. Anisotropic adsorption of molecular assemblies on crystalline surfaces. *J. Phys. Chem. B* **2006**, *110*, 16624–16632.
- (121) Saville, D.; Chun, J.; Li, J.-L.; Schniepp, H.; Car, R.; Aksay, I. A. Orientational order of molecular assemblies on inorganic crystals. *Phys. Rev. Lett.* **2006**, *96* (1), 018301.
- (122) Zhang, X.; He, Y.; Sushko, M. L.; Liu, J.; Luo, L.; De Yoreo, J. J.; Mao, S. X.; Wang, C.; Rosso, K. M. Direction-specific van der Waals attraction between rutile TiO2 nanocrystals. *Science* **2017**, *356*, 434–437.
- (123) Liu, L. L.; Nakouzi, E.; Sushko, M. L.; Schenter, G. K.; Mundy, C. J.; Chun, J.; De Yoreo, J. J. Connecting energetics to dynamics in particle growth by oriented attachment using real-time observations. *Nat. Commun.* **2020**, *11*, 1045.

- (124) Raju, M.; van Duin, A. C.; Fichthorn, K. A. Mechanisms of oriented attachment of TiO₂ nanocrystals in vacuum and humid environments: reactive molecular dynamics. *Nano Lett.* **2014**, *14*, 1836–42.
- (125) Penn, R. L.; Banfield, J. F. Morphology development and crystal growth in nanocrystalline aggregates under hydrothermal conditions: Insights from titania. *Geochim. Cosmochim. Acta* **1999**, *63*, 1549–1557.
- (126) Li, D. S.; Wang, H. L.; Xiao, D. D.; Song, M.; Legg, B.; Chun, J. Investigating the magnitude and source of orientation-dependent interactions between TiO₂ crystal surfaces. *Nanoscale* **2017**, *9*, 10173–10177.
- (127) Zhang, X.; Shen, Z.; Liu, J.; Kerisit, S. N.; Bowden, M. E.; Sushko, M. L.; De Yoreo, J. J.; Rosso, K. M. Direction-specific interaction forces underlying zinc oxide crystal growth by oriented attachment. *Nat. Commun.* **2017**, *8*, 835.
- (128) Ren, P.; Lu, Z.; Song, M.; Liu, L.; Wang, B.; Wei, N.; Bowden, M. E.; Wirth, M. G.; Perea, D. E.; Zhang, D.; et al. Formation of Pyrophosphates across Grain Boundaries Induces the Formation of Mismatched but Oriented Interfaces in Silver Phosphate Polypods. *Appl. Surf. Sci.* **2021**, *563*, 149980.
- (129) Gras, P.; Rey, C.; Andre, G.; Charvillat, C.; Sarda, S.; Combes, C. Crystal structure of monoclinic calcium pyrophosphate dihydrate (m-CPPD) involved in inflammatory reactions and osteoarthritis. *Acta Crystallogr. B* **2016**, *72*, 96–101.
- (130) Nakouzi, E.; Stack, A. G.; Kerisit, S.; Legg, B. A.; Mundy, C. J.; Schenter, G. K.; Chun, J.; De Yoreo, J. J. Moving beyond the solvent-tip approximation to determine site-specific variations of interfacial water structure through 3D force microscopy. *J. Phys. Chem. C* **2021**, *125*, 1282–1291.
- (131) Zhang, X.; Shen, Z.; Liu, J.; Kerisit, S.; Bowden, M.; Sushko, M.; De Yoreo, J.; Rosso, K. M. Direction-specific interaction forces underlying zinc oxide crystal growth by oriented attachment. *Nat. Commun.* **2017**, *8*, 835.
- (132) Lee, J.; Nakouzi, E.; Xiao, D.; Wu, Z. G.; Song, M.; Ophus, C.; Chun, J.; Li, D. S. Interplay between short- and long-ranged forces leading to the formation of Ag nanoparticle superlattice. *Small* **2019**, *15*, 1901966.
- (133) Chun, J. H.; Mundy, C. J.; Schenter, G. K. The Role of Solvent Heterogeneity in determining the dispersion interaction between nanoassemblies. *J. Phys. Chem. B* **2015**, *119*, 5873–5881.
- (134) Ho, T. A.; Criscenti, L. J. Molecular-level understanding of gibbsite particle aggregation in water. *J. Colloid Interface Sci.* **2021**, *600*, 310–317.
- (135) Kerisit, S. N.; De Yoreo, J. J. Effect of hydrophilicity and interfacial water structure on particle attachment. *J. Phys. Chem. C* **2020**, *124*, 5480–5488.
- (136) Shen, Z. Z.; Chun, J. H.; Rosso, K. M.; Mundy, C. J. Surface chemistry affects the efficacy of the hydration force between two ZnO(1010) Surfaces. *J. Phys. Chem. C* **2018**, *122*, 12259–12266.
- (137) Zhang, X.; Shen, Z.; Liu, J.; Kerisit, S. N.; Bowden, M. E.; Sushko, M. L.; De Yoreo, J. J.; Rosso, K. M. Direction-specific interaction forces underlying zinc oxide crystal growth by oriented attachment. *Nat. Commun.* **2017**, *8*, 835.
- (138) Li, D. S.; Chun, J. H.; Xiao, D. D.; Zhou, W. J.; Cai, H. C.; Zhang, L.; Rosso, K. M.; Mundy, C. J.; Schenter, G. K.; De Yoreo, J. J. Trends in mica-mica adhesion reflect the influence of molecular details on long-range dispersion forces underlying aggregation and coalignment. *PNAS* **2017**, *114*, 7537–7542.
- (139) Li, T.-D.; Riedo, E. Nonlinear viscoelastic dynamics of nanoconfined wetting liquids. *Phys. Rev. Lett.* **2008**, *100*, 106102.
- (140) Zhu, Y.; Granick, S. Viscosity of interfacial water. *Phys. Rev. Lett.* **2001**, *87*, 096104.
- (141) Fumagalli, L.; Esfandiari, A.; Fabregas, R.; Hu, S.; Ares, P.; Janardanan, A.; Yang, Q.; Radha, B.; Taniguchi, T.; Watanabe, K.; et al. Anomalous low dielectric constant of confined water. *Science* **2018**, *360*, 1339–1342.
- (142) Sushko, M. L. Understanding the driving forces for crystal growth by oriented attachment through theory and simulations. *J. Mater. Sci.* **2019**, *34*, 2914–2927.
- (143) Qin, Y.; Fichthorn, K. A. Solvation forces between colloidal nanoparticles: directed alignment. *Phys. Rev. E* **2006**, *73*, 020401.
- (144) Kerisit, S. N.; De Yoreo, J. J. Effect of Hydrophilicity and Interfacial water structure on particle attachment. *J. Phys. Chem. C* **2020**, *124*, 5480–5488.
- (145) Zhang, X.; Shen, Z.; Liu, J.; Kerisit, S. N.; Bowden, M. E.; Sushko, M. L.; De Yoreo, J. J.; Rosso, K. M. Direction-specific interaction forces underlying zinc oxide crystal growth by oriented attachment. *Nat. Commun.* **2017**, *8*, 835.
- (146) Kashchiev, D. Thermodynamically consistent description of the work to form a nucleus of any size. *J. Chem. Phys.* **2003**, *118*, 1837–1851.
- (147) Yang, J.; Zeng, Z.; Kang, J.; Betzler, S.; Czarnik, C.; Zhang, X.; Ophus, C.; Yu, C.; Bustillo, K.; Pan, M.; Qiu, J.; Wang, L.-W.; Zheng, H. Formation of two-dimensional transition metal oxide nanosheets with nanoparticles as intermediates. *Nat. Mater.* **2019**, *18*, 970–976.
- (148) Sathiyarayanan, R.; Alimohammadi, M.; Zhou, Y.; Fichthorn, K. A. Role of solvent in the shape-controlled synthesis of anisotropic colloidal nanostructures. *J. Phys. Chem. C* **2011**, *115*, 18983–18990.
- (149) Dong, M.; Wang, W.; Wei, W.; Hu, X.; Qin, M.; Zhang, Q.; Sun, L.; Xu, F. Understanding the ensemble of growth behaviors of sub-10-nm silver nanorods using in situ liquid cell transmission electron microscopy. *J. Phys. Chem. C* **2019**, *123*, 21257–21264.
- (150) Halder, A.; Ravishankar, N. Ultrafine Single-crystalline gold nanowire arrays by oriented attachment. *Adv. Mater.* **2007**, *19*, 1854–1858.
- (151) Yang, J.; Zeng, Z.; Kang, J.; Betzler, S.; Czarnik, C.; Zhang, X.; Ophus, C.; Yu, C.; Bustillo, K.; Pan, M.; Qiu, J.; Wang, L. W.; Zheng, H. Formation of two-dimensional transition metal oxide nanosheets with nanoparticles as intermediates. *Nat. Mater.* **2019**, *18*, 970–976.
- (152) Fichthorn, K. A. A Pathway from 3D to 2D. *Nat. Mater.* **2019**, *18*, 911–912.
- (153) Wang, G.; Li, G. Titania from nanoclusters to nanowires and nanoforks. *Eur. Phys. J. D. Atomic, Molecular, Optical and Plasma Physics* **2003**, *24*, 355–360.
- (154) Ranade, M. R.; Navrotsky, A.; Zhang, H. Z.; Banfield, J. F.; Elder, S. H.; Zaban, A.; Borse, P. H.; Kulkarni, S. K.; Doran, G. S.; Whitfield, H. J. Energetics of nanocrystalline TiO₂. *PNAS* **2002**, *99*, 6476–6481.
- (155) Liu, L.; Wang, J.; Gong, S. K.; Mao, S. X. High resolution transmission electron microscope observation of zero-strain deformation twinning mechanisms in Ag. *Phys. Rev. Lett.* **2011**, *106*, 175504.
- (156) Whitham, K.; Smilgies, D.-M.; Hanrath, T. Entropic, enthalpic, and kinetic aspects of interfacial nanocrystal superlattice assembly and attachment. *Chem. Mater.* **2018**, *30*, 54–63.
- (157) Sandeep, C. S. S.; Azpiroz, J. M.; Evers, W. H.; Boehme, S. C.; Moreels, I.; Kinge, S.; Siebbeles, L. D. A.; Infante, I.; Houtepen, A. J. Epitaxially connected PbSe quantum-dot Films: Controlled neck formation and optoelectronic properties. *ACS Nano* **2014**, *8*, 11499–11511.
- (158) Lim, T. H.; McCarthy, D.; Hendy, S. C.; Stevens, K. J.; Brown, S. A.; Tilley, R. D. Real-time TEM and kinetic monte carlo studies of the coalescence of decahedral gold nanoparticles. *ACS Nano* **2009**, *3*, 3809–3813.
- (159) Simon, P.; Bahrig, L.; Baburin, I. A.; Formanek, P.; Röder, F.; Sickmann, J.; Hickey, S. G.; Eychmüller, A.; Lichte, H.; Kniep, R.; Rosseeva, E. Interconnection of nanoparticles within 2D superlattices of PbS/oleic acid thin films. *Adv. Mater.* **2014**, *26*, 3042–3049.
- (160) Whitham, K.; Yang, J.; Savitzky, B. H.; Kourkoutis, L. F.; Wise, F.; Hanrath, T. Charge transport and localization in atomically coherent quantum dot solids. *Nat. Mater.* **2016**, *15*, 557–563.
- (161) Evers, W. H.; Schins, J. M.; Aerts, M.; Kulkarni, A.; Capiod, P.; Berthe, M.; Grandidier, B.; Delerue, C.; van der Zant, H. S. J.; van Overbeek, C.; et al. High charge mobility in two-dimensional percolative networks of PbSe quantum dots connected by atomic bonds. *Nat. Commun.* **2015**, *6*, 8195.
- (162) Whitham, K.; Hanrath, T. Formation of epitaxially connected quantum dot solids: Nucleation and coherent phase transition. *J. Phys. Chem. Lett.* **2017**, *8*, 2623–2628.

- (163) Xu, Y.; Wang, X.; Zhang, W. L.; Lv, F.; Guo, S. Recent progress in two-dimensional inorganic quantum dots. *Chem. Soc. Rev.* **2018**, *47*, 586–625.
- (164) Talapin, D. V.; Lee, J.-S.; Kovalenko, M. V.; Shevchenko, E. V. Prospects of colloidal nanocrystals for electronic and optoelectronic applications. *Chem. Rev.* **2010**, *110*, 389–458.
- (165) Boles, M. A.; Engel, M.; Talapin, D. V. Self-assembly of colloidal nanocrystals: From intricate structures to functional materials. *Chem. Rev.* **2016**, *116*, 11220–11289.
- (166) Kagan, C. R.; Lifshitz, E.; Sargent, E. H.; Talapin, D. V. Building devices from colloidal quantum dots. *Science* **2016**, *353*, aac5523.
- (167) Beugeling, W.; Kalesaki, E.; Delerue, C.; Niquet, Y. M.; Vanmaekelbergh, D.; Smith, C. M. Topological States in multi-orbital HgTe honeycomb lattices. *Nat. Commun.* **2015**, *6*, 6316.
- (168) De Yoreo, J. J.; Gilbert, P. U. P. A.; Sommerdijk, N. A. J. M.; Penn, R. L.; Whitelam, S.; Joester, D.; Zhang, H.; Rimer, J. D.; Navrotsky, A.; Banfield, J. F.; Wallace, A. F.; Michel, F. M.; Meldrum, F. C.; Cölfen, H.; Dove, P. M. Crystallization by particle attachment in synthetic, biogenic, and geologic environments. *Science* **2015**, *349*, aaa6760.
- (169) Urban, J. J. Prospects for Thermoelectricity in quantum dot hybrid arrays. *Nat. Nanotechnol.* **2015**, *10*, 997–1001.
- (170) van Overbeek, C.; Peters, J. L.; van Rossum, S. A. P.; Smits, M.; van Huis, M. A.; Vanmaekelbergh, D. Interfacial self-assembly and oriented attachment in the family of PbX (X = S, Se, Te) nanocrystals. *J. Phys. Chem. C* **2018**, *122*, 12464–12473.
- (171) Geuchies, J. J.; van Overbeek, C.; Evers, W. H.; Goris, B.; de Backer, A.; Gantapara, A. P.; Rabouw, F. T.; Hilhorst, J.; Peters, J. L.; Konovalov, O.; Petukhov, A. V.; Dijkstra, M.; Siebbeles, L. D. A.; van Aert, S.; Bals, S.; Vanmaekelbergh, D. In situ study of the formation mechanism of two-dimensional superlattices from PbSe nanocrystals. *Nat. Mater.* **2016**, *15*, 1248–1254.
- (172) Weidman, M. C.; Smilgies, D.-M.; Tisdale, W. A. Kinetics of the Self-assembly of nanocrystal superlattices measured by real-time in situ X-Ray scattering. *Nat. Mater.* **2016**, *15*, 775–781.
- (173) Zaluzhnyy, I. A.; Kurta, R. P.; André, A.; Gorobtsov, O. Y.; Rose, M.; Skopintsev, P.; Besedin, I.; Zozulya, A. V.; Sprung, M.; Schreiber, F.; et al. Quantifying angular correlations between the atomic lattice and the superlattice of nanocrystals assembled with directional linking. *Nano Lett.* **2017**, *17*, 3511–3517.
- (174) Yalcin, A. O.; Fan, Z.; Goris, B.; Li, W.-F.; Koster, R. S.; Fang, C.-M.; van Blaaderen, A.; Casavola, M.; Tichelaar, F. D.; Bals, S.; et al. Atomic resolution monitoring of cation exchange in CdSe-PbSe heteronanocrystals during epitaxial solid–solid–vapor growth. *Nano Lett.* **2014**, *14*, 3661–3667.
- (175) Cho, K.-S.; Talapin, D. V.; Gaschler, W.; Murray, C. B. Designing PbSe nanowires and nanorings through oriented attachment of nanoparticles. *J. Am. Chem. Soc.* **2005**, *127*, 7140–7147.
- (176) Evers, W. H.; Goris, B.; Bals, S.; Casavola, M.; de Graaf, J.; van Roij, R.; Dijkstra, M.; Vanmaekelbergh, D. Low-dimensional semiconductor superlattices formed by geometric control over nanocrystal attachment. *Nano Lett.* **2013**, *13*, 2317–2323.
- (177) Wang, Y.; Peng, X.; Abelson, A.; Zhang, B.-K.; Qian, C.; Ercius, P.; Wang, L.-W.; Law, M.; Zheng, H. In situ TEM observation of neck formation during oriented attachment of PbSe nanocrystals. *Nano Res.* **2019**, *12*, 2549–2553.
- (178) Elert, G. “Viscosity” *The Physics Hypertextbook*; The Physics Hypertextbook, **1998–2022** (accessed 2007-10-02).
- (179) Tian, Y.; Zhang, Y.; Wang, T.; Xin, H. L.; Li, H.; Gang, O. Lattice engineering through nanoparticle–DNA frameworks. *Nat. Mater.* **2016**, *15*, 654–661.
- (180) Lin, Q.-Y.; Mason, J. A.; Li, Z.; Zhou, W.; O’Brien, M. N.; Brown, K. A.; Jones, M. R.; Butun, S.; Lee, B.; Dravid, V. P.; et al. Building superlattices from individual nanoparticles via template-confined DNA-mediated assembly. *Science* **2018**, *359*, 669–672.
- (181) Lin, H.; Lee, S.; Sun, L.; Spellings, M.; Engel, M.; Glotzer, S. C.; Mirkin, C. A. Clathrate colloidal crystals. *Science* **2017**, *355*, 931–935.
- (182) Li, L.; Yang, Y.; Ding, J.; Xue, J. Synthesis of magnetite nanooctahedra and their magnetic field-induced two-/three-dimensional superstructure. *Chem. Mater.* **2010**, *22* (10), 3183–3191.
- (183) Grzelczak, M.; Vermant, J.; Furst, E. M.; Liz-Marzán, L. M. Directed self-assembly of nanoparticles. *ACS Nano* **2010**, *4*, 3591–3605.
- (184) Yanai, N.; Sindoro, M.; Yan, J.; Granick, S. Electric field-induced assembly of monodisperse polyhedral metal–organic framework crystals. *J. Am. Chem. Soc.* **2013**, *135*, 34–37.
- (185) Dong, D.; Fu, R.; Shi, Q.; Cheng, W. Self-assembly and characterization of 2D plasmene nanosheets. *Nat. Protoc.* **2019**, *14*, 2691–2706.
- (186) Talapin, D. V.; Shevchenko, E. V.; Murray, C. B.; Kornowski, A.; Förster, S.; Weller, H. CdSe and CdSe/CdS nanorod solids. *J. Am. Chem. Soc.* **2004**, *126*, 12984–12988.
- (187) Bodnarchuk, M. I.; Li, L.; Fok, A.; Nachtergaele, S.; Ismagilov, R. F.; Talapin, D. V. Three-dimensional nanocrystal superlattices grown in nanoliter microfluidic plugs. *J. Am. Chem. Soc.* **2011**, *133*, 8956–8960.
- (188) Powers, A. S.; Liao, H.-G.; Raja, S. N.; Bronstein, N. D.; Alivisatos, A. P.; Zheng, H. Tracking nanoparticle diffusion and interaction during self-assembly in a liquid cell. *Nano Lett.* **2017**, *17*, 15–20.
- (189) Abelson, A.; Qian, C.; Salk, T.; Luan, Z.; Fu, K.; Zheng, J.-G.; Wardini, J. L.; Law, M. Collective topo-epitaxy in the self-assembly of a 3D quantum dot superlattice. *Nat. Mater.* **2020**, *19*, 49–55.
- (190) Tan, S. F.; Chee, S. W.; Lin, G.; Mirsaidov, U. Direct observation of interactions between nanoparticles and nanoparticle self-assembly in solution. *Acc. Chem. Res.* **2017**, *50*, 1303–1312.
- (191) Ou, Z.; Wang, Z.; Luo, B.; Luijten, E.; Chen, Q. Kinetic pathways of crystallization at the nanoscale. *Nat. Mater.* **2020**, *19*, 450–455.
- (192) Fan, Z.; Grünwald, M. Orientational order in self-assembled nanocrystal superlattices. *J. Am. Chem. Soc.* **2019**, *141*, 1980–1988.
- (193) Parent, L. R.; Bakalis, E.; Proetto, M.; Li, Y.; Park, C.; Zerbetto, F.; Gianneschi, N. C. Tackling the challenges of dynamic experiments using liquid-cell transmission electron microscopy. *Acc. Chem. Res.* **2018**, *51*, 3–11.
- (194) Verch, A.; Pfaff, M.; de Jonge, N. Exceptionally slow movement of gold nanoparticles at a solid/liquid interface investigated by scanning transmission electron microscopy. *Langmuir* **2015**, *31*, 6956–6964.
- (195) Lu, J.; Aabdin, Z.; Loh, N. D.; Bhattacharya, D.; Mirsaidov, U. Nanoparticle dynamics in a nanodroplet. *Nano Lett.* **2014**, *14*, 2111–2115.
- (196) Woehl, T. J.; Prozorov, T. The mechanisms for nanoparticle surface diffusion and chain self-assembly determined from real-time nanoscale kinetics in liquid. *J. Phys. Chem. C* **2015**, *119*, 21261–21269.
- (197) Zheng, H.; Claridge, S. A.; Minor, A. M.; Alivisatos, A. P.; Dahmen, U. Nanocrystal diffusion in a liquid thin film observed by in situ transmission electron microscopy. *Nano Lett.* **2009**, *9*, 2460–2465.
- (198) Sahoo, S.; Husale, S.; Colwill, B.; Lu, T.-M.; Nayak, S.; Ajayan, P. M. Electric field directed self-assembly of cuprous oxide nanostructures for photon sensing. *ACS Nano* **2009**, *3*, 3935–3944.
- (199) Jiang, X.; Feng, J.; Huang, L.; Wu, Y.; Su, B.; Yang, W.; Mai, L.; Jiang, L. Bioinspired 1D superparamagnetic magnetite arrays with magnetic field perception. *Adv. Mater.* **2016**, *28*, 6952–6958.
- (200) Liu, Z. F.; Fang, S.; Moura, F. A.; Ding, J. N.; Jiang, N.; Di, J.; Zhang, M.; Lepó, X.; Galvão, D. S.; Haines, C. S.; et al. Hierarchically buckled sheath-core fibers for superelastic electronics, sensors, and muscles. *Science* **2015**, *349*, 400–404.
- (201) Palacci, J.; Sacanna, S.; Preska Steinberg, A.; Pine, D. J.; Chaikin, P. M. Living crystals of light-activated colloidal surfers. *Science* **2013**, *339*, 936–940.
- (202) Dai, B.; Wang, J.; Xiong, Z.; Zhan, X.; Dai, W.; Li, C.-C.; Feng, S.-P.; Tang, J. Programmable artificial phototactic microswimmer. *Nat. Nanotechnol.* **2016**, *11*, 1087–1092.
- (203) Mu, J.; Hou, C.; Wang, H.; Li, Y.; Zhang, Q.; Zhu, M. Origami-inspired active graphene-based paper for programmable instant self-folding walking devices. *Sci. Adv.* **2015**, *1*, No. e1500533.

- (204) Qin, H.; Zhang, T.; Li, N.; Cong, H.-P.; Yu, S.-H. Anisotropic and self-healing hydrogels with multi-responsive actuating capability. *Nat. Commun.* **2019**, *10*, 2202.
- (205) Huang, C.; Chen, X.; Xue, Z.; Wang, T. Effect of structure: A new insight into nanoparticle assemblies from inanimate to animate. *Sci. Adv.* **2020**, *6*, No. eaba1321.
- (206) Liao, H.-G.; Zheng, H. Liquid cell transmission electron microscopy study of platinum iron nanocrystal growth and shape evolution. *J. Am. Chem. Soc.* **2013**, *135*, 5038–5043.
- (207) Wang, Y.; Peng, X.; Abelson, A.; Xiao, P.; Qian, C.; Yu, L.; Ophus, C.; Ercius, P.; Wang, L.-W.; Law, M.; Zheng, H. Dynamic deformability of individual PbSe nanocrystals during superlattice phase transitions. *Sci. Adv.* **2019**, *5*, aaw5623.
- (208) Tian, X.; Anand, U.; Mirsaidov, U.; Zheng, H. Spontaneous reshaping and splitting of AgCl nanocrystals under electron beam illumination. *Small* **2018**, *14*, 1803231.
- (209) Zheng, H. Imaging, understanding, and control of nanoscale materials transformations. *MRS Bull.* **2021**, *46*, 443–450.
- (210) Peters, J. L.; van den Bos, K. H. W.; Van Aert, S.; Goris, B.; Bals, S.; Vanmaekelbergh, D. Ligand-induced shape transformation of PbSe nanocrystals. *Chem. Mater.* **2017**, *29*, 4122–4128.
- (211) Schapotschnikov, P.; van Huis, M. A.; Zandbergen, H. W.; Vanmaekelbergh, D.; Vlugt, T. J. H. Morphological transformations and fusion of PbSe nanocrystals studied using atomistic simulations. *Nano Lett.* **2010**, *10*, 3966–3971.
- (212) Hernández-Guzmán, J.; Weeks, E. R. The equilibrium intrinsic crystal–liquid interface of colloids. *Proc. Nat. Acad. Sci. U. S. A.* **2009**, *106*, 15198.
- (213) Hoyt, J. J.; Asta, M.; Karma, A. Method for computing the anisotropy of the solid–liquid interfacial free energy. *Phys. Rev. Lett.* **2001**, *86*, 5530–5533.
- (214) Ou, Z.; Yao, L.; An, H.; Shen, B.; Chen, Q. Imaging how thermal capillary waves and anisotropic interfacial stiffness shape nanoparticle supracrystals. *Nat. Commun.* **2020**, *11*, 4555.
- (215) Nguyen, V. D.; Dang, M. T.; Weber, B.; Hu, Z.; Schall, P. Visualizing the structural solid–liquid transition at colloidal crystal/fluid interfaces. *Adv. Mater.* **2011**, *23*, 2716–2720.
- (216) Auyeung, E.; Li, T. I. N. G.; Senesi, A. J.; Schmucker, A. L.; Pals, B. C.; de la Cruz, M. O.; Mirkin, C. A. DNA-mediated nanoparticle crystallization into Wulff polyhedra. *Nature* **2014**, *505*, 73–77.
- (217) Mirabello, G.; Ianiro, A.; Bomans, P. H. H.; Yoda, T.; Arakaki, A.; Friedrich, H.; de With, G.; Sommerdijk, N. Crystallization by particle attachment is a colloidal assembly process. *Nat. Mater.* **2020**, *19*, 391–396.
- (218) Aabdin, Z.; Lu, J. Y.; Zhu, X.; Anand, U.; Loh, N. D.; Su, H. B.; Mirsaidov, U. Bonding pathways of aoid nanocrystals in solution. *Nano Lett.* **2014**, *14*, 6639–6643.
- (219) Li, D. S.; Nielsen, M. H.; Lee, J. R. I.; Frandsen, C.; Banfield, J. F.; De Yoreo, J. J. Direction-specific interactions control crystal growth by oriented attachment. *Science* **2012**, *336*, 1014–1018.
- (220) Liao, H. G.; Cui, L. K.; Whitlam, S.; Zheng, H. M. Real-time imaging of Pt3Fe nanorod growth in solution. *Science* **2012**, *336*, 1011–1014.
- (221) Liu, L.; Nakouzi, E.; Sushko, M. L.; Schenter, G. K.; Mundy, C. J.; Chun, J.; De Yoreo, J. J. Connecting energetics to dynamics in particle growth by oriented attachment using real-time observations. *Nat. Commun.* **2020**, *11*, 1045.
- (222) Ye, X.; Jones, M. R.; Frechette, L. B.; Chen, Q.; Powers, A. S.; Ercius, P.; Dunn, G.; Rotskoff, G. M.; Nguyen, S. C.; Adiga, V. P.; Zettl, A.; Rabani, E.; Geissler, P. L.; Alivisatos, A. P. Single-particle mapping of nonequilibrium nanocrystal transformations. *Science* **2016**, *354*, 874–877.
- (223) Wu, Z. G.; Chun, J. H.; Chatterjee, S.; Li, D. S. Fabrication of oriented crystals as force measurement tips via focused ion beam and microlithography methods. *Surf. Interface Anal.* **2018**, *50*, 117–122.
- (224) Herruzo, E. T.; Asakawa, H.; Fukuma, T.; Garcia, R. Three-dimensional quantitative force maps in liquid with 10 piconewton, angstrom and sub-minute resolutions. *Nanoscale* **2013**, *5*, 2678–2685.
- (225) Martin-Jimenez, D.; Chacon, E.; Tarazona, P.; Garcia, R. Atomically resolved three-dimensional structures of electrolyte aqueous solutions near a solid surface. *Nat. Commun.* **2016**, *7*, 12164.
- (226) Uhlig, M. R.; Martin-Jimenez, D.; Garcia, R. Atomic-scale mapping of hydrophobic layers on graphene and few-layer MoS2 and WSe2 in water. *Nat. Commun.* **2019**, *10*, 2696.
- (227) Fukuma, T.; Higgins, M. J.; Jarvis, S. P. Direct imaging of individual intrinsic hydration layers on lipid bilayers at angstrom resolution. *Biophys. J.* **2007**, *92*, 3603–3609.
- (228) Fukuma, T.; Jarvis, S. P. Development of liquid-environment frequency modulation atomic force microscope with low noise deflection sensor for cantilevers of various dimensions. *Rev. Sci. Instrum.* **2006**, *77*, 043701.
- (229) Miyazawa, K.; Kobayashi, N.; Watkins, M.; Shluger, A. L.; Amano, K.; Fukuma, T. A relationship between three-dimensional surface hydration structures and force distribution measured by atomic force microscopy. *Nanoscale* **2016**, *8*, 7334–7342.
- (230) Songen, H.; Bechstein, R.; Kuhnle, A. Quantitative atomic force microscopy. *Condens. Matter Phys.* **2017**, *29*, 274001.
- (231) Songen, H.; Marutschke, C.; Spijker, P.; Holmgren, E.; Hermes, I.; Bechstein, R.; Klassen, S.; Tracey, J.; Foster, A. S.; Kuhnle, A. Chemical identification at the solid–liquid interface. *Langmuir* **2017**, *33*, 125–129.
- (232) Bourg, I. C.; Lee, S. S.; Fenter, P.; Tournassat, C. Stern layer structure and energetics at mica–water interfaces. *J. Phys. Chem. C* **2017**, *121*, 9402–9412.
- (233) Cheng, L.; Fenter, P.; Nagy, K.; Schlegel, M.; Sturchio, N. Molecular-scale density oscillations in water adjacent to a mica surface. *Phys. Rev. Lett.* **2001**, *87*, 156103.
- (234) Prakash, A.; Pfaendtner, J.; Chun, J.; Mundy, C. J. Quantifying the molecular-scale aqueous response to the mica surface. *J. Phys. Chem. C* **2017**, *121*, 18496–18504.
- (235) Davies, B.; Ninham, B. Van der Waals forces in electrolytes. *Chem. Phys.* **1972**, *56*, 5797–5801.